

Gridded Meteorological Datasets and Hydrological Modelling in the Upper Indus Basin

Final Report

October 2014

Authors

A.F. Lutz (MSc.)
Dr. W.W. Immerzeel
P.D.A. Kraaijenbrink (MSc.)

Client

International Centre for Integrated Mountain Development (ICIMOD)

Report FutureWater: 130



FutureWater

Costerweg 1V
6702 AA Wageningen
The Netherlands

+31 (0)317 460050

info@futurewater.nl

www.futurewater.nl

Preface

ICIMOD has contracted FutureWater to generate high-resolution gridded meteorological datasets and conduct a high-resolution hydrological modelling analysis for the Upper Indus Basin (UIB). The project ran from 15 September 2013 until 30 June 2014.

The original TOR did not contain any work on climate change downscaling, but given delays in delivery of the climate change scenarios, FutureWater has implemented an advanced delta change approach for a selection of CMIP5 climate models. These datasets were used to force the hydrological model.

This technical report discusses the work performed by FutureWater during the project, and includes discussion of the results.

Arthur Lutz
Walter Immerzeel
Philip Kraaijenbrink

Wageningen, October 2014



Table of contents

1	Introduction	8
1.1	Background	8
1.2	Objectives and division of tasks	8
2	Improving gridded meteorological data in the Upper Indus Basin	10
2.1	Existing gridded products	10
2.2	Shortcomings in APHRODITE product	12
2.3	Station observations	14
2.4	Methods	16
	2.4.1 Correction of air temperature	17
	2.4.2 Correction of precipitation data	19
2.5	Corrected gridded air temperature dataset	21
2.6	Corrected gridded precipitation dataset	23
2.7	Validation to observed runoff	25
3	Future Climate	27
3.1	Selection of General Circulation Models	27
3.2	Advanced Delta Change method	28
	3.2.1 Description of the Advanced Delta Change method	28
	3.2.2 Implementing the Advanced Delta Change method for the Upper Indus basin	32
3.3	Changes in Climate	34
	3.3.1 Changes in temperature	34
	3.3.2 Changes in precipitation	37
	3.3.3 Changes in precipitation extremes	41
4	Distributed hydrological modelling	44
4.1	Model description	44
	4.1.1 Spatial Processes in Hydrology model (SPHY)	44
	4.1.2 Cryospheric processes	45
	4.1.3 Rainfall runoff	48
	4.1.4 Ground water	49
	4.1.5 Routing	49
4.2	Calibration	49
	4.2.1 Calibration of parameters related to glacier melt	50
	4.2.2 Calibration of parameters related to snow melt	51
	4.2.3 Calibration of parameters related to rainfall-runoff, baseflow and routing	54
4.3	Validation	56
4.4	Current hydrology	58
4.5	Future hydrological changes	62
	4.5.1 Changes in glacier extent	62
	4.5.2 Changes in water availability	63
	4.5.3 Changes in hydrological extremes	70
5	Conclusions and Recommendations	77
	References	79



Tables

Table 1: Overview of gridded meteorological products.	10
Table 2: Long-term annual average runoff for different subbasins in the upper Indus basin [Sharif et al., 2013b].	14
Table 3: Meteorological ground station records in the UIB.	15
Table 4: Vertical temperature lapse rates per altitudinal zone [Tahir et al., 2011b].	17
Table 5: Observed discharge in the UIB. Data originates from PMD and WAPDA as published in scientific literature [Archer, 2003b; Sharif et al., 2013b].	26
Table 6: Selected GCM runs for ensemble of RCP4.5 and RCP8.5 GCMs.	28
Table 7: List of years from reference period used as basis for future period (2001-2100).	33
Table 8: UIB-averaged projected temperature changes according to the downscaled GCMs. The delta values for the two time slices are with respect to the reference period (1971-2000)..	35
Table 9: UIB-averaged projected precipitation changes according to the downscaled GCMs. The delta values for the two time slices are with respect to the reference period (1971-2000)..	38
Table 10: UIB-averaged projections of temperature and precipitation change for the monsoon season and winter season with respect to the reference period (1971-2000).	41
Table 11: Quantiles of daily precipitation averaged over five subbasins in the UIB for the reference period, near future and far future, for all ensemble members in RCP4.5 and RCP8.5	41
Table 12: Soil properties used in HI-SPHY model.	48
Table 13: Calibrated values for glacier melt related parameters in the SPHY-model.....	51
Table 14: Calibrated values for snowmelt related parameters in the SPHY-model.....	51
Table 15: Gauging stations used for calibration and validation of the SPHY model.....	54
Table 16: Validation of simulated discharge to observed long-term averaged discharge data. .	58
Table 17: Hydro-meteorological characteristics of the entire UIB and five subbasins for the reference period (1971-2000).....	61
Table 18: Projected changes in the total UIB and five subbasins for the entire multi-model ensemble for two future periods (2031-2060 and 2071-2100) with respect to the reference period (1971-2000).....	65
Table 19: Quantiles of daily discharge values at five locations in the UIB for the reference period, near future and far future for the model forced with each ensemble member in RCP4.5 and RCP8.5	71

Figures

Figure 1: Multiannual mean (1998-2007) of summer (JJAS) precipitation over the HKKH region as represented by different dataset [Palazzi et al., 2013b].	11
Figure 2: Multiannual mean (1998-2007) of winter (DJFMA) precipitation over the HKH region as represented by different dataset [Palazzi et al., 2013].	12
Figure 3: Annual precipitation in the upper Indus Basins (APHRODITE 1998-2007).....	13
Figure 4: Meteorological ground stations in the upper Indus basin.	15
Figure 5: Conceptual model of vertical and horizontal meteorological and cryospheric regimes in the Karakoram [Hewitt, 2007b].	16



Figure 6: Bias between observed temperatures and gridded temperatures per month. Dots represent the average bias for 14 stations. Error bars represent the complete range of bias for 14 stations.	17
Figure 7: Bias between observations and gridded temperature per month and by station elevation.	18
Figure 8: Regional glacier mass balance for three subzones in the UIB for 2003-2008 as derived using IceSat [<i>Kääb et al., 2012b</i>].	20
Figure 9: Estimated precipitation gradients at the locations of individual glacier systems in the UIB. The precipitation field on the background is the annual precipitation according to the original APHRODITE data 1998-2007.	21
Figure 10: Mean air temperature 1961-2007 according to APHRODITE (upper panel) and the corrected dataset (middle panel). Lower panel shows the difference between the corrected dataset and the uncorrected dataset.	22
Figure 11: UIB averaged mean air temperature 1961-2007.	23
Figure 12: Average annual precipitation 1998-2007 according to APHRODITE (upper panel) and the corrected dataset (middle panel). Lower panel shows the ratio of the corrected dataset over the uncorrected dataset.	24
Figure 13: UIB averaged annual precipitation 1961-2007.	25
Figure 14: Calculated runoff vs observed runoff for multiple gauged catchments in the UIB. Results are shown for uncorrected APHRODITE and corrected APHRODITE.	25
Figure 15: Average temperature and precipitation change in the Upper Indus basin (2071-2100 with respect to 1961-1990) for all RCP4.5 and RCP8.5 GCM runs used for IPCC AR5. Selected models which are used in this project for the climate change impact assessment are highlighted.	27
Figure 16: Schematic probability distribution of observation, control and future precipitation with the quantiles, excesses and biases denoted (from [<i>Kraaijenbrink, 2013b</i>], after [<i>van Pelt et al., 2012b</i>]).	29
Figure 17: Flowchart of the parameter calculation steps of the advanced delta change method [<i>Kraaijenbrink, 2013b</i>].	30
Figure 18: Flowchart of the transformation of the corrected observation time series by applying the coefficients [<i>Kraaijenbrink, 2013b</i>].	30
Figure 19: Transient timeseries for entire simulation period of downscaled average annual temperature averaged over the UIB. Upper panel shows RCP4.5 GCMs and lower panel shows RCP8.5 GCMs.	35
Figure 20: Mean temperature change for time slices 2031-2060 and 2071-2100 with respect to 1971-2000 according to GCM multi-model ensemble (left). The right panels show the standard deviation in temperature change of the entire multi-model ensemble.	36
Figure 21: UIB-averaged temperature change per month for 2031-2060 (left) and 2071-2100 (right) vs. 1971-2000. Upper panels are for RCP4.5 multi-model ensemble and lower panels are for RCP8.5 multi-model ensemble. The dots indicate the ensemble mean projection and the whiskers indicate the spread in projections within the entire ensemble.	37
Figure 22: Mean precipitation change for time slices 2031-2060 and 2071-2100 with respect to 1971-2000 according to GCM multi-model ensemble (left). The right panels show the standard deviation in temperature change of the entire multi-model ensemble.	39
Figure 23: UIB-averaged precipitation change per month for 2031-2060 (left) and 2071-2100 (right) vs. 1971-2000. Upper panels are for RCP4.5 multi-model ensemble and lower panels are for RCP8.5 multi-model ensemble. The dots indicate the ensemble mean projection and the whiskers indicate the spread in projections within the entire ensemble.	40
Figure 24: Model structure of SPHY model.	45
Figure 25: Schematic representation glacier related processes in the HI-SPHY model.	46



Figure 26 Schematic representation of snow related processes in the HI-SPHY model.....	47
Figure 27: Schematic representation of rainfall-runoff modelling in the HI-SPHY model	48
Figure 28: Left: Map showing DEM difference for glaciated areas in Shimshal valley 1999-2009 (provided by T. Bolch), and outlines of individual glaciers from the Randolph Glacier Inventory covering the analysed parts. Right: Box plots showing distributions of observed (1999-2009) and simulated (1999-2007) glacier mass balances for optimum parameter configuration.	50
Figure 29: Left panel: Observed and simulated average fractional snow cover in the entire UIB (left panel). The values represent the average for the 46 periods during 2000-2008. Right panel: The difference in fractional snow cover between simulated and observed.	52
Figure 30: Observed and simulated fractional snow cover in three subareas within the UIB (HI=Himalaya, HK=Hindu Kush, KK=Karakoram, see Figure 8). Red line shows the average observed for 2000-2008, blue line shows the average simulated for 2000-2007, green line shows the maximum simulated for 2000-2007 and the purple line shows the minimum simulated for 2000-2007.	52
Figure 31: Average snow cover 2000-2008 according to MODIS (a), and 2000-2007 according to SPHY (b). Error SPHY-MODIS (c), and Pearson coefficient SPHY vs MODIS (d)	53
Figure 32: Locations of gauging stations which records were used for calibration and/or validation of the SPHY model.....	54
Figure 33: Observed and simulated flow for gauging station locations used for model calibration.	55
Figure 34: Observed and simulated flow for gauging station locations used for model validation.	57
Figure 35: Average annual runoff generation in the UIB per 1x1 km model grid cell during the reference period, specified as total runoff (upper left panel) and per runoff component (other panels).....	59
Figure 36: Contributions of glacier melt (a), snow melt (b) and rainfall-runoff (c) to the total flow (magnitude indicated by symbol size) averaged over the reference period (1971-2000).....	60
Figure 37: Five subbasins in the UIB. Note that the Hunza basin upstream of Dainyor bridge and the Indus basin upstream of Skardu are part of the Indus basin upstream of Tarbela.	61
Figure 38: Simulated monthly averaged discharge and separation of runoff components for 1971-2000 at five locations in the UIB.	62
Figure 39: Projected changes in glacier extent for three subzones in the UIB. Left panel: Himalayas, middle panel: Karakoram, right panel: Hindu Kush. Projected changes for each multi-model ensemble member are shown.	63
Figure 40: Simulated monthly averaged discharge and separation of runoff components at five locations in the UIB for 2031-2060 for the RCP4.5 ensemble. The red line indicates the mean projection and error bars indicate spread in the ensemble output. The blue line indicates the reference situation.	66
Figure 41: Simulated monthly averaged discharge and separation of runoff components at five locations in the UIB for 2031-2060 for the RCP8.5 ensemble. The red line indicates the mean projection and error bars indicate spread in the ensemble output. The blue line indicates the reference situation.	67
Figure 42: Simulated monthly averaged discharge and separation of runoff components at five locations in the UIB for 2071-2100 for the RCP4.5 ensemble. The red line indicates the mean projection and error bars indicate spread in the ensemble output. The blue line indicates the reference situation.	68
Figure 43: Simulated monthly averaged discharge and separation of runoff components at five locations in the UIB for 2071-2100 for the RCP8.5 ensemble. The red line indicates the mean projection and error bars indicate spread in the ensemble output. The blue line indicates the reference situation.	68



Figure 44: Time series annual averaged discharge at five locations in the UIB for the entire simulated period (1961-2100). Until 2000, the results for the baseline climate run are shown. After 2000 the mean of the model forced with the RCP4.5 ensemble is shown with error bars marking the spread in output from the entire ensemble..... 69

Figure 45: Time series annual averaged discharge at five locations in the UIB for the entire simulated period (1961-2100). Until 2000, the results for the baseline climate run are shown. After 2000 the mean of the model forced with the RCP8.5 ensemble is shown with error bars marking the spread in output from the entire ensemble..... 70

Figure 46: Flow duration curves for five locations in the UIB for SPHY forced with all RCP4.5 ensemble members for 2031-2060. 73

Figure 47: Flow duration curves for five locations in the UIB for SPHY forced with all RCP4.5 ensemble members for 2071-2100. 74

Figure 48: Flow duration curves for five locations in the UIB for SPHY forced with all RCP8.5 ensemble members for 2031-2060. 75

Figure 49: Flow duration curves for five locations in the UIB for SPHY forced with all RCP8.5 ensemble members for 2071-2100. 76



1 Introduction

1.1 Background

High-resolution gridded meteorological datasets which capture the spatial variability of precipitation are critical for modelling the hydrology of high-mountain regions. In the Upper Indus Basin (UIB), previous modelling studies have demonstrated that snow and glacier melt are major contributors to stream discharge [Immerzeel *et al.*, 2010a; Lutz *et al.*, 2014a], and on daily or seasonal scales can play even larger roles. However, hydrological models suffer from a lack of gridded input climate data which accurately reflects the topographic complexity and spatial variability in precipitation. Improvements to existing gridded datasets using high-elevation station data will increase the reliability of hydrological models in the region.

Hydrological models are often poorly calibrated with respect to glaciers due to a lack of available information. Inaccuracies in precipitation estimation, for example, are often compensated by increased glacier melt [Schaeffli *et al.*, 2005], which produces the correct model result but for the wrong reason. With the incorporation of multiple lines of calibration data [Pellicciotti *et al.*, 2012], and improved gridded precipitation fields, hydrological models can be greatly improved.

It is highly likely that future climate change will impact future water availability in the UIB [Immerzeel *et al.*, 2010b, 2013a; Lutz *et al.*, 2014b], as temperature increases and changes in the timing, magnitude, and phase of precipitation will alter the timing and contribution of snow and ice melt [Shrestha and Aryal, 2010]. General Circulation Models need to be downscaled to provide appropriate input fields for estimating future water yields, and be used to generate hydrological forecasts for the UIB.

Climatic regimes differ substantially across the different mountain ranges in the Hindu-Kush Karakoram Himalaya (HKKH). The climate in the eastern Himalaya is dominated by monsoon dynamics, with the bulk of the annual precipitation occurring during summer. In the Hindu-Kush Karakoram (HKK) in the west, where the greater part of the UIB is located, precipitation also occurs during winter, having dominant influence on the cryospheric regime [Hewitt, 2011a].

1.2 Objectives and division of tasks

The main objectives of the project are:

- 1) To develop a high-quality meteorological forcing dataset (temperature and precipitation) for the UIB by merging existing gridded datasets and high-altitude climate observations.
- 2) To improve the existing large-scale SPHY model and recalibrating the model with additional observations (geodetic mass balance, time series of river runoff, time series of reservoir inflow data).
- 3) To use the recalibrated SPHY model to examine shifts in the basin hydrology under CMIP5 climate change scenarios.



To accomplish these objectives certain products produced by the project partners are required by FutureWater as outlined below:

- Daily meteorological data (T,P) from 1961-2007, in particular the high elevation stations in the UIB are provided by PMD
- River runoff and reservoir inflows for 1961-2007 for a number of locations in the UIB, especially long time series are provided by PMD
- Geodetic mass balance data from Shimshal Valley are provided by T. Bolch
- Downscaled CMIP5 climate change scenarios (four GCMs with two RCPs each (RCP4.5 and RCP8.5), daily time step, 10 km resolution are provided by PMD



2 Improving gridded meteorological data in the Upper Indus Basin

2.1 Existing gridded products

Understanding the spatial and temporal variability of precipitation in mountainous areas remains a key challenge. Point measurements are often not sufficient to capture the strong gradients in the multiple local factors that determine the distribution of precipitation. Climatologists have created numerous gridded datasets, based on observations. These datasets were developed to support climate research and have therefore many parameters at many elevations less interesting for water resources application. However, since a couple of products include precipitation and temperature at ground level, they can be used to overcome data gaps in observations.

A distinction in two groups can be made regarding gridded datasets for temperature and precipitation: (i) datasets based created using advanced geo-statistical interpolation techniques, and (ii) datasets based on climate models (often referred to as reanalysis products). Obviously, both approaches rely completely on the availability and quality of the observations used. In this section an overview of the available gridded datasets is provided. Only datasets covering the complete UIB are considered. A tabular overview of available datasets and their key characteristics is provided in Table 1. Apart from differences in the underlying methodology (interpolation of observations or reanalysis) the main differences in the datasets are the spatial resolution, temporal resolution and time span covered.

Table 1: Overview of gridded meteorological products.

Dataset	Type	Coverage	Resolution	Frequency	Period	Parameters	Institute
NCEP/NCAR reanalysis data	Re-analysis	Global	~209 km (T62 grid)	6 hourly	1948 - present	Prec, Tmax, Tmin, Tavg (+ many more)	NCEP/NCAR
CFSR	Re-analysis	Global	~ 50 km (0.5 degree)	1 hourly, 6 hourly, monthly	1979-2010	Prec, Tmax, Tmin, Tavg (+ many more)	NCEP
ERA 15 basic	Re-analysis	Global	basic: ~ 250 km (2.5 degrees)	monthly	1979 - 1994	Prec, Tmax, Tmin, Tavg (+ many more)	ECMWF
ERA 15 advanced	Re-analysis	Global	~ 120 km (N80 grid)	monthly	1979 - 1994		ECMWF
ERA 40 basic	Re-analysis	Global	~ 250 km (2.5 degrees)	6 hourly	1957 - 2002	Prec, Tmax, Tmin, Tavg (+ many more)	ECMWF
ERA 40 advanced	Re-analysis	Global	~ 120 km (N80 grid)	6 hourly	1957 - 2002	Prec, Tmax, Tmin, Tavg (+ many more)	ECMWF
ERA Interim	Re-analysis	Global	~ 70 km (N128 grid)	6 hourly	1979 - present	Prec, Tmax, Tmin, Tavg (ECMWF



						+ many more)	
ERA 20 CM	Climate model ensemble	Global	~ 120 km (N80 grid)	3 hourly	1900-2009	Prec, Tavg	ECMWF
NASA MERRA	Re-analysis	Global	~ 70 km (0.5 x 0.67 degrees))	3 hourly	1979 - present	Prec, Tmax, Tmin, Tavg (+ many more)	NASA
Global Meteorological Forcing Dataset for land surface modeling	Re-analysis + observations	Global	~ 50 km (0.5 degree)	3 hourly	1948 - 2008	Prec, Tmax, Tmin, Tavg (+ many more)	Princeton University
APHRODITE	Observations	Asia	~ 25 km (0.25 degree)	Daily	1961 - 2007	Prec, Tavg	Meteorological Research Institute of Japan Meteorological Agency
CRU TS 3.10.01	Observations	Global	~ 50 km (0.5 degree)	Monthly	1901-2009	Prec, Tmax, Tmin, Tavg (+ many more)	Climate Research Unit at the University of East Anglia
GPCC	Observations	Global	~ 50 km (0.5 degree)	Monthly	1901-2007	Precipitation	Global Precipitation Climatology Centre
GPCP	Observations	Global	~ 250 km (2.5 degrees)	Monthly	1979 - present	Precipitation	GEWEX
CPC-UGBAGDP	Observations	Global	~ 50 km (0.5 degree)	Daily	1979-present	Prec	CPC
DEL	Observations	Global	~ 50 km (0.5 degree)	monthly	1900-2008	Prec, Tair	CCR Univ of Delaware

A thorough comparison on the performance of existing gridded products for the HKH region [Palazzi *et al.*, 2013a] highlights the striking differences between the different products. All the currently available products are subject to limited spatial resolution. They are mostly suitable for large-scale continental studies. However, to analyse climate variations at smaller scales and in orographically complex regions, such as the UIB, they lack accuracy.

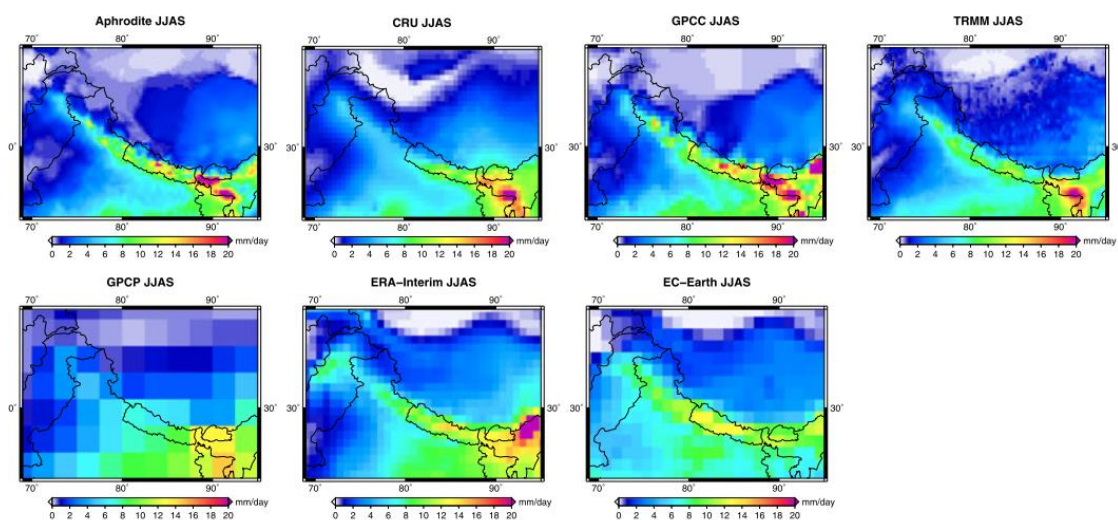


Figure 1: Multiannual mean (1998-2007) of summer (JJAS) precipitation over the HKKH region as represented by different dataset [Palazzi *et al.*, 2013b].



As illustrated in Figure 1 and Figure 2 the APHRODITE product [Yatagai *et al.*, 2012a] has the highest spatial resolution, while at the same time capturing the winter precipitation (Figure 2), which is very important in the UIB, reasonably well compared to the other products. Researches who compared the performance of TRMM and APHRODITE over Nepal concluded that the latter is the more accurate dataset [Duncan and Biggs, 2012]. Other researchers also concluded that there is large variability in performance between different gridded products by comparing them for multiple transects crossing the Himalayan ranges [Andermann *et al.*, 2011]. They also conclude that APHRODITE, based on ground station data solely, gives the best precipitation estimates. However, they also mention that the lack of stations at high elevations limits the accuracy of this dataset. Since the APHRODITE product is considered to be the best performing gridded dataset over Asia's high mountain regions, we select this dataset as a basis to construct an improved gridded meteorological dataset for the UIB.

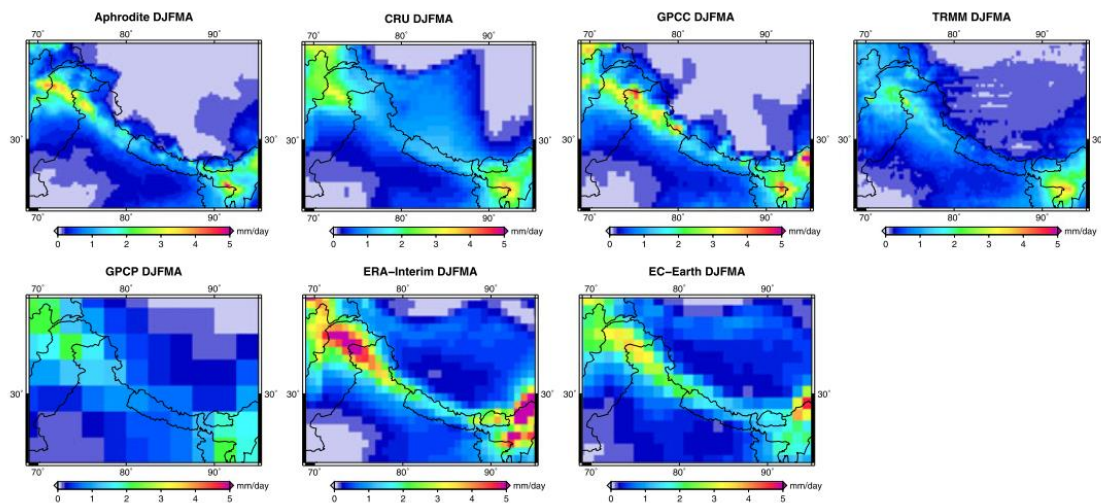


Figure 2: Multiannual mean (1998-2007) of winter (DJFMA) precipitation over the HKH region as represented by different dataset [Palazzi *et al.*, 2013].

2.2 Shortcomings in APHRODITE product

As mentioned in the previous section, the performance of the APHRODITE product over mountainous areas is limited by the scarcity of representative ground station data. Apart from a general sparser distribution of ground stations in mountainous areas in comparison to the flatter land areas, the ground stations do not represent the entire range of altitude present in the mountains, while altitude is an important controlling factor of the precipitation amount. The ground observations in the UIB are sparse and are mainly located in the valleys. In mountainous meteorology, vertical lapse rates are important characteristics of climatic variables such as air temperature and especially precipitation. The vertical temperature lapse rate is largely dependent on the moisture content of the air and generally varies between the dry adiabatic lapse rate ($-0.0098 \text{ } ^\circ\text{C m}^{-1}$) and the saturated adiabatic lapse rate (typically $-0.005 \text{ } ^\circ\text{C m}^{-1}$, strongly dependent on the temperature). Thus, vertical temperature lapse rates tend to decrease with elevation as the air gets dryer with altitude [Tahir *et al.*, 2011a]. This may not be well represented in the ground station data as the stations are located in the valley bottoms. Precipitation also varies greatly over short horizontal distances in mountain areas and although APHRODITE is considered to be the best performing precipitation dataset for the Himalayas, strong vertical lapse rates have been reported, in particular in the Karakoram in the upper Indus basin [Hewitt, 2005a, 2011b; Winiger *et al.*, 2005a].



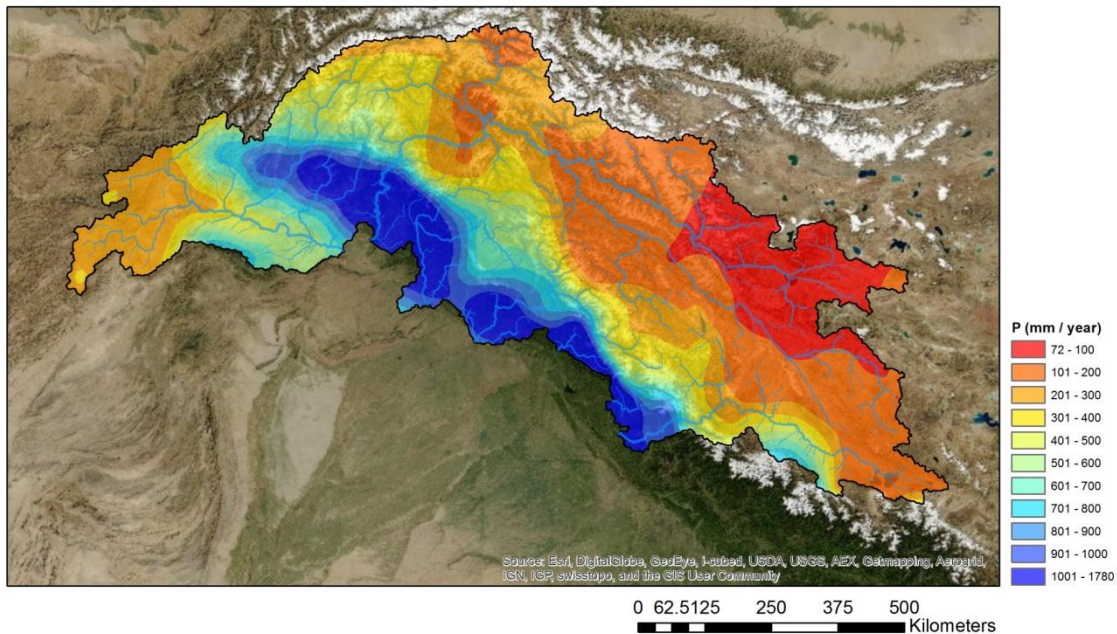


Figure 3: Annual precipitation in the upper Indus Basins (APHRODITE 1998-2007).

Figure 3 shows the annual precipitation in the UIB as derived from APHRODITE. Averaged over the entire upstream basin the annual precipitation is ~400 mm. The map shows strong gradients with high precipitation downstream and decreasing precipitation upstream. Behind the Himalayan ranges, in the Karakoram, APHRODITE is very dry, while at the same time the largest glaciers systems persist in that area, which require a lot of precipitation to be sustained. One way to check the performance of the gridded precipitation product is to compare the precipitation averaged over a catchment area to the observed discharge at the outlet of the catchment.

For example, the observed mean annual discharge observed at the outlet of the Hunza basin equals 767.3 mm yr^{-1} (Table 2). According to APHRODITE (Figure 3), the annual precipitation equals $\sim 200\text{-}300 \text{ mm yr}^{-1}$. Thus, the amount of water discharged from the catchment is more than double the amount of precipitation, even without accounting for losses due to evapotranspiration, sublimation and infiltration to the groundwater. As another example, the observed annual discharge at Besham, near the outlet of the UIB equals 458.3 mm yr^{-1} , while the observed annual precipitation equals $300\text{-}400 \text{ mm yr}^{-1}$. This indicates that the underestimate in precipitation is smaller further downstream. Negative glacier mass balances could explain the difference between observed discharge and observed precipitation, but these are generally neutral or only slightly negative for the Karakoram. Thus the high altitude precipitation is underestimated significantly in the APHRODITE product.

Table 2: Long-term annual average runoff for different subbasins in the upper Indus basin
[Sharif *et al.*, 2013b].

Stn. No.	River	Station	Period of available record	Basin area km ²	Mean elevation m	Area above 5000 m %	Mean flow m ³ s ⁻¹	Annual Runoff mm yr ⁻¹	Median SOT	Median CoV
(a) Gauging stations with available daily records										
Catchments with predominantly glacial melt regime										
1	Shyok	Yogo	1973–1997	33 350*	4900	46.2	347.1	328.4	12 Jun	1 Aug
2	Hunza	Dainyore	1966–1997	13 925	4472	35.8	338.6	767.3	4 Jun	29 Jul
Catchments with predominantly seasonal snowmelt regime										
3	Indus	Kharmong	1982–1997	72 500	4755	36.7	489.1	212.9	18 May	15 Jul
4	Gilgit	Gilgit	1960–1998	12800	3740	2.9	281.9	694.7	26 May	19 Jul
5	Astore	Doyian	1974–1997	3750	3921	2.8	136.8	1150.0	4 Jun	19 Jul
6	Chitral	Chitral	1964–1996	12 425	3794	8.1	271.9	690.0	29 May	25 Jul
7	Swat	Kalam	1961–1997	2025	3300	0.3	89.6	1395.9	5 May	8 Jul
8	Kunhar	Naran	1960–1998	1175	3700	0.0	48.1	1290.4	5 May	1 Jul
Main river catchments with mixed glacial and seasonal snowmelt regime										
9	Indus	Kachura	1970–1997	115 289*	4789	40.2	1069.1	292.6	26 May	25 Jul
10	Gilgit	Alam Br	1966–1998	27 525	4094	18.1	644.0	737.9	29 May	24 Jul
11	Indus	Partab Br	1962–1996	145 618*	4656	36.2	1775.8	384.8	28 May	25 Jul
12	Indus	Besham	1969–1997	166 096*	4505	32.6	2412.2	458.3	22 May	21 Jul
Catchments with mixed seasonal snowmelt and spring or monsoon rainfall										
13	Swat	Chakdara	1961–1997	5400	2499	0.14	178.9	1044.8	12 Apr	29 Jun
14	Khan Khwar	Karora	1975–1996	625	1906	0.0	21.2	1071.6	8 Mar	2 Jun
15	Kunhar	Garhi Habibullah	1960–1998	2400	3061	0.0	101.8	1337.4	19 Apr	27 Jun
16	Neelum	Muzafferabad	1963–1995	7392	3215		357	1524.0	6 Apr	13 Jun
(b) Additional stations with available monthly records (mixed seasonal snowmelt and monsoon rainfall)										
17	Jhelum	Chinari	1970–1995	13775	2437		330	756.0		
18	Jhelum	Kohala	1965–1995	25000	2629		828	1045.2		
19	Poonch	Kotli	1960–1995	3176	1805		134	1333		

2.3 Station observations

Station observations in the UIB are sparse. Figure 4 and Table 3 list the stations and station metadata, including record length, as available in this project. As evident from the map, the stations are very unequally distributed over the basin and mostly located in the valleys. As can be seen in the table, only three out of twenty stations are located above 4000 m a.s.l., with the highest being located at an elevation of 4730 m a.s.l. In addition, many stations have rather short records available. The locations of stations carrying IDs 6 and 19 could not be verified and are therefore excluded from further analysis.



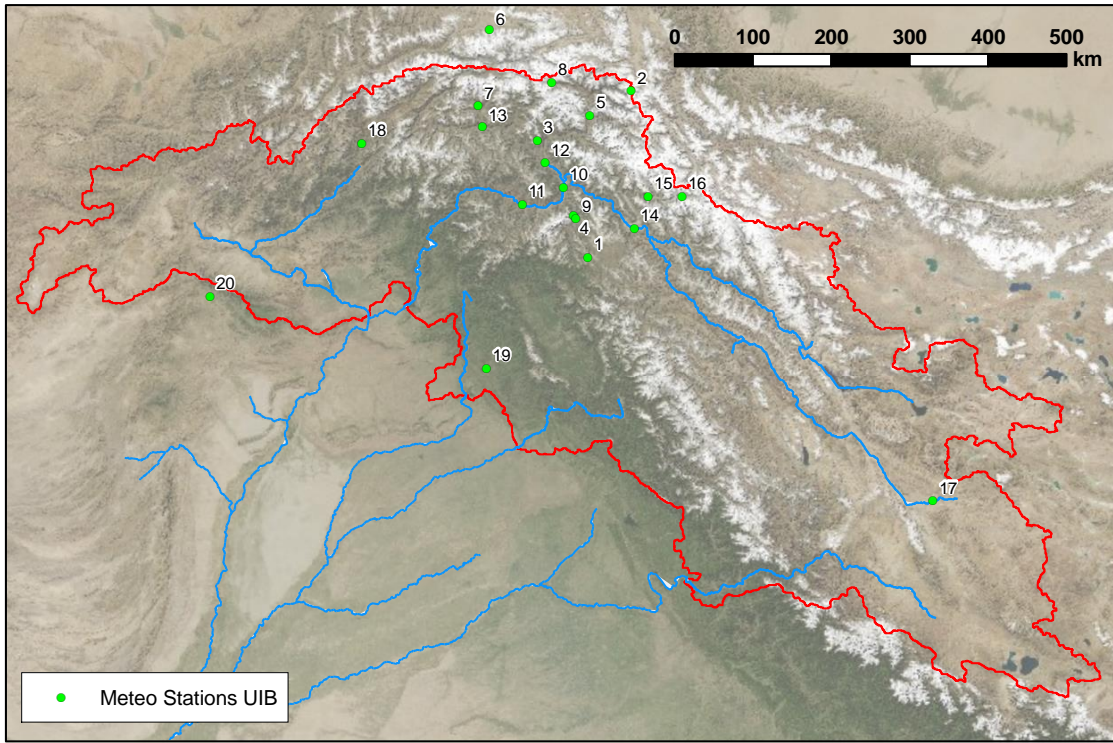


Figure 4: Meteorological ground stations in the upper Indus basin.

Table 3: Meteorological ground station records in the UIB.

ID	Name	Source	Lon (dd)	Lat (dd)	Elevation (masl)	StartDate	EndDate	Tmax	Tmin	Tavg	P
1	Burzil	WAPDA	75.088	34.911	4030	01/01/1999	31/12/2008	daily	daily	Average of Tmax and Tmin	daily
2	Khunjerab	WAPDA	75.400	36.850	4730	01/01/1999	31/12/2008	daily	daily	Average of Tmax and Tmin	daily
3	Naltar	WAPDA	74.189	36.158	2810	01/01/1999	31/12/2008	daily	daily	Average of Tmax and Tmin	daily
4	Rama	WAPDA	74.817	35.367	3000	01/01/1999	31/12/2008	daily	daily	Average of Tmax and Tmin	daily
5	Rattu	WAPDA	74.871	36.515	2570	01/01/1999	31/12/2008	daily	daily	Average of Tmax and Tmin	daily
6	Ushkore	WAPDA	73.300	37.333	2977	01/01/1999	31/12/2008	daily	daily	Average of Tmax and Tmin	daily
7	Yasin	WAPDA	73.300	36.450	3150	01/01/1999	31/12/2008	daily	daily	Average of Tmax and Tmin	daily
8	Ziarat	WAPDA	74.276	36.836	3669	01/01/1999	31/12/2008	daily	daily	Average of Tmax and Tmin	daily
9	Astore	PMD	74.857	35.329	2168	01/01/2000	31/12/2005	daily	daily	Average of Tmax and Tmin	daily
10	Bunji	PMD	74.633	35.667	1470	01/01/2000	31/12/2005	daily	daily	Average of Tmax and Tmin	daily
11	Chilas	PMD	74.100	35.417	1251	01/01/1991	31/12/2005	daily	daily	Average of Tmax and Tmin	daily
12	Gilgit	PMD	74.333	35.917	1459	01/01/2000	31/12/2005	daily	daily	Average of Tmax and Tmin	daily
13	Gupis	PMD	73.400	36.230	2156	01/01/1991	31/12/2005	daily	daily	Average of Tmax and Tmin	daily
14	Skardu	PMD	75.680	35.300	2210	01/01/1991	31/12/2005	daily	daily	Average of Tmax and Tmin	daily
15	Askole	CEOP	75.815	35.681	3015	10/08/2005	31/12/2007	daily	daily	Average of hourly Tair	daily
16	Urdukas	CEOP	76.286	35.728	3927	06/17/2004	31/12/2007	daily	daily	Average of hourly Tair	daily
17	Shiquanhe	China	80.080	32.500	4278	01/01/1961	31/12/2006	no	no	daily	no
18	Chitral	PMD	71.780	35.839	1500	01/01/1991	01/01/2005	no	no	no	daily
19	Kotli	PMD	73.900	33.520	2017	01/01/1991	01/01/2005	no	no	no	daily
20	Parachinar	PMD	70.083	33.867	1726	01/01/1991	01/01/2005	no	no	no	daily

2.4 Methods

Since the amounts of precipitation in the ground station data and APHRODITE product are underestimated it is very likely that the precipitation necessary to supply the observed amount of discharged water is occurring at high altitudes. Research in this area [*Batura Investigations Group,* 1979; *Hewitt,* 2005b, 2007a, 2011b; *Winiger et al.,* 2005b] suggests that precipitation increases up to 5000 to 6000 m a.s.l., where it is at its maximum, and decreases at higher altitudes (Figure 5, right panel).

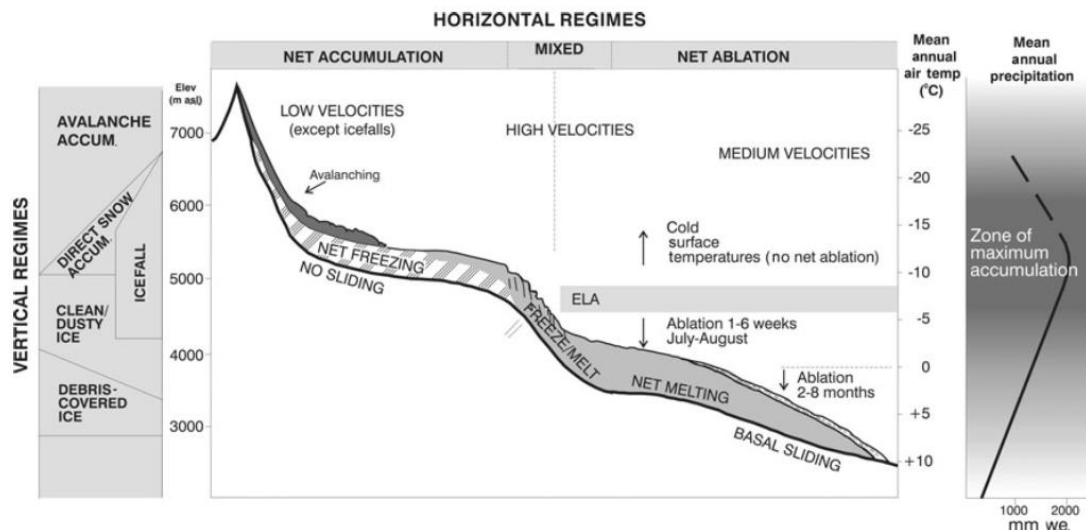


Figure 5: Conceptual model of vertical and horizontal meteorological and cryospheric regimes in the Karakoram [Hewitt, 2007b].

In the construction of an improved gridded meteorological dataset for the upper Indus basin we assume this conceptual model to be correct to infer vertical precipitation lapse rates based on a linear increase of precipitation up to 5500 m a.s.l., and decreasing linearly at higher altitudes with the same lapse rate.

In summary, the methodology to improve the data for air temperature and precipitation is as follows:

- APHRODITE air temperature and precipitation data are used as basis
 - Air temperature (step 1):
 - Temperature fields are initially corrected using elevation-dependent temperature lapse rates
 - The bias between ground observations and APHRODITE is determined
 - A monthly relation between bias and elevation is derived
 - Temperature fields are corrected using the bias-elevation relation
 - Precipitation (step 2):
 - Using the improved APHRODITE temperature fields (result of step 1), the observed glacier mass balance is included as a proxy to derive local precipitation lapse rates
 - Local precipitation lapse rates are spatially interpolated
 - Interpolated field of precipitation lapse rates is used to correct the original precipitation grids



2.4.1 Correction of air temperature

As a first step, the APHRODITE air temperature fields are corrected by applying elevation-dependent temperature lapse rates and bias-correction using ground station data. In the APHRODITE dataset a uniform vertical temperature lapse rate is assumed ($-0.0065 \text{ }^\circ\text{C m}^{-1}$) [Yatagai *et al.*, 2012b]. However, the vertical temperature lapse rate is largely dependent on the moisture content of the air and generally varies between the dry adiabatic lapse rate ($-0.0098 \text{ }^\circ\text{C m}^{-1}$) and the saturated adiabatic lapse rate (typically $-0.005 \text{ }^\circ\text{C m}^{-1}$, strongly dependent on the temperature). Thus, vertical temperature lapse rates tend to decrease (get stronger) with elevation as the air gets dryer with altitude. We apply different temperature lapse rates for different elevation zones as determined in another UIB hydrological modeling study (Table 4).

Table 4: Vertical temperature lapse rates per altitudinal zone [Tahir *et al.*, 2011b].

Altitudinal zone	Lapse rate ($^\circ\text{C m}^{-1}$)
< 3500 m	-0.0048
3500 – 4500 m	-0.0064
> 4500 m	-0.0076

Subsequently, the temperature bias between the ground stations (section 2.3) and the temperature grids are determined, for stations with records covering 2003-2007 (14 stations). In Figure 6, the bias is plotted for twelve months. As it is evident from the figure, the bias shows a strong seasonal pattern. During the winter months, APHRODITE generally underestimates the observed air temperature, while during the monsoon months APHRODITE tends to overestimate observed air temperature. This seasonal pattern can most likely be attributed to variations in the moisture content in the air. During the monsoon, the air is moist and vertical temperature lapse rates are therefore weaker than during winter months, when the air is dryer.

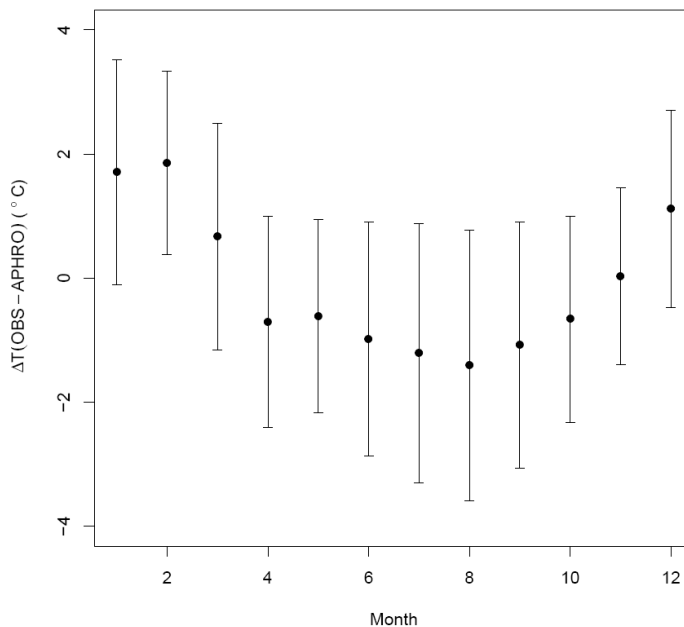


Figure 6: Bias between observed temperatures and gridded temperatures per month. Dots represent the average bias for 14 stations. Error bars represent the complete range of bias for 14 stations.



Thus, for the bias between observed and gridded air temperature, a seasonal dependency occurs. However, a second determinant for the bias can be distinguished. Figure 7 shows the bias between observed and gridded temperature as a function of station elevation for each month. For each month the bias (Observation minus APHRODITE) is decreasing with elevation. Also the previously mentioned seasonal effect can be distinguished in this figure, as the fitted linear relation is steeper during the monsoon months compared to the winter months. Thus a dependency of the bias is present for seasons, as well as for elevation and we correct the original APHRODITE gridded temperature for both effects.

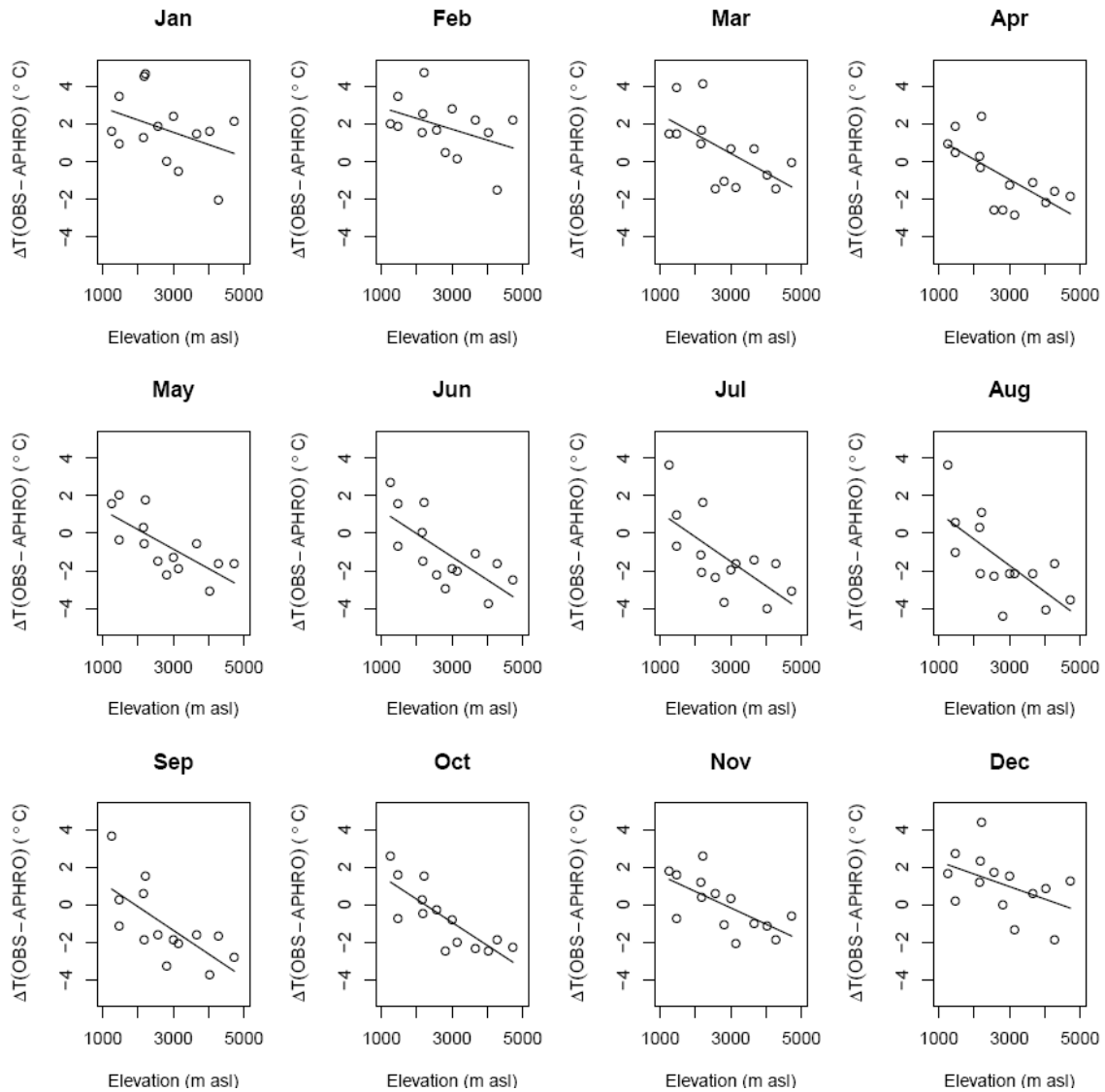


Figure 7: Bias between observations and gridded temperature per month and by station elevation.

We correct the APHRODITE gridded temperature on a monthly scale for both effects by applying the linear correction functions as visible in Figure 7.

For each day in the original dataset running from 1 January 1961 to 31 December 2007, this is done for each grid cell:

$$T_{COR(x,y)} = T_{APHRO(x,y)} + a \cdot H_{(x,y)} + b$$



where T_{COR} is the corrected temperature, T_{APHRO} is the original gridded temperature, H is the grid cell elevation according to the SRTM Digital Elevation Model [Farr *et al.*, 2007], and a and b are monthly coefficients as determined from the fitted functions in Figure 7. The corrected temperature datasets can in turn be used for the correction of the precipitation data.

2.4.2 Correction of precipitation data

To correct the precipitation data we use the observed glacier mass balance to derive precipitation lapse rates for each individual glacier system, as applied before in the Hunza basin [Immerzeel *et al.*, 2012]. As the glaciers in the upper Indus basin cannot persist without precipitation input being much higher than observed in the APHRODITE grids, we can use the glacier mass balance to derive the amount of precipitation that would be necessary to sustain the observed glacier mass balance.

Based on the conceptual model in Figure 5 we assume that precipitation increases linearly with elevation up to 5500 m a.s.l. and decreases with the same lapse rate above 5500 m a.s.l.:

$$P_{COR}(x, y) = P_{APHRO}(x, y) \cdot (1 + ((h(x, y) - h_r(x, y)) \cdot \gamma \cdot 0.01))$$

for $h < 5500$ m, and:

$$P_{COR}(x, y) = P_{APHRO}(x, y) \cdot \left\{ 1 + \left(\left((5500 - h_r(x, y)) + (5500 - h(x, y)) \right) \cdot \gamma \cdot 0.01 \right) \right\}$$

for $h \geq 5500$ m

where P_{COR} is the corrected precipitation, P_{APHRO} is the precipitation according to APHRODITE, h_r is a reference elevation from which precipitation gradients occur, which is assumed to be 2500 m a.s.l. in this study, h is the elevation for the grid cell, and γ is the precipitation gradient ($\% \text{ m}^{-1}$).

To calculate the precipitation gradients for individual glacier system, we select all glacier systems that have an area $> 5 \text{ km}^2$, which are 550 individual systems in the UIB. Since only few glaciers are field-monitored in the UIB, which would not yield a representative glacier mass balance for the entire glacier population, we use regional glacier mass balances as derived using IceSat data for 2003-2008 [Kääb *et al.*, 2012a]. The regional mass balance data for three sub-zones in the UIB were made available (Figure 8). It is evident from these data that the glacier mass loss is much stronger in the Himalaya ($-0.49 \text{ m w.e. yr}^{-1}$) than in the Karakoram ($-0.07 \text{ m w.e. yr}^{-1}$).

A glacier's mass balance is determined by the amount of accumulation and the amount of ablation:

$$\Delta M = C - A$$

where C is the accumulation and A is the ablation. For each of the 550 glacier systems the ablation can be determined using a degree day melt model forced with the corrected gridded temperature fields. This can be done quite straightforward by using the glacier outlines from a glacier inventory [Bajracharya and Shrestha, 2011] as a potential melting surface. Calculating the glacier accumulation is a bit more complex, since the accumulation area of a glacier is often



not entirely included in the glacier outlines in a glacier inventory. Especially in the Karakoram, the glacier accumulation consists for large part of snow fed to the glacier surface by avalanching. To include this, we assume the accumulation area of a glacier system to include the grid cells covered by the glacier outline from the glacier inventory and in addition the adjacent grid cells that have their “drain” direction to the glacier surface and have a slope steeper than 0.20 m m^{-1} . This slope threshold is estimated from the slope distribution of the glacierised area in the UIB.

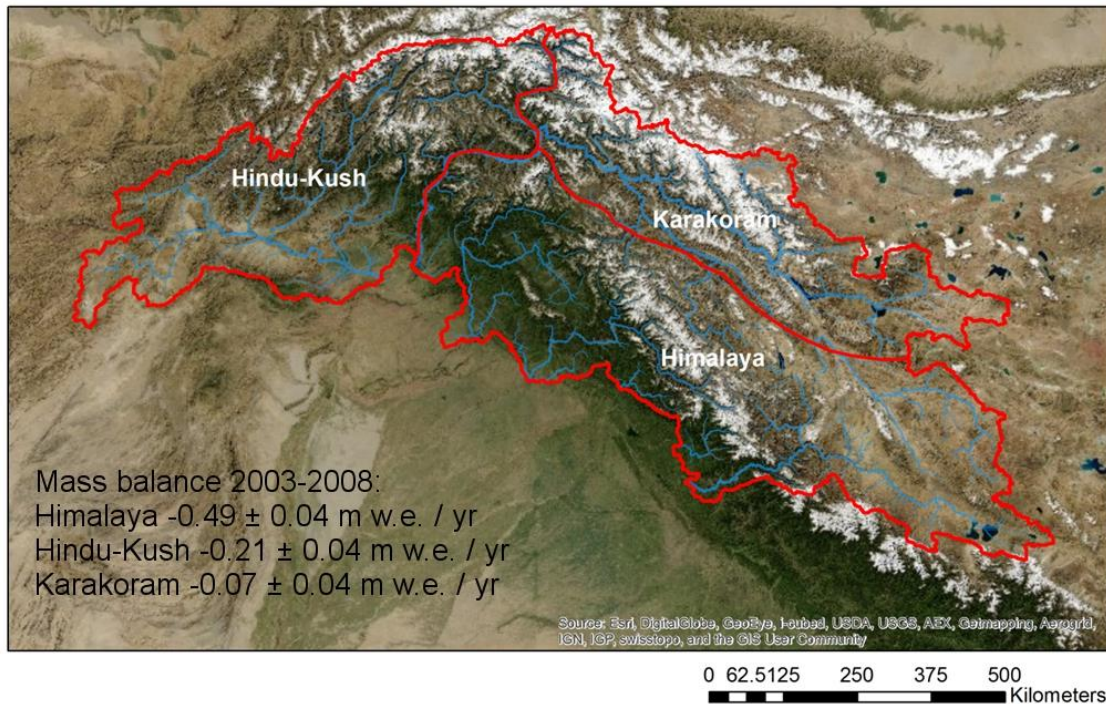


Figure 8: Regional glacier mass balance for three subzones in the UIB for 2003-2008 as derived using IceSat [Kääb et al., 2012b].

Since the glacier mass balance is known and the ablation can be calculated using the melt model, we can derive for each individual glacier system which amount of precipitation would be required in the accumulation area to sustain the observed mass balance. Thus, we can derive for those glacier systems, which precipitation gradient is appropriate to correct the original precipitation field to match the amount of precipitation necessary to sustain the mass balance (Figure 9).



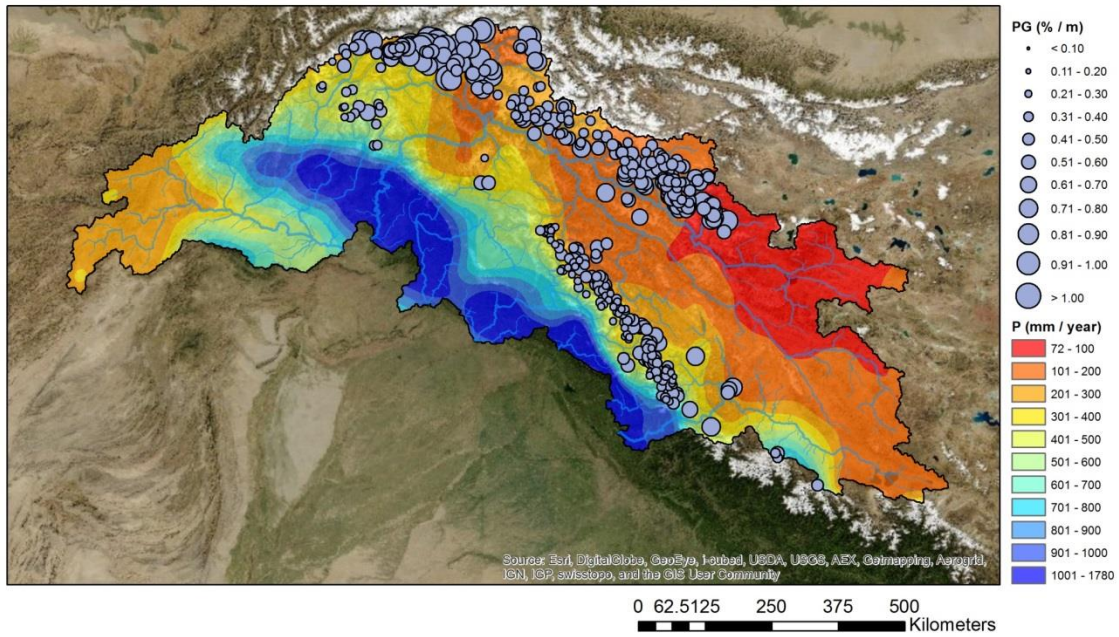


Figure 9: Estimated precipitation gradients at the locations of individual glacier systems in the UIB. The precipitation field on the background is the annual precipitation according to the original APHRODITE data 1998-2007.

As can be observed in Figure 9, this reveals a striking pattern with strongest precipitation gradients in the far north of the UIB and mainly smaller precipitation gradients in the southern glacierized areas. By spatially interpolating these precipitation gradients we obtain a correction grid that covers the entire UIB and can be used to correct the entire APHRODITE precipitation dataset from 1 January 1961 to 31 December 2007.

2.5 Corrected gridded air temperature dataset

Figure 10 shows the average air temperature for 1961-2007 for the original APHRODITE dataset and the bias-corrected air temperature dataset. The difference between the two datasets is shown in the lower panel. The bias-corrected dataset has been corrected at the monthly scale for the observed relation of the bias between station data and the APHRODITE mean air temperature product. From the lower panel in Figure 10 it is clear that at the temperature data for low elevations has increased for the corrected dataset whereas it has decreased for the higher elevations.

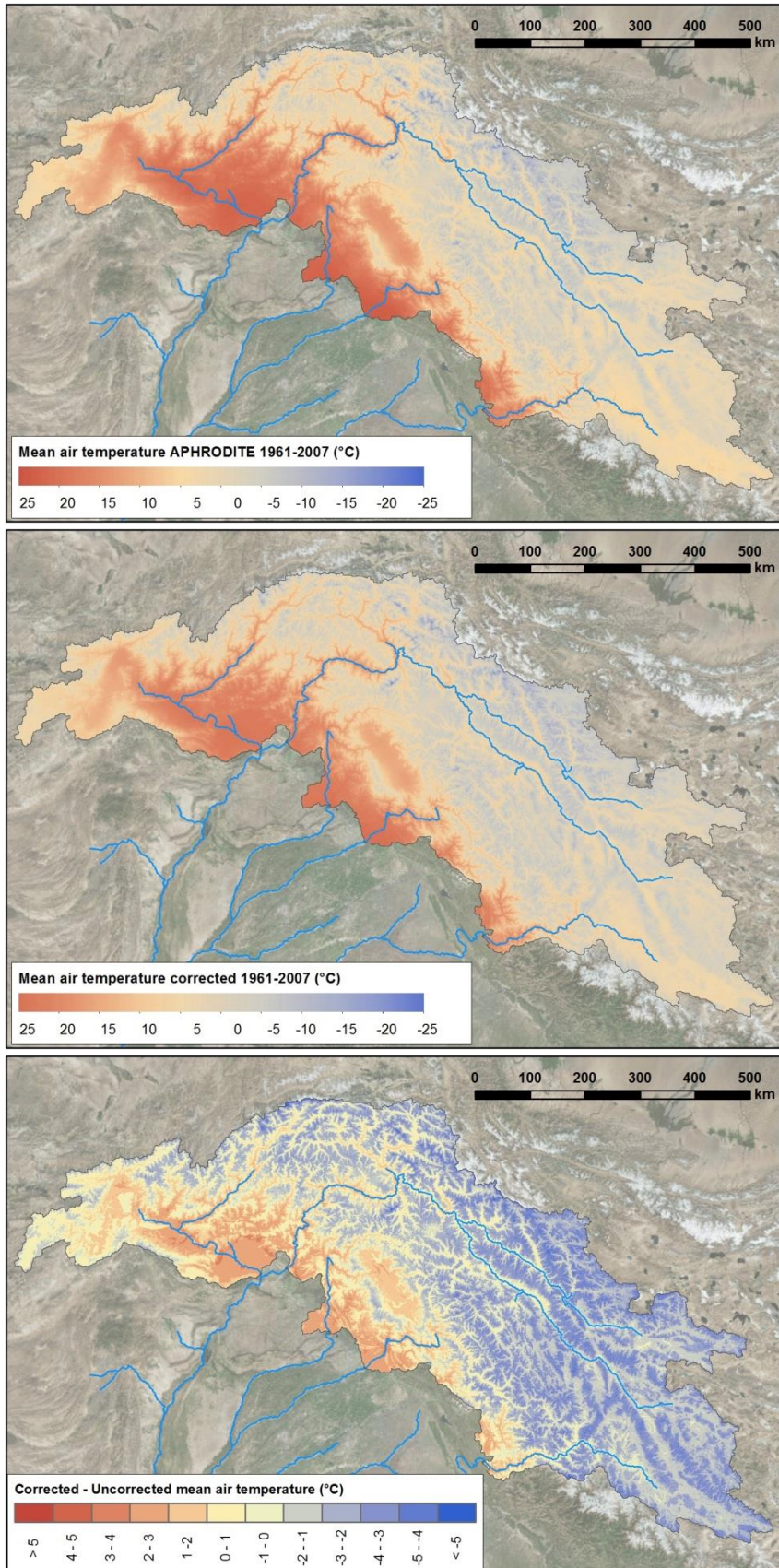


Figure 10: Mean air temperature 1961-2007 according to APHRODITE (upper panel) and the corrected dataset (middle panel). Lower panel shows the difference between the corrected dataset and the uncorrected dataset.



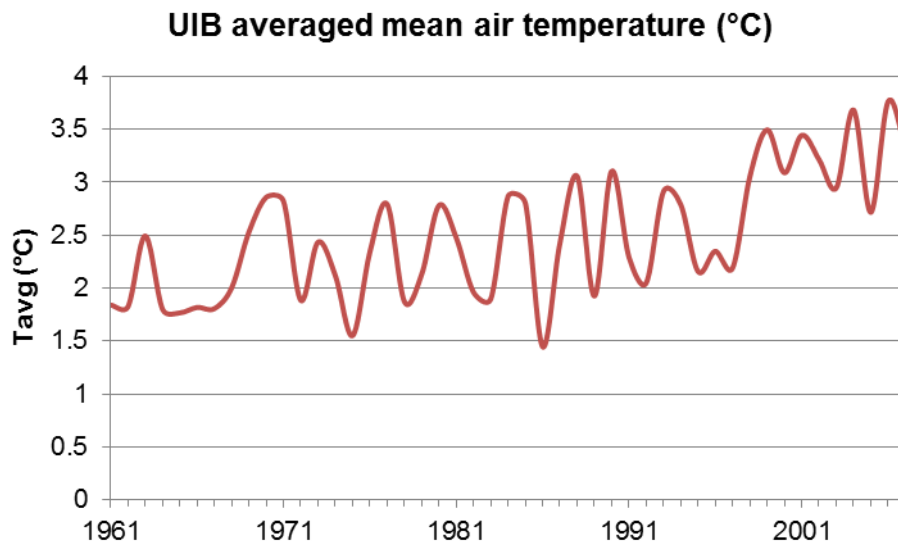


Figure 11: UIB averaged mean air temperature 1961-2007.

2.6 Corrected gridded precipitation dataset

Figure 12 shows for 1998-2007 how annual precipitation differs between uncorrected APHRODITE and the corrected data. Averaged over the entire UIB, the corrected precipitation data has an average precipitation sum of 913 mm yr^{-1} , which is more than double the 437 mm yr^{-1} in the uncorrected product. In the most extreme case, precipitation is underestimated by a factor 5 to 10 in the region where the Pamir, Karakorum and Hindu-Kush ranges intersect (lower panel). The large glacier systems in the region can only be sustained if snowfall in their accumulation areas is around 2000 mm yr^{-1} . This is in sharp contrast to precipitation amounts around $200 - 300 \text{ mm yr}^{-1}$ that is reported by uncorrected APHRODITE. The highest precipitation amounts are found along the monsoon-influenced southern Himalayan arc with values over 3000 mm yr^{-1} , while north of the Himalayan range the precipitation decreases quickly towards a vast dry area in the north-eastern part of the UIB (Shyok sub-basin).

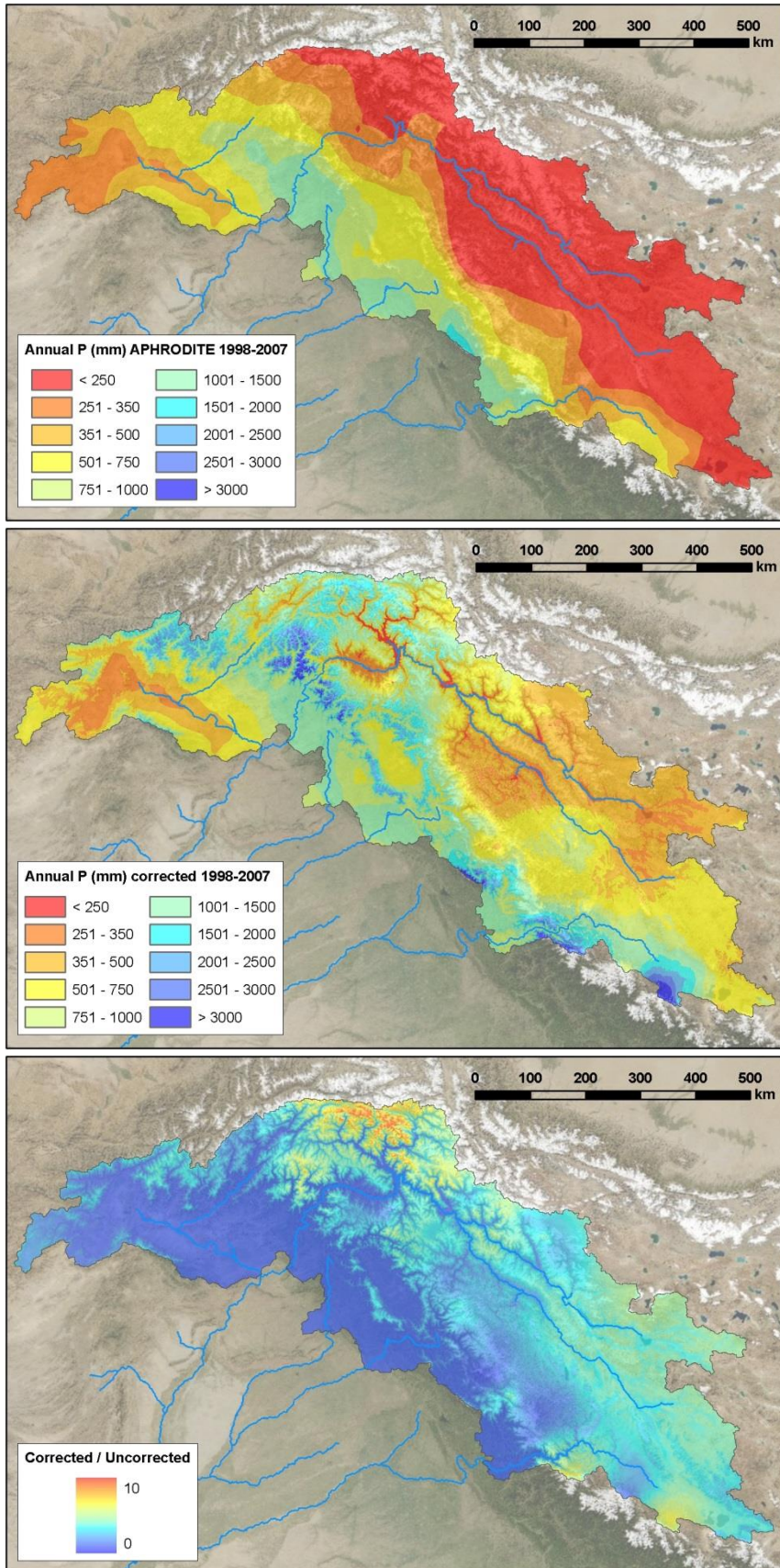


Figure 12: Average annual precipitation 1998-2007 according to APHRODITE (upper panel) and the corrected dataset (middle panel). Lower panel shows the ratio of the corrected dataset over the uncorrected dataset.



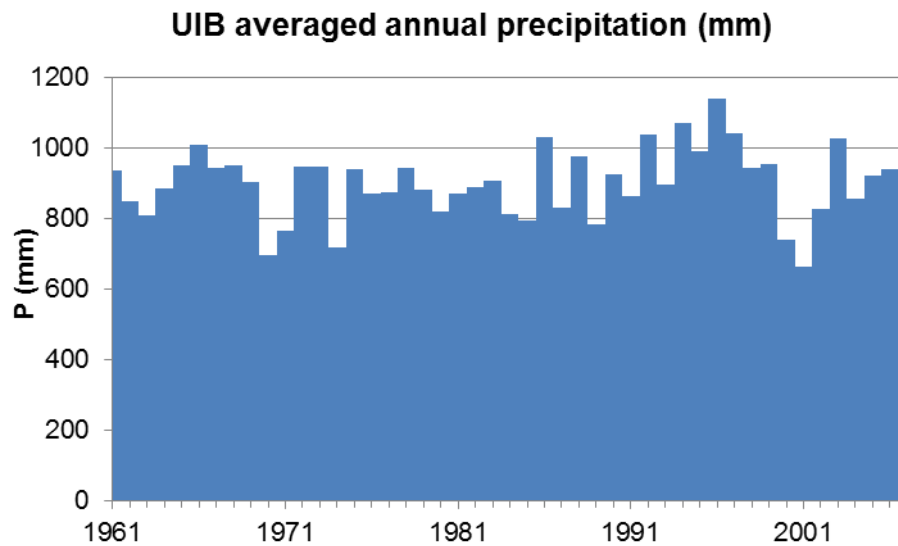


Figure 13: UIB averaged annual precipitation 1961-2007.

2.7 Validation to observed runoff

The supposed improvement in the corrected dataset versus the uncorrected data can be validated to discharge observations. Annual average discharge values have been published for multiple long-term records [Archer, 2003a; Khattak et al., 2011a; Sharif et al., 2013a]. We compare observed and calculated runoff for 18 stations with a catchment area larger than 5000 km² (Table 5). The runoff estimates (precipitation – evapotranspiration + mass balance) based on the corrected precipitation agree much better with the average observed annual runoff (Figure 14). The runoff estimated for the uncorrected APHRODITE dataset is consistently lower than the observed runoff, and in some occasions even negative. This confirms that these products underestimate precipitation considerably, and that the applied corrections form a large step forward in improving the meteorological forcing for the UIB.

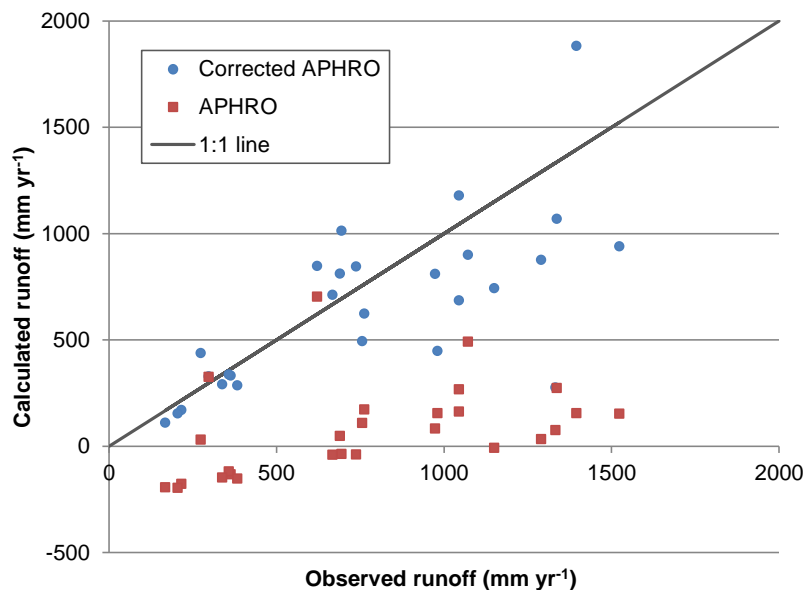


Figure 14: Calculated runoff vs observed runoff for multiple gauged catchments in the UIB. Results are shown for uncorrected APHRODITE and corrected APHRODITE.



Table 5: Observed discharge in the UIB. Data originates from PMD and WAPDA as published in scientific literature [Archer, 2003b; Sharif et al., 2013b].

Station	Latitude	Longitude	Area (km ²)	Observed Q (mm y ⁻¹)	Period
Besham Qila	34.91	72.87	198741	364	2000-2007
Tarbela inflow	34.33	72.86	203014	358	1998-2007
Mangla inflow	33.20	73.65	29966	762	1998-2007
Marala inflow	32.67	74.46	29611	981	1998-2007
Dainyor bridge	34.01	71.98	95803	667	1998-2004
Partab Bridge	35.43	75.47	146200	383	1962-1996
Yogo	35.77	74.60	177622	168	1973-1997
Kharmong	35.18	76.10	64240	205	1982-1997
Gilgit	34.93	76.22	70875	695	1960-1998
Doyian	35.93	74.30	13174	1150	1974-1997
Kalam	35.87	71.78	12824	1396	1961-1997
Chakdara	35.77	74.60	28201	1045	1961-1997
Karora	34.65	72.02	5990	1072	1975-1996
Chinari	34.43	73.49	7604	756	1970-1995
Kohala	34.16	73.83	14248	1045	1965-1995
Kotli	34.09	73.50	25820	1333	1960-1995
Phulra	35.42	75.73	6681	622	1969-1996
Shatial Bridge	34.10	71.30	74092	338	1983-1997



3 Future Climate

Knowledge about the future climate is necessary to generate estimates of changes in the future hydrological regime. Based on the latest ensemble (CMIP5 [Taylor *et al.*, 2012]) of General Circulation Models (GCMs), that was used to generate the most recent IPCC Assessment Report (AR 5) [IPCC, 2013], a selection of GCMs is made, which are used to generate climatological forcing for the SPHY model runs that are conducted for the future until 2100. This chapter describes how a representative ensemble of GCMs was selected, how the downscaling was performed and summarizes the future climatic changes.

3.1 Selection of General Circulation Models

The procedure for the selection of GCMs is similar as in the work FutureWater did for ICIMOD in the Himalayan Climate Change Adaptation Programme (HICAP) project [Immerzeel and Lutz, 2012; Lutz and Immerzeel, 2013; Lutz *et al.*, 2014b]. Figure 15 shows the average change in temperature and precipitation between 2071-2100 and 1961-1990 for all GCM grid cells covering the Upper Indus basin, for all RCP4.5 and RCP8.5 GCM runs that were used for IPCC AR5. These values were calculated for the GCM grid cells that cover the Upper Indus basin.

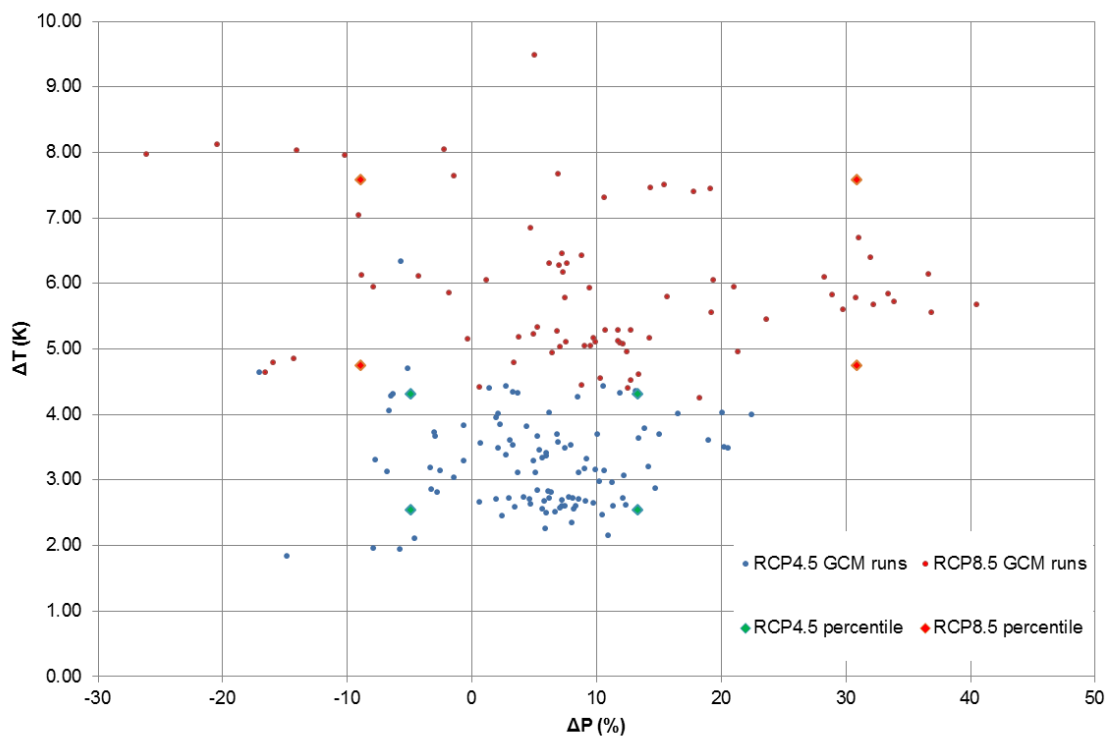


Figure 15: Average temperature and precipitation change in the Upper Indus basin (2071-2100 with respect to 1961-1990) for all RCP4.5 and RCP8.5 GCM runs used for IPCC AR5. Selected models which are used in this project for the climate change impact assessment are highlighted.

Based on the average changes in temperature and precipitation, for both RCP4.5 and RCP8.5, four GCM runs are selected. The four GCM runs are selected such that they cover the 10th to 90th percentile space in the range of projections of temperature and precipitation. The values corresponding to the 10th and 90th percentile of the projections for precipitation and temperature are listed in column 3 and 4 in Table 6. The GCM runs with the delta values closest to these



reported values are then selected. The delta values for precipitation and temperature according to the selected GCM runs are listed in columns 6 and 7 in Table 6.

Table 6: Selected GCM runs for ensemble of RCP4.5 and RCP8.5 GCMs.

Description	RCP	dP (%)	dT (K)	Selected model run	selected model dP	selected model dT
DRY, COLD	RCP45	-4.9	2.5	inmcm4_r1i1p1	-4.62	2.11
DRY, WARM	RCP45	-4.9	4.3	IPSL-CM5A-LR_r3i1p1	-6.33	4.31
WET, COLD	RCP45	13.3	2.5	bcc-csm1-1_r1i1p1	12.33	2.62
WET, WARM	RCP45	13.3	4.3	CanESM2_r4i1p1	13.18	4.36
DRY, COLD	RCP85	-8.9	4.7	MPI-ESM-LR_r1i1p1	-7.91	5.95
DRY, WARM	RCP85	-8.9	7.6	IPSL-CM5A-LR_r3i1p1	-10.18	7.95
WET, COLD	RCP85	30.9	4.7	CSIRO-Mk3-6-0_r1i1p1	29.80	5.60
WET, WARM	RCP85	30.9	7.6	MIROC5_r3i1p1	31.04	6.6

3.2 Advanced Delta Change method

To account for scale discrepancy between the reference climate dataset used in this project (operating at 1 km spatial scale) and the GCM runs (operating between 1.0° and 3.75°, depending on the model and latitudinal or longitudinal resolution), a proper downscaling technique has to be applied to the GCM runs. We use the well-established Advanced Delta Change (ADC) method [van Pelt et al., 2012a; Kraaijenbrink, 2013a]. This section summarizes the theory of the ADC method and how it was implemented for the application in the Upper Indus basin.

3.2.1 Description of the Advanced Delta Change method

The delta change method is a transformation that scales historical precipitation time series to obtain series that are representative for a future climate. Usually historical time series are used for the transformation. The coefficients required in the transformation are obtained from the GCM climate change signal. For precipitation this signal is essentially the relative difference in precipitation between a control period of the GCM, i.e. the same period as the historical time series, and a future period. As the historical data and GCM data is usually present on very different spatial scales, a linkage between the two scales is required. This is performed by the use of a common grid to which the observation data is aggregated and the GCM data is interpolated.

The classic delta change method comprises a linear transformation of mean precipitation values, which may result in an unrealistic change of the precipitation distribution compared to the changes that occur in the GCMs. However, detailed insight in the change of the extremes in the precipitation distribution is valuable for research and modelling, as many environmental processes trigger only at extreme low or high precipitation amounts, e.g. flooding, erosion and vegetation stress. To accommodate this, a revised version of the delta change method was developed by Van Pelt [van Pelt et al., 2012b], which is called the advanced delta change (ADC) method. This revised method focuses primarily on increasing detail in the high end of the distribution as it is aimed at aiding hydrological modelling of extreme discharge events. The principal difference with the original delta change method is that the revised method uses a non-linear transformation based on the 60% and 90% quantiles of the precipitation distribution



(Figure 16). Furthermore, biases in these quantiles in the control period of the GCM compared with the observation series are corrected for.

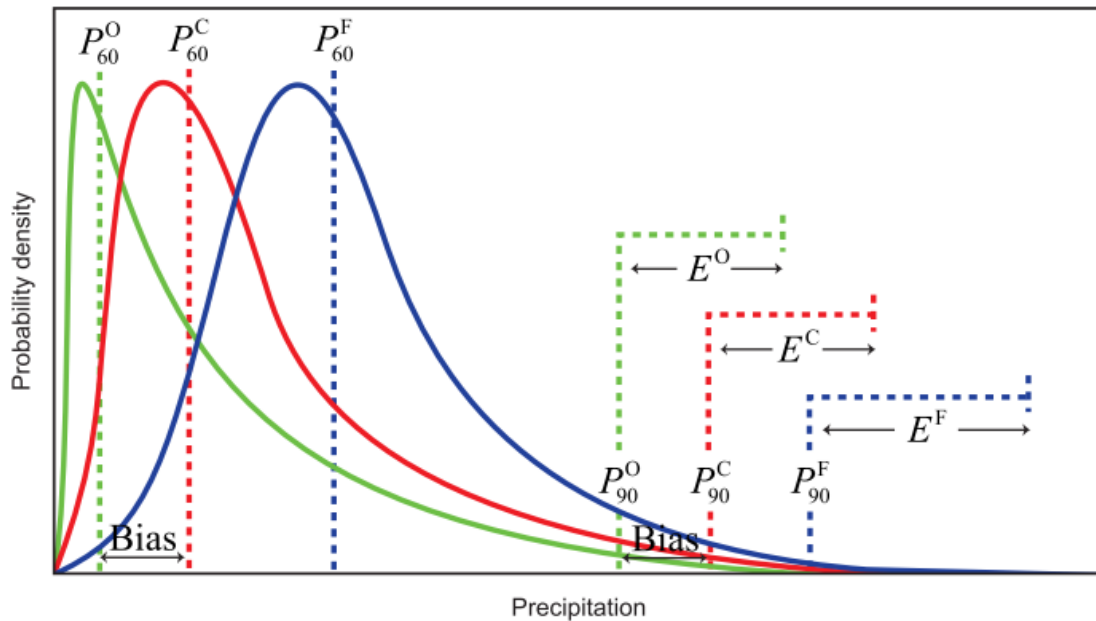


Figure 16: Schematic probability distribution of observation, control and future precipitation with the quantiles, excesses and biases denoted (from [Kraaijenbrink, 2013b], after [van Pelt et al., 2012b]).

[van Pelt et al., 2012] showed that using a non-linear transformation is a feasible method to yield small scale daily data that incorporates the relative change of the precipitation distribution, which could be used for modelling the effects of climate change on hydrological extremes.

Both the GCM datasets and the historical dataset (Chapter 2) must be on the same spatial scale and therefore an aggregation of the daily observation values from the improved forcing data to the common grid is performed using an area-weighted mean. In the case of the Upper Indus basin a common grid at 0.25° spatial resolution is defined. The daily GCM data, both the control and future period, are interpolated to the same grid by bilinear interpolation.

The ADC method does not act on the daily values itself, but rather on 5-day precipitation sums. This is performed as extreme discharge events depend on multiple days of extreme precipitation. In practice, the use of 5-day sums results in 73 non-overlapping sums in a 365-day year. Leap days are excluded. A specific month is assigned to each five day sum, not entirely analogous to Gregorian calendar months. Namely, the months January up to November are each assigned to consecutive groups of six 5-day sums while December is assigned to the remaining group of seven 5-day sums. Figure 17 and Figure 18 present flowcharts that denote all steps of the ADC method that are explained in this section as well as the different temporal scales involved in each step. All calculations for the ADC method are performed using R-scripts and Python-scripts.

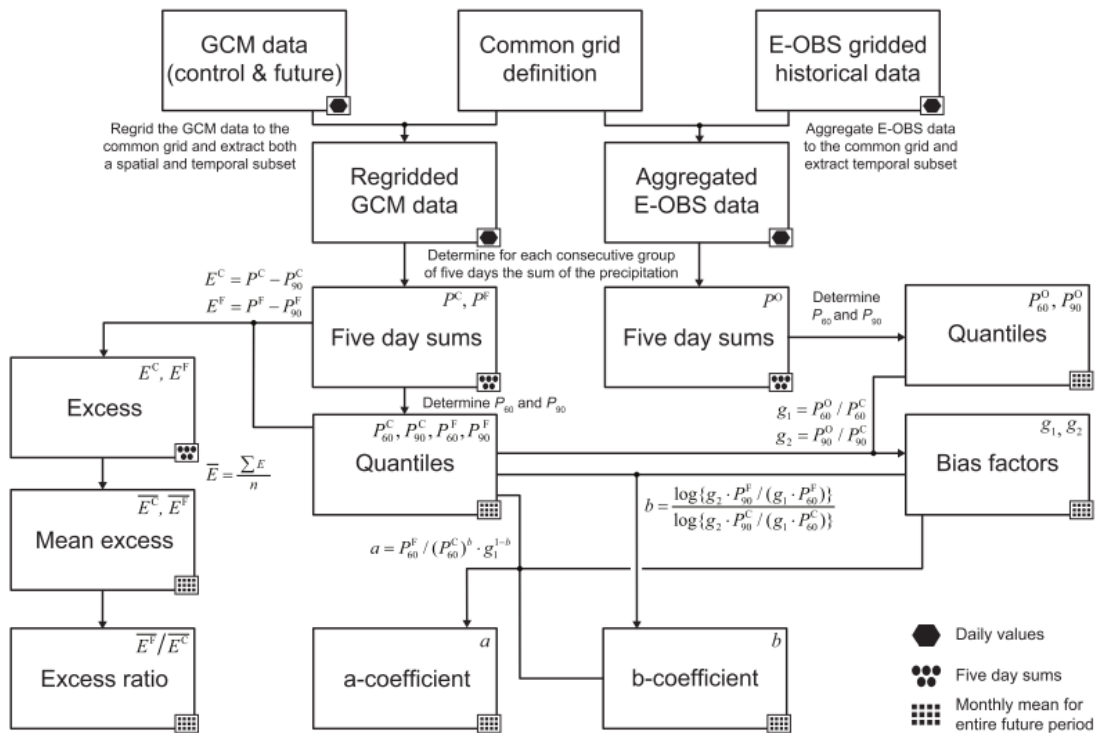


Figure 17: Flowchart of the parameter calculation steps of the advanced delta change method [Kraaijenbrink, 2013b].

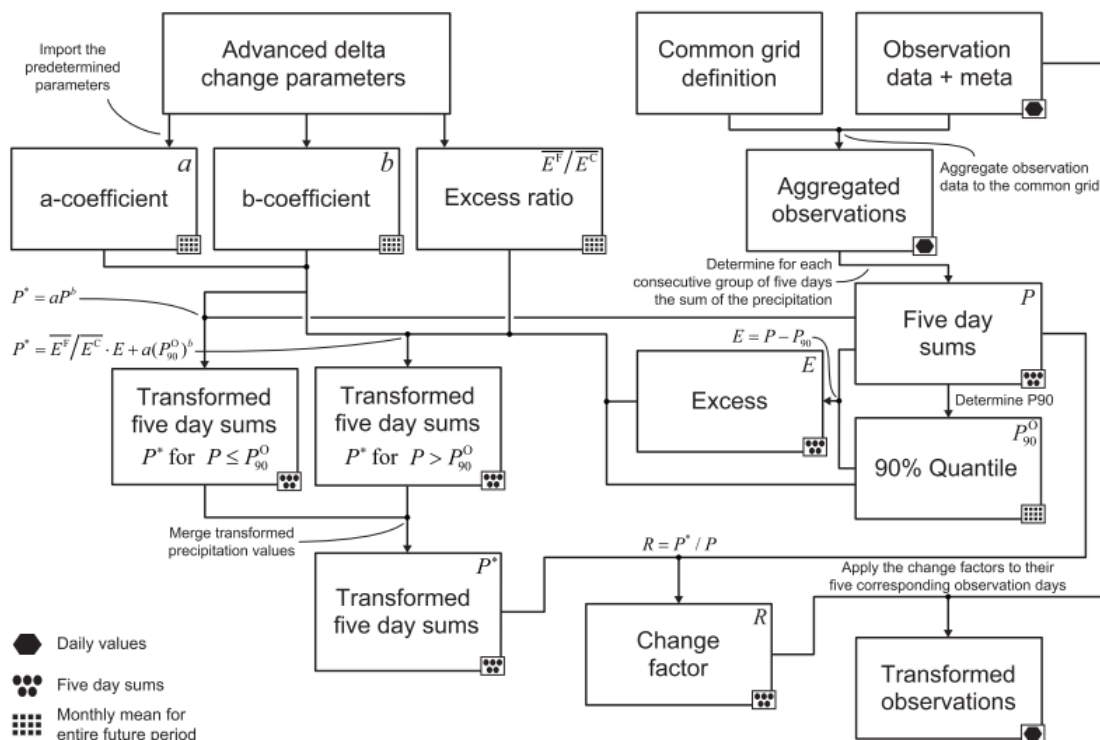


Figure 18: Flowchart of the transformation of the corrected observation time series by applying the coefficients [Kraaijenbrink, 2013b].



For the transformation of the observed 5-day precipitation sums (P) two different equations are used, i.e. for precipitation sums that are smaller or larger than their 90% quantile (P_{90}). This quantile is determined per calendar month and per common grid cell over the entire reference period; hence there are twelve different P_{90} values per grid cell.

The two transformation equations are:

$$P^* = aP^b \text{ for } P^O < P_{90}^O$$

$$P^* = \overline{E^F} / \overline{E^C} \cdot (P^O - P_{90}^O) + a(P_{90}^O)^b \text{ for } P^O > P_{90}^O$$

Where P^* represents the transformed 5-day sums, P the observation 5-day sums, P_{90} the 90% quantile and a and b are the transformation coefficients. The superscripts ^O, ^C and ^F denote whether the variable represents respectively the observation time series, the GCM control series or the GCM future series. For 5-day precipitation sums that exceed the P_{90} of their month an excess value (E) is determined, which is the part of the precipitation that is above P_{90} (Figure 16). It is calculated by:

$$E = P - P_{90}$$

The mean future and control excesses in Equation 2 are, similarly to P_{90} , determined on a monthly basis per grid cell over the entire period by:

$$\overline{E^C} = \frac{\sum P^C - P_{90}^C}{n^C} \quad \text{and} \quad \overline{E^F} = \frac{\sum P^F - P_{90}^F}{n^F}$$

The linear scaling of the transformed precipitation with the ratio of future and control excess in Equation 2 expresses a change in the slope of the extreme value plot of the 5-day maximum precipitation amounts [van Pelt et al., 2012b]. It also avoids unrealistically high transformed precipitation values that may occur when Equation 1 is used for $P > P_{90}$ and $b > 1$.

The transformation coefficients a and b are derived from the 60% and 90% quantiles by:

$$b = \frac{\log\{g_2 \cdot P_{90}^F / (g_1 \cdot P_{60}^F)\}}{\log\{g_2 \cdot P_{90}^C / (g_1 \cdot P_{60}^C)\}}$$

$$a = P_{60}^F / (P_{60}^C)^b \cdot g_1^{1-b}$$

The calculation of the transformation coefficients requires bias correction factors g_1 and g_2 that address systematic differences between the P_{60} and P_{90} of the observations and the GCM control series (Figure 16) to ensure a proper reproduction of the relative changes in these quantiles during the transformation. The correction factors are determined by:

$$g_1 = P_{60}^O / P_{60}^C$$

$$g_2 = P_{90}^O / P_{90}^C$$

To reduce sampling variability in the transformation coefficients, the P_{60} and P_{90} are smoothed temporally by using a weighted mean with weights of 0.25, 0.5 and 0.25 on respectively the previous, current and next month. The mean excesses are smoothed temporally in a similar



manner. There is also noise present in the parameters spatially [van Pelt et al., 2012b]. This is especially an issue for the b coefficient that has a relatively large influence in the transformation and could cause considerable and unrealistically large differences in transformation results of neighboring common grid cells. Therefore spatial smoothing is applied. The ratio between the control and future mean excesses used in Equation 2 is smoothed spatially as well.

When the 5-day precipitation sums are transformed a change factor can be determined for each sum that is subsequently applied to its corresponding five days of daily observations. The individual days within the five day groups are thereby transformed with an equal change factor. This change factor (R) is determined by:

$$R = P^*/P$$

For hydrological modelling purposes transformed temperature data is required besides the transformed precipitation data. To accommodate in this need, the corrected temperature data are transformed to represent future temperatures. The temperature transformation, conversely to that of precipitation, is linear in nature and has the form [van Pelt et al., 2012b]:

$$T^* = \frac{\sigma^F}{\sigma^C} (T - \overline{T^O}) + \overline{T^O} + \overline{T^F} - \overline{T^C}$$

where T^* represents the transformed temperature; T the observed temperature; $\overline{T^O}$, $\overline{T^C}$ and $\overline{T^F}$ the monthly mean of respectively the observed, control and future temperature; σ^C and σ^F the standard deviations of the daily control and future temperature calculated per calendar month.

The means and standard deviations are, similarly as for the precipitation transformation, determined for each common grid cell by aggregation of the observations and bilinear interpolation of the GCM temperatures. Furthermore, similar temporal smoothing is applied to the standard deviations. The transformation however operates on daily values and as a result the transformation does not require the use of a change factor, i.e. the transformation is applied directly to daily values on 1 km grid cell scale (T) by using the common grid scale means ($\overline{T^O}$, $\overline{T^C}$ and $\overline{T^F}$) and standard deviations (σ^C and σ^F).

3.2.2 Implementing the Advanced Delta Change method for the Upper Indus basin

The ADC method is applied to generate transient mapseries of daily precipitation (P), mean air temperature (T_{avg}), maximum air temperature (T_{max}) and minimum air temperature (T_{min}) until the end of the 21st century, for each of the four ensemble members and for each of the two RCPs. Thus in total, 4 GCMs x 2 RCPs = 8 mapseries are generated for each of the four meteorological variables (P , T_{avg} , T_{max} , T_{min}). As reference period we define 1 January 1971 until 31 December 2000. As future period we define 1 January 2001 until 31 December 2100. For the reference period we use the corrected daily meteorological forcing dataset for 1971-2000, which is described in chapter 2. This dataset at 1 km spatial resolution is aggregated to the common grid resolution (0.25°), for use in the application of the ADC method.

For the future period, we select a random year from the 30-year reference period and use that as a basis for the future. We keep this generated sequence of random years between from 2001 until 2100 constant for each of the eight future runs (Table 7).



Table 7: List of years from reference period used as basis for future period (2001-2100).

Future Year	Reference Year								
2001	1994	2021	1976	2041	1975	2061	1995	2081	1980
2002	1997	2022	1996	2042	1980	2062	1979	2082	1971
2003	1972	2023	1973	2043	1980	2063	1975	2083	1998
2004	1974	2024	1979	2044	1997	2064	1980	2084	1990
2005	1995	2025	1974	2045	2000	2065	1975	2085	1977
2006	1971	2026	1974	2046	1995	2066	1977	2086	2000
2007	1980	2027	1981	2047	1992	2067	1980	2087	1982
2008	1998	2028	1974	2048	1981	2068	1986	2088	1975
2009	1997	2029	1989	2049	1999	2069	1995	2089	1996
2010	1971	2030	1995	2050	1984	2070	1989	2090	1994
2011	1988	2031	1988	2051	1989	2071	1995	2091	1995
2012	1987	2032	1971	2052	1971	2072	1985	2092	1997
2013	1973	2033	1972	2053	1986	2073	1972	2093	1982
2014	1986	2034	1989	2054	1984	2074	1979	2094	1987
2015	1971	2035	1998	2055	1995	2075	1977	2095	2000
2016	1999	2036	1987	2056	1997	2076	1973	2096	1993
2017	1978	2037	1999	2057	1987	2077	1982	2097	2000
2018	1995	2038	1982	2058	1973	2078	1971	2098	1971
2019	1981	2039	1990	2059	1994	2079	1992	2099	1997
2020	1981	2040	1978	2060	1997	2080	1999	2100	1983

For all years in the future, the years are randomly sampled with replacement from the 30 years of reference. For each block of 10 years in the future period, the ADC transformation coefficients are determined by comparing two blocks of 30 years. For example, for 2001-2010 the transformation coefficients are determined using the 1971-2000 reference data and the 1991-2020 GCM data in the workflow described in section 3.2.2. The block 2001-2010 is in the middle of the block 1991-2020. After determining the transformation parameters for this 10-year block, the transformation is applied to the climatological data from the corresponding years from the reference period (Table 7), and 10 years of transformed future forcing data are generated. Similar, for the next block of ten years (2011-2020), the transformation coefficients are determined by comparing the 1971-2000 reference data and the 2001-2030 GCM data. The GCM projections are available until 2100, thus for the last 10-year block (2091-2100), the same 30 year block of GCM data (2071-2100) is used to determine the transformation parameters, because the 30-year block 2081-2110 is not available.

Because the variability in precipitation within a common grid cell in the UIB is much larger than in the Rhine basin, for which the ADC-method was originally developed, the *a* and *b* parameters are additionally constrained to avoid unrealistic high transformed daily precipitation values. This is done by constraining the *a* parameter and associated *b* parameter:

$$\text{for } b < 0.55, a = 6 \text{ and } b = 0.55$$

This constraining is based on the distribution of *a* and *b* parameter values observed in the transformation in the Rhine basin [Kraaijenbrink, 2013a]. Additionally the transformed



precipitation values are scaled for each future ten year period at the grid cell level at monthly scale to the ratio of future and reference precipitation sum according to the raw GCM data:

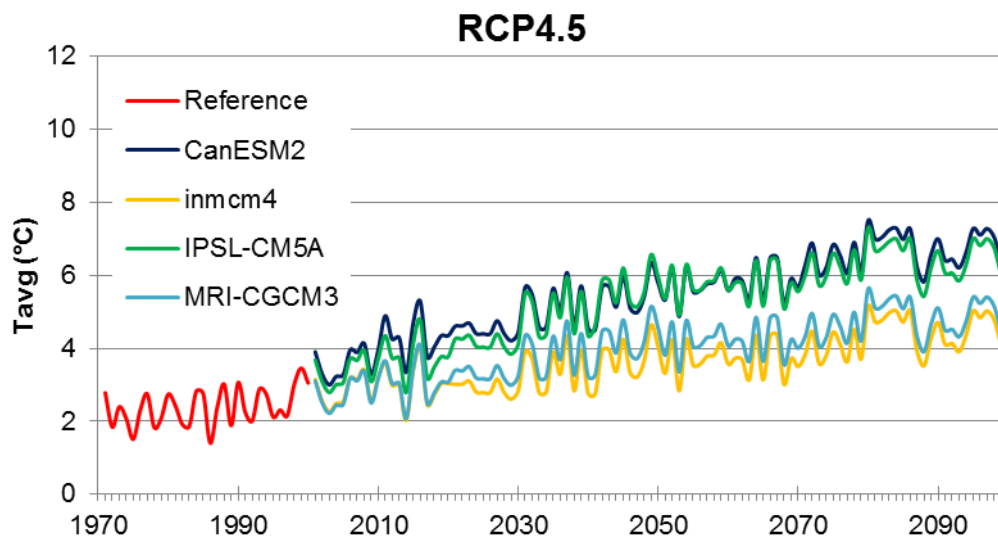
$$[P^{**}]_{day} = [P^*]_{day} \cdot \left[\frac{P_F}{P_C} \cdot \frac{P^O}{P^*} \right]_{month}$$

With P^{**} being the final transformed daily precipitation value, P_F being the future precipitation sum in the GCM future run, P_C being the precipitation sum in the GCM control run, P^O being the precipitation sum in the reference dataset and P^* being the transformed precipitation.

3.3 Changes in Climate

3.3.1 Changes in temperature

Figure 19 shows how mean annual air temperature changes averaged over the entire UIB according to the downscaled climate change scenarios is changing. The figure clearly shows the difference in warming between the two selected RCPs, with RCP8.5 resulting in a much stronger warming at the end of the century compared to RCP4.5. The uncertainty in temperature change indicated by the four different ensemble members is higher for RCP4.5 compared to RCP8.5. For 2071-2100 the difference between the warmest and coldest model is 2.3 K for RCP4.5 whereas it is 2.0 K for RCP8.5 (Table 8).



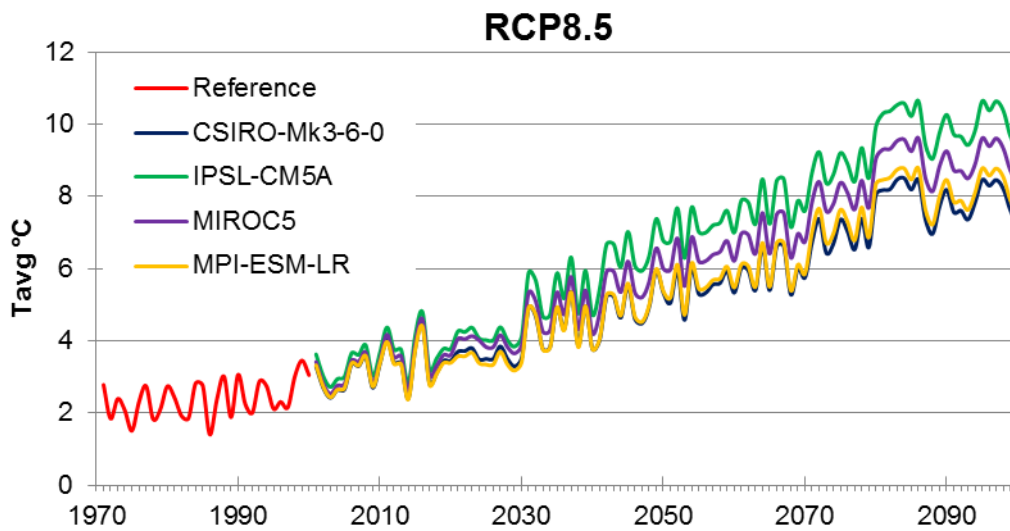


Figure 19: Transient timeseries for entire simulation period of downscaled average annual temperature averaged over the UIB. Upper panel shows RCP4.5 GCMs and lower panel shows RCP8.5 GCMs.

Table 8: UIB-averaged projected temperature changes according to the downscaled GCMs. The delta values for the two time slices are with respect to the reference period (1971-2000).

RCP	Model	ΔT (°C) 2031-2060	ΔT (°C) 2071-2100
RCP4.5	inmcm4_r1i1p1	1.2	2.0
	IPSL-CM5A-LR_r3i1p1	3.1	4.0
	MRI-CGCM3_r1i1p1	1.7	2.4
	CanESM2_r4i1p1	3.1	4.3
RCP8.5	MPI-ESM-LR_r1i1p1	2.7	5.5
	IPSL-CM5A-LR_r3i1p1	3.9	7.3
	CSIRO-Mk3-6-0_r1i1p1	2.6	5.3
	MIROC5_r3i1p1	3.3	6.4

For the complete multi-model ensemble the warming between 2071-2100 and 1971-2000 the projections range from a 2.0 K increase to 7.3 K. As expected, for 2031-2060 the range in projected changes is still smaller, ranging from 1.2 K increase to 3.9 K.

However, these projections averaged over the entire UIB don't reflect the large spatial variation in the projections. These spatial variations are indicated in Figure 20. For both RCPs, the ensemble mean projects stronger increases in temperature in the most mountainous parts of the UIB compared to the lowest areas. The difference can be up to two degrees between the area with strongest temperature increase and the area with the least temperature increase. More striking is the spatial pattern observed in the uncertainty between ensemble members as indicated by the standard deviation of the ensemble projections (right panels). For RCP4.5 the spatial distribution shows a fairly constant pattern with increasing uncertainty between 2031-2060 and 2071-2100. The RCP8.5 ensemble on the other hand, shows strong spatial variation in the uncertainty. For 2031-2060 especially the most eastern high parts of the UIB have large uncertainty in the projections with up to 1.5 K standard deviation, whereas these values are between 0 and 0.5 K in the lowest areas. For 2071-2100 the pattern is very similar but the differences in uncertainty get even larger.



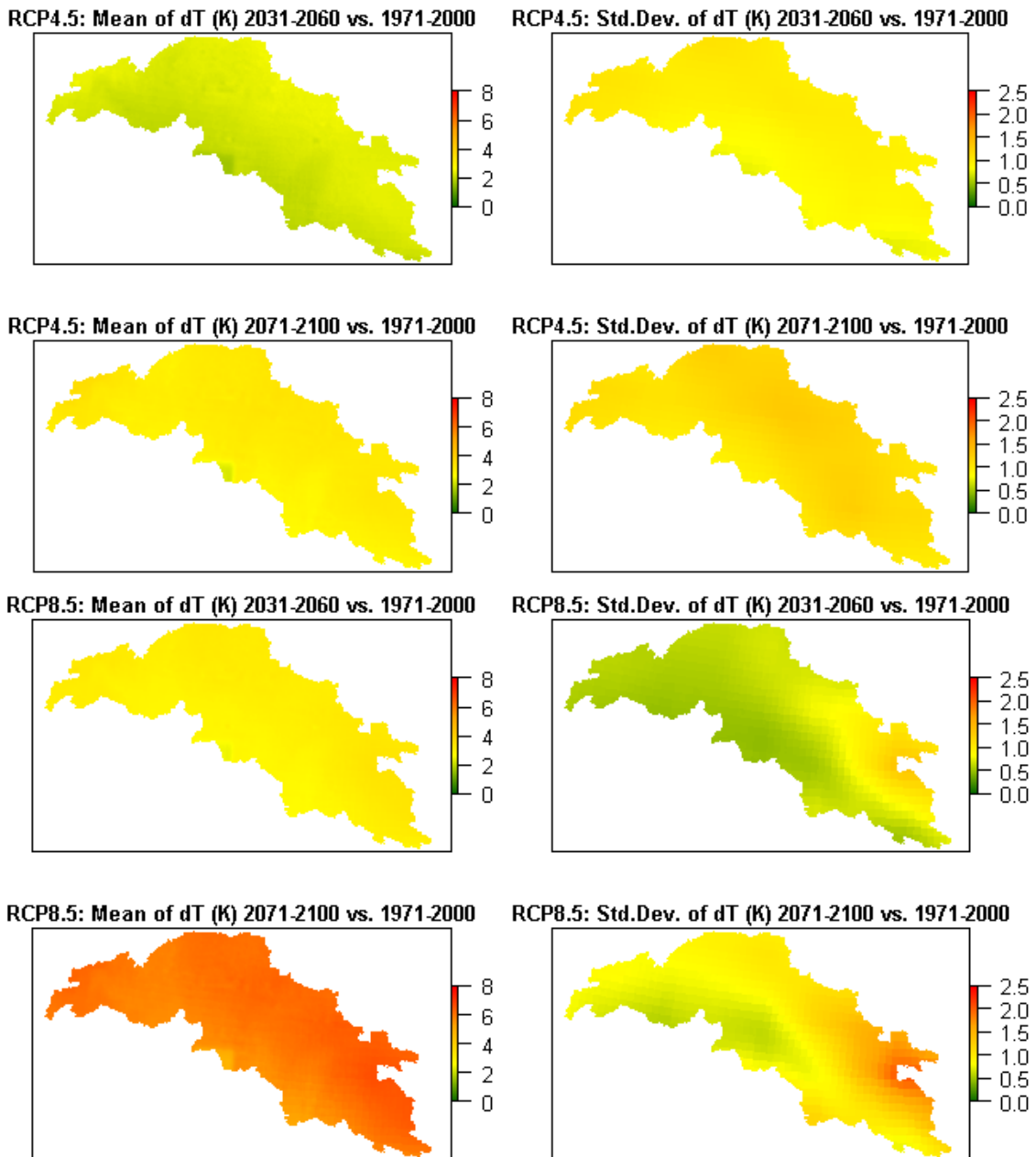


Figure 20: Mean temperature change for time slices 2031-2060 and 2071-2100 with respect to 1971-2000 according to GCM multi-model ensemble (left). The right panels show the standard deviation in temperature change of the entire multi-model ensemble.

Besides large spatial variation the projections also show intra-annual variations (Figure 21). The patterns for both RCPs are quite similar. The ensemble means show strongest temperature increases during the monsoon season. Strong temperature increases are also projected for January during the winter season, which is when a large part of the precipitation in the Hindu Kush and Karakoram falls. Again, a strong emphasis has to put on the uncertainty between the ensemble members as indicated by the error bars. Besides, there may be strong spatial variations within the UIB which are not indicated in this figure. These differences are however captured in the distributed hydrological model forcing and are thus taken into account in calculation of future runoff.



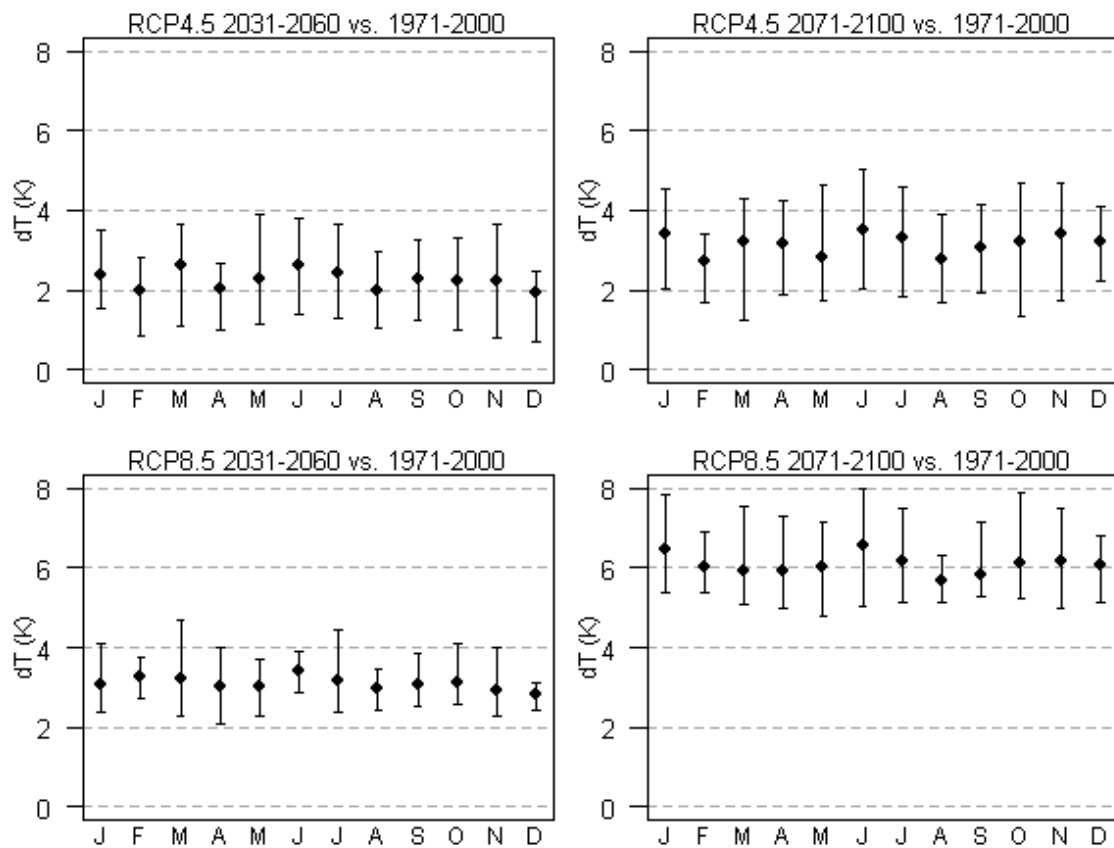


Figure 21: UIB-averaged temperature change per month for 2031-2060 (left) and 2071-2100 (right) vs. 1971-2000. Upper panels are for RCP4.5 multi-model ensemble and lower panels are for RCP8.5 multi-model ensemble. The dots indicate the ensemble mean projection and the whiskers indicate the spread in projections within the entire ensemble.

3.3.2 Changes in precipitation

Projections for precipitation changes in the UIB show much more variation than temperature projections. Table 9 lists the projected changes in precipitation averaged over the UIB for 2031-2060 and 2071-2100 with respect to 1971-2000 according to all downscaled multi-model ensemble members. For RCP4.5 the projected changes at the end of the century vary from 5.4% increase to 8.6% decrease. For RCP8.5 the range is larger: from 15.4% decrease to 34.9% increase. These changes are averaged over the entire UIB and spatial variation is very large, as can be seen in Figure 22.

Table 9: UIB-averaged projected precipitation changes according to the downscaled GCMs. The delta values for the two time slices are with respect to the reference period (1971-2000).

RCP	Model	ΔP (%) 2031-2060	ΔP (%) 2071-2100
RCP4.5	inmcm4_r1i1p1	-7.2	-7.3
	IPSL-CM5A-LR_r3i1p1	-8.1	-8.6
	MRI-CGCM3_r1i1p1	6.8	5.4
	CanESM2_r4i1p1	4.7	-1.1
RCP8.5	MPI-ESM-LR_r1i1p1	-5.5	-12.1
	IPSL-CM5A-LR_r3i1p1	-5.8	-15.4
	CSIRO-Mk3-6-0_r1i1p1	19.6	34.9
	MIROC5_r3i1p1	16.4	26.1

For RCP4.5, the mean of the ensemble projects precipitation increase in the eastern part of the UIB as well as in the northern Karakoram and the most western parts of the Hindu Kush for 2031-2060 with respect to 1971-2000. For the far future, the mean of the ensemble projects precipitation increase in the eastern parts of the UIB and precipitation decrease in the middle and western parts. The spread in projections between the ensemble members is largest in the western parts of the UIB as indicated by the standard deviation in the right panels.

For RCP8.5, mostly increase in precipitation is projected in the middle and eastern parts of the UIB according to the ensemble mean for 2031-2060. For the far future, the spatial variation in projection increases. The mean projection for the Hindu Kush shows decrease whereas strong precipitation increase is projected for the eastern parts of the UIB. In contrast to the temperature projections, the largest uncertainty between the models is observed in the lowest parts of the UIB (lower right panel), whereas the uncertainty is smaller in other parts. Still, it is clear that uncertainty between ensemble members is large everywhere, and strongest for the far future in the RCP8.5 ensemble.



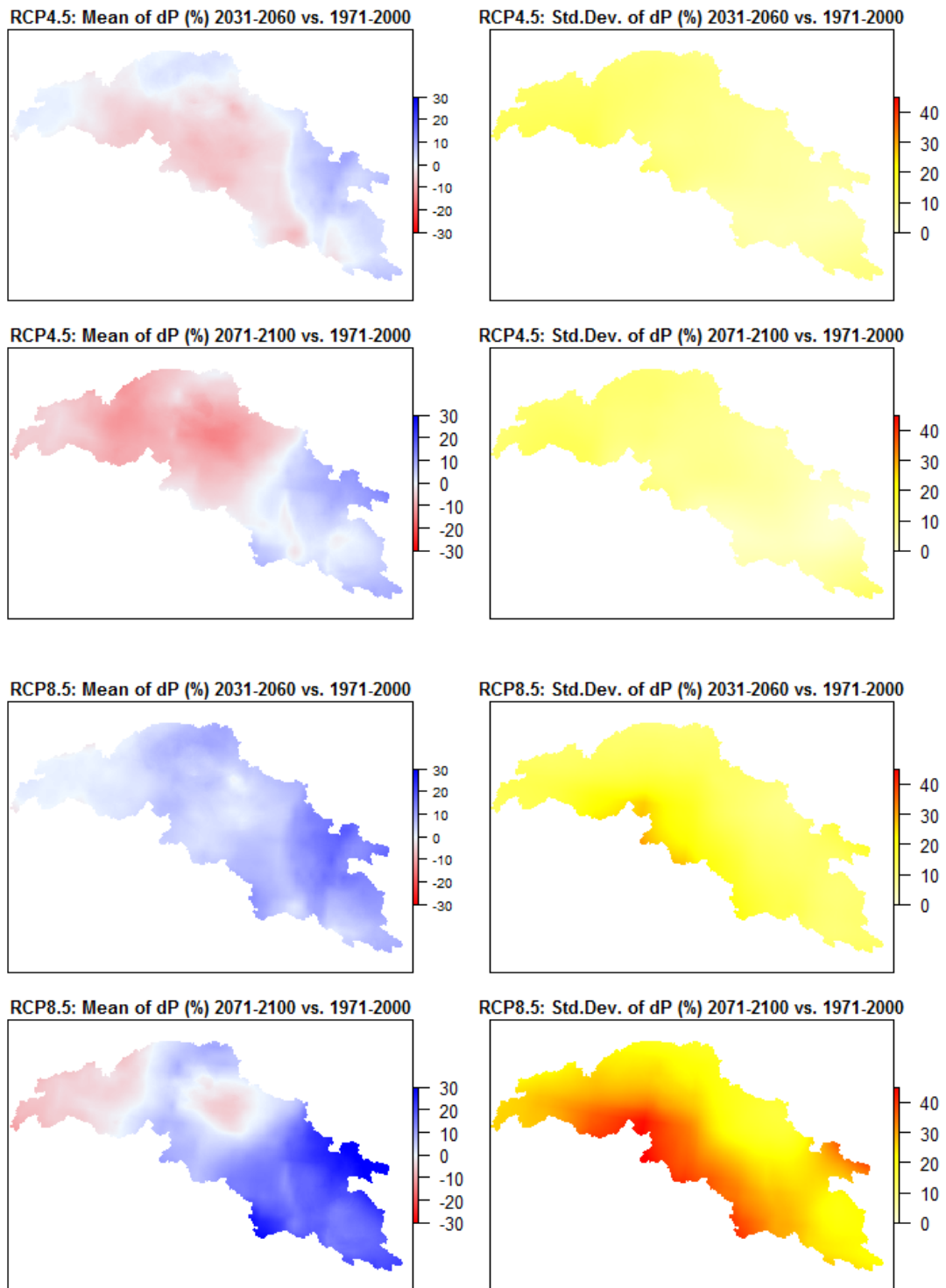


Figure 22: Mean precipitation change for time slices 2031-2060 and 2071-2100 with respect to 1971-2000 according to GCM multi-model ensemble (left). The right panels show the standard deviation in temperature change of the entire multi-model ensemble.

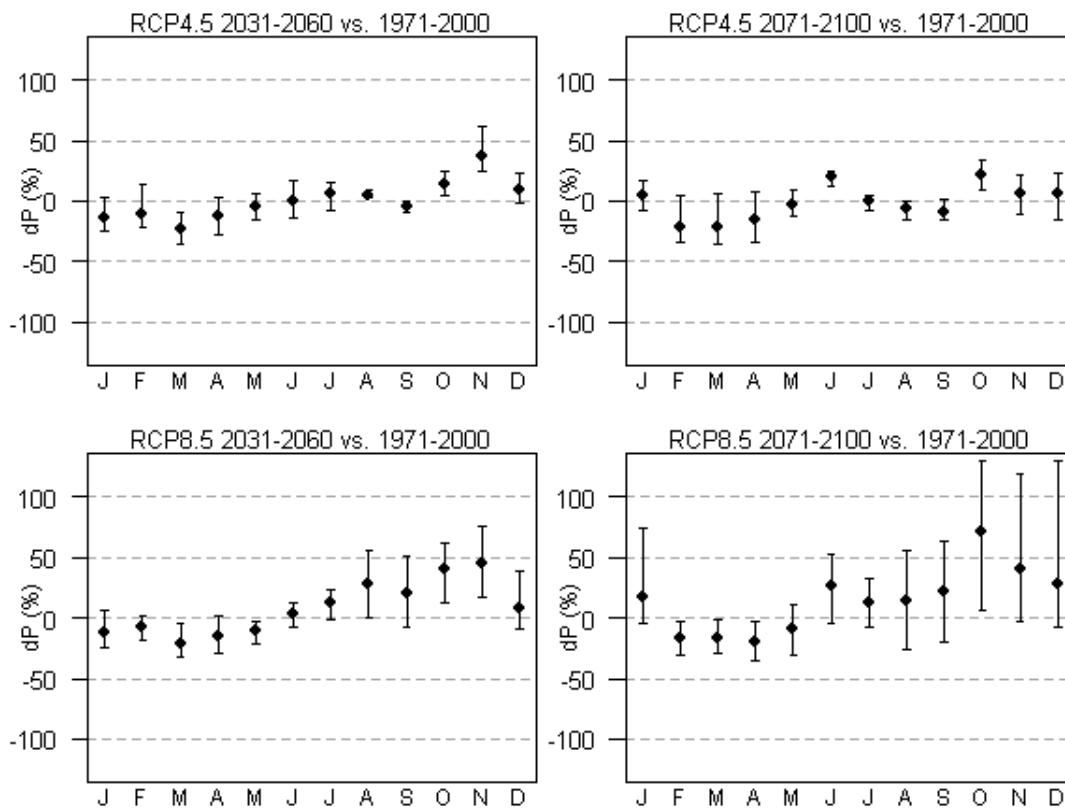


Figure 23: UIB-averaged precipitation change per month for 2031-2060 (left) and 2071-2100 (right) vs. 1971-2000. Upper panels are for RCP4.5 multi-model ensemble and lower panels are for RCP8.5 multi-model ensemble. The dots indicate the ensemble mean projection and the whiskers indicate the spread in projections within the entire ensemble.

On the intra-annual scale, precipitation projections show strong variation (Figure 23). Independent of time slice and RCP, the mean projections indicate decreasing precipitation during February-May, with small uncertainty in between ensemble members. Mostly increases in precipitation are projected for the monsoon season. Stronger precipitation increases are however projected for October to December. Contrasting projections are observed for January between the near future (decrease for RCP4.5 and RCP8.5) and the far future (increase in both RCPs). Note the very large uncertainty for the RCP8.5 ensemble for 2071-2100.

These large variations in space and time for the precipitation projections are taken into account in the forcing data for the distributed hydrological model.

Table 10 summarizes the temperature and precipitation projections for all multi-model ensemble members for the two seasons with most importance for the glacio-hydrology in the UIB: the monsoon season (June-September) and the winter season (December-February). Note that these projections can be very contrasting. For example, the CSIRO model in RCP8.5 for 2031-2060 projects 37.2% precipitation increase during the monsoon season, while only 9.6% increase is projected for the winter season. For the same model, in 2071-2100 very strong increase in precipitation is projected for both seasons (42.1% and 52.3% increase for monsoon season and winter season respectively). Note that these values are averaged over the entire UIB and strong spatial variations are present as demonstrated in Figure 22.



Table 10: UIB-averaged projections of temperature and precipitation change for the monsoon season and winter season with respect to the reference period (1971-2000).

Season	RCP	model	2031-2060		2071-2100	
			ΔT (K)	ΔP (%)	ΔT (K)	ΔP (%)
Monsoon (JJAS)	RCP4.5	inmcm4_r1i1p1	1.5	-4.6	2.4	-2.7
		IPSL-CM5A-LR_r3i1p1	3.2	3.0	4.1	2.3
		MRI-CGCM3_r1i1p1	1.3	2.2	1.9	-5.8
		CanESM2_r4i1p1	3.2	10.5	4.3	3.4
	RCP8.5	MPI-ESM-LR_r1i1p1	2.6	-1.8	5.4	-9.5
		IPSL-CM5A-LR_r3i1p1	3.9	6.8	7.1	-14.3
		CSIRO-Mk3-6-0_r1i1p1	2.7	37.2	5.4	42.1
		MIROC5_r3i1p1	3.3	28.9	6.2	47.7
Winter (DJF)	RCP4.5	inmcm4_r1i1p1	1.1	-10.0	2.0	-7.7
		IPSL-CM5A-LR_r3i1p1	2.9	-18.3	3.8	-18.2
		MRI-CGCM3_r1i1p1	1.9	9.0	2.7	8.8
		CanESM2_r4i1p1	2.5	-11.7	3.9	-7.4
	RCP8.5	MPI-ESM-LR_r1i1p1	2.7	-12.3	5.7	-16.5
		IPSL-CM5A-LR_r3i1p1	3.5	-18.2	7.0	-13.0
		CSIRO-Mk3-6-0_r1i1p1	2.6	9.6	5.3	52.3
		MIROC5_r3i1p1	3.3	-4.5	6.8	-5.6

3.3.3 Changes in precipitation extremes

The greatest advantage of using the Advanced Delta Change method over a simple linear delta change method is that the Advanced Delta Change method projects changes in the distribution of the precipitation intensity. Table 11 lists how this distribution changes in the future for each of the ensemble members for the near future and far future for five subbasins in the UIB (Figure 37). From the table it is clear that for each model in each subbasin the P_{99} increases, thus also for models projecting decreases in the total precipitation. In each subbasin, most models project decreases in P_{60} , except for the wettest models in RCP8.5 (MIROC and CSIRO), which project increases for all precipitation quantiles. The mostly observed decrease in the low precipitation quantiles accompanied by increase in the high precipitation quantiles leads to the general conclusion that a shift towards more extreme precipitation events can be expected in the UIB.

Table 11: Quantiles of daily precipitation averaged over five subbasins in the UIB for the reference period, near future and far future, for all ensemble members in RCP4.5 and RCP8.5

Basin	Period	RCP	Model	P_{50} (mm day ⁻¹)	P_{60} (mm day ⁻¹)	P_{90} (mm day ⁻¹)	P_{95} (mm day ⁻¹)	P_{99} (mm day ⁻¹)
Hunza - Dainyor bridge	1971-2000	-	Reference	0.015	0.206	4.97	9.6	25.3
	2031-2060	RCP4.5	CanESM2_rcp45	0.005	0.136	4.24	8.9	31.4
			IPSL_CM5A_LR_rcp45	0.004	0.117	3.76	8.0	29.7
			inmcm4_rcp45	0.004	0.119	3.69	8.0	30.5
			MRI_CGCM3_rcp45	0.006	0.154	4.66	9.9	33.7
			CSIRO_Mk3_6_0_rcp85	0.006	0.157	4.87	10.4	33.8
		RCP8.5	IPSL_CM5A_LR_rcp85	0.004	0.106	3.60	7.7	29.8
			MIROC5_rcp85	0.006	0.155	4.91	10.5	32.9
			MPI_ESM_LR_rcp85	0.004	0.119	3.89	8.7	33.3



Indus - Skardu	2071-2100	RCP4.5	CanESM2_rcp45	0.004	0.117	3.89	7.9	29.4	
			IPSL_CM5A_LR_rcp45	0.003	0.101	3.56	7.6	29.5	
			inmcm4_rcp45	0.003	0.098	3.33	7.1	29.7	
			MRI_CGCM3_rcp45	0.004	0.133	4.44	9.3	33.6	
		RCP8.5	CSIRO_Mk3_6_0_rcp85	0.006	0.173	5.58	11.2	37.7	
			IPSL_CM5A_LR_rcp85	0.002	0.068	2.66	6.2	27.7	
			MIROC5_rcp85	0.004	0.136	4.79	9.8	35.8	
			MPI_ESM_LR_rcp85	0.003	0.093	3.43	7.7	35.5	
	1971-2000	-	Reference	0.355	0.716	4.58	7.6	16.5	
		2031-2060	RCP4.5	CanESM2_rcp45	0.323	0.668	4.48	7.9	21.2
	IPSL_CM5A_LR_rcp45			0.277	0.573	4.04	7.3	19.4	
	inmcm4_rcp45			0.265	0.542	3.84	7.1	19.1	
	MRI_CGCM3_rcp45			0.324	0.640	4.41	8.2	21.8	
	RCP8.5		CSIRO_Mk3_6_0_rcp85	0.370	0.771	5.01	8.7	22.1	
IPSL_CM5A_LR_rcp85			0.251	0.515	3.97	7.5	21.4		
MIROC5_rcp85			0.350	0.736	5.30	9.0	22.9		
MPI_ESM_LR_rcp85			0.285	0.585	4.13	7.7	20.4		
2071-2100	RCP4.5	CanESM2_rcp45	0.335	0.684	4.35	7.7	20.5		
		IPSL_CM5A_LR_rcp45	0.271	0.564	3.93	7.3	20.0		
		inmcm4_rcp45	0.293	0.600	4.00	7.2	18.9		
		MRI_CGCM3_rcp45	0.338	0.658	4.33	8.0	21.1		
		RCP8.5	CSIRO_Mk3_6_0_rcp85	0.468	0.937	5.42	9.5	23.7	
			IPSL_CM5A_LR_rcp85	0.220	0.467	3.73	7.1	20.8	
			MIROC5_rcp85	0.400	0.830	5.79	10.3	25.2	
			MPI_ESM_LR_rcp85	0.285	0.583	3.89	7.5	20.5	
	Indus - Tarbela	1971-2000	-	Reference	0.488	0.881	4.93	8.1	17.2
			2031-2060	RCP4.5	CanESM2_rcp45	0.440	0.816	4.80	8.5
		IPSL_CM5A_LR_rcp45			0.363	0.685	4.37	7.8	19.3
		inmcm4_rcp45			0.358	0.670	4.28	7.7	19.7
		MRI_CGCM3_rcp45			0.440	0.827	4.93	9.0	21.9
		RCP8.5		CSIRO_Mk3_6_0_rcp85	0.490	0.917	5.46	9.5	23.3
IPSL_CM5A_LR_rcp85				0.328	0.624	4.35	8.0	21.0	
MIROC5_rcp85				0.460	0.896	5.67	9.7	22.6	
MPI_ESM_LR_rcp85				0.384	0.714	4.51	8.2	20.8	
2071-2100		RCP4.5	CanESM2_rcp45	0.446	0.809	4.48	7.7	20.2	
			IPSL_CM5A_LR_rcp45	0.352	0.651	4.22	7.7	20.2	
			inmcm4_rcp45	0.383	0.692	4.25	7.4	19.3	
			MRI_CGCM3_rcp45	0.456	0.827	4.76	8.3	22.7	
		RCP8.5	CSIRO_Mk3_6_0_rcp85	0.661	1.149	5.96	10.4	25.7	
	IPSL_CM5A_LR_rcp85		0.282	0.534	3.79	7.3	20.9		
	MIROC5_rcp85		0.512	0.985	5.96	10.1	24.8		
	MPI_ESM_LR_rcp85		0.377	0.673	4.15	7.6	21.0		
Kabul - Nowshera	1971-2000	-	Reference	0.309	0.739	6.07	10.6	25.4	
		2031-2060	RCP4.5	CanESM2_rcp45	0.302	0.730	6.23	11.2	28.0
	IPSL_CM5A_LR_rcp45			0.184	0.449	4.70	9.1	25.1	
	inmcm4_rcp45			0.231	0.568	5.33	10.1	27.0	
	MRI_CGCM3_rcp45			0.293	0.731	6.55	11.8	29.4	
	RCP8.5		CSIRO_Mk3_6_0_rcp85	0.289	0.718	7.03	12.2	32.1	
			IPSL_CM5A_LR_rcp85	0.156	0.398	4.51	9.5	27.7	
			MIROC5_rcp85	0.276	0.687	6.40	12.1	30.9	
			MPI_ESM_LR_rcp85	0.229	0.554	5.11	9.2	24.6	
	2071-2100	RCP4.5	CanESM2_rcp45	0.261	0.648	5.28	9.3	26.7	
			IPSL_CM5A_LR_rcp45	0.149	0.395	4.23	8.6	25.4	
			inmcm4_rcp45	0.212	0.529	4.69	9.0	27.9	
			MRI_CGCM3_rcp45	0.281	0.717	6.13	11.0	29.8	
		RCP8.5	CSIRO_Mk3_6_0_rcp85	0.392	0.903	7.47	12.9	36.4	
IPSL_CM5A_LR_rcp85			0.117	0.297	3.32	6.9	25.5		
MIROC5_rcp85			0.237	0.604	5.75	11.3	32.5		
MPI_ESM_LR_rcp85			0.142	0.351	3.66	7.7	25.5		
Satluj	1971-2000	-	Reference	0.749	1.514	10.23	17.3	38.5	
		2031-2060	RCP4.5	CanESM2_rcp45	0.687	1.439	9.77	17.6	45.8
	IPSL_CM5A_LR_rcp45			0.592	1.298	9.24	16.6	43.4	
	inmcm4_rcp45			0.535	1.110	8.34	15.3	41.8	
	MRI_CGCM3_rcp45	0.653		1.350	9.33	16.4	47.2		



2071-2100	RCP8.5	CSIRO_Mk3_6_0_rcp85	0.807	1.636	10.57	19.2	50.1
		IPSL_CM5A_LR_rcp85	0.463	1.048	8.99	17.2	46.1
		MIROC5_rcp85	0.748	1.650	11.45	19.9	48.9
		MPI_ESM_LR_rcp85	0.538	1.149	8.50	15.7	41.3
		CanESM2_rcp45	0.769	1.584	10.70	18.4	46.7
	RCP4.5	IPSL_CM5A_LR_rcp45	0.548	1.206	9.36	16.6	43.6
		inmcm4_rcp45	0.645	1.360	10.11	17.6	44.0
		MRI_CGCM3_rcp45	0.714	1.401	9.76	16.7	46.8
		CSIRO_Mk3_6_0_rcp85	1.154	2.238	12.95	22.4	53.8
	RCP8.5	IPSL_CM5A_LR_rcp85	0.429	0.962	8.89	16.8	49.5
		MIROC5_rcp85	0.937	2.057	13.96	23.6	55.7
		MPI_ESM_LR_rcp85	0.509	1.098	8.72	15.5	42.9



4 Distributed hydrological modelling

4.1 Model description

4.1.1 *Spatial Processes in Hydrology model (SPHY)*

In this project FutureWater's Spatial Processes in Hydrology (SPHY) model is used. The SPHY model is a raster based highly detailed full distributed cryospheric- hydrological model. The model is based on commonly accepted standards from multiple proven hydrological models and the approach is based on [Immerzeel *et al.*, 2010b]. SPHY is created in PCRaster environmental modelling software [Karssenber *et al.*, 2001]. PCRaster is a spatio-temporal environmental modelling language developed at Utrecht University, the Netherlands. The model runs at 1 x 1 km spatial resolution with daily time steps and incorporates all major hydrological processes as well as cryospheric processes.

The actual runoff which is calculated for each grid cell consists of four contributing factors. These are: runoff originating from rain, runoff originating from snow melt, runoff originating from glacial melt, and base flow, as visualized in Figure 24. With the daily air temperature and daily precipitation per grid cell as input the model evaluates how much precipitation falls and it is disaggregated into either snow or rain based on the air temperature distribution. The model evaluates the amount of glacier melt and snow melt or accumulation and which part of snow and glacier melt is directly transformed to runoff and which part refreezes. Rainfall-runoff processes are evaluated in a soil component in the model. The runoff from all contributing components is routed through the system using the DEM.

Each grid cell is divided in fractions. If a cell is (partly) glacierized, the cell has a glacier fraction between 0 and 1 (0: no glacier cover, 1: complete glacier cover). The other fraction of the grid cell can be either 'snow' or 'rain'. This depends on the presence of snow cover, which is determined by the model. As long as snow cover is present, the snow module is active, while the rain module is active when no snow cover is present.



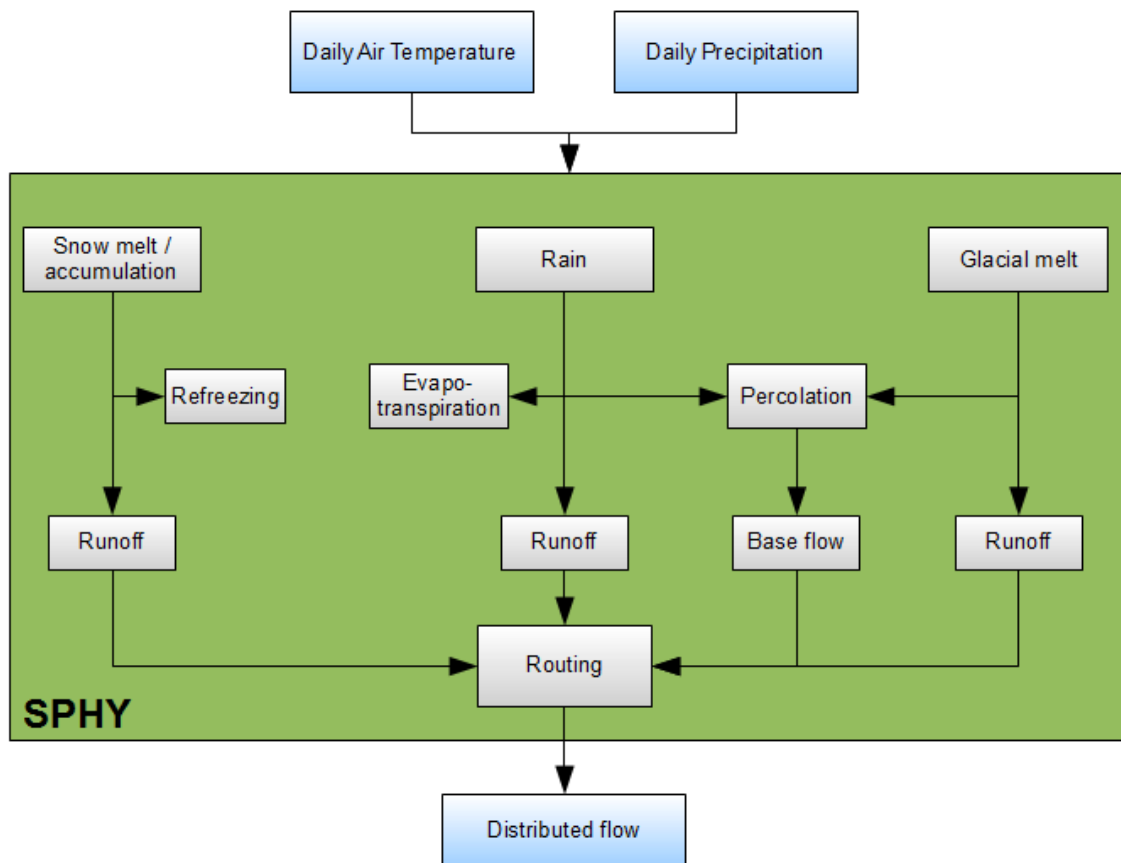


Figure 24: Model structure of SPHY model

4.1.2 Cryospheric processes

The initial glacier cover is derived from the recently completed inventory by ICIMOD [Bajracharya and Shrestha, 2011]. With this dataset the initial glacierised fraction of each grid cell is calculated. Since the model is set up for a 1 x 1 km resolution, the ice cover is described as a fraction varying from 0 (no glacial cover) to 1 (100% glacial cover). In this way, 1 x 1 km grid cells which are partly covered with ice can be simulated. A differentiation is made between clean ice glaciers and debris covered glaciers. Glaciers at lower altitude tend to have more debris cover because of the cumulative accumulation of debris from higher grounds and glacier parts with a small slope have more debris cover compared to steep-sloped parts of the glacier. The differentiation between clean ice glaciers and debris covered glaciers is then re-calculated to fractions of the 1 x 1 km grid cells used in the model. Summing the fractions of clean ice glacier and debris covered glacier will always result in a total fraction of one.

Initial conditions for snow cover are obtained directly from the model. A model run is done simulating several years to develop a balanced snow cover. The snow cover at the end of this model run is used as initial snow cover for further model runs. In the model calculations, the amounts of ice and snow are described as millimeters water equivalent. The modelling of processes involving glaciers is described in a schematic way in Figure 25. Melt from clean ice glaciers is defined as the air temperature (if above 0 °C) multiplied by the degree day factor for clean ice, multiplied by the clean ice fraction of the glacier cover and the cell fraction with glacier cover.



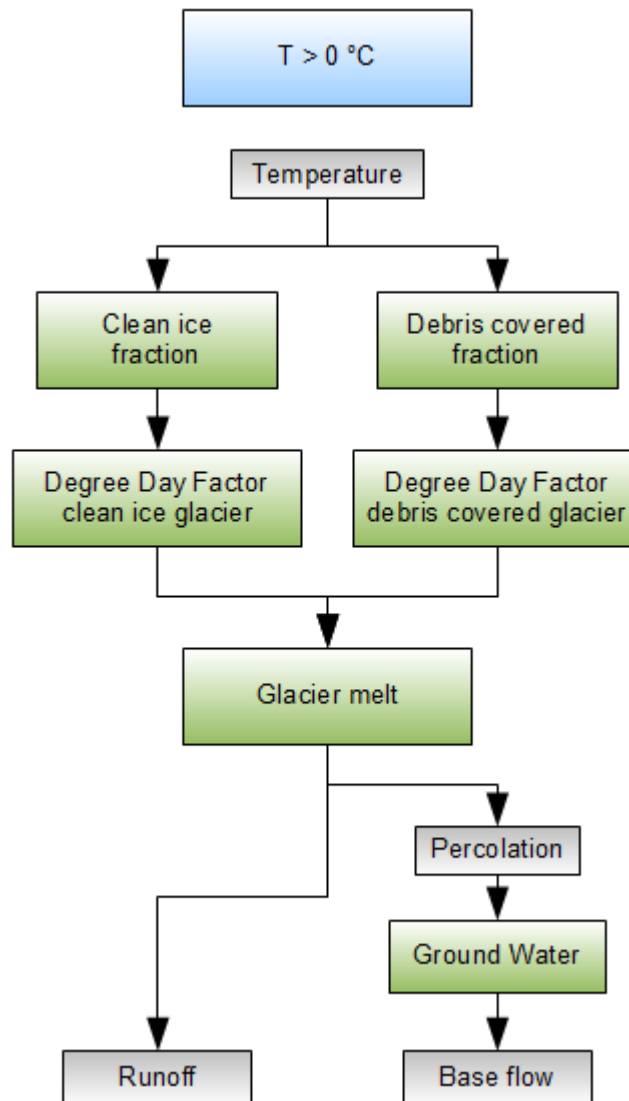


Figure 25: Schematic representation glacier related processes in the HI-SPHY model

For the melt from debris covered glaciers the calculation is similar, although a different degree day factor for debris covered glaciers is specified. Melt rates for debris covered glaciers are lower, since the energy fluxes are partly blocked by the (thick) debris cover.

Degree Day Modeling

The use of temperature index or degree day models is widespread in cryospheric models to estimate ice and snow melt. In these models an empirical relationship between melt and air temperature based on a frequently observed correlation between the two quantities is assumed [Hock, 2005]. Degree-day models are easier to set up compared to energy-balance models, and only require air temperature, which is mostly available and relatively easy to interpolate.

The total glacier melt is then calculated by summing the two components from clean ice glacier melt and debris covered glacier melt. A part of glacial melt comes to runoff, while another part percolates to the ground water. This process is controlled by adjusting the glacial runoff factor.

For each cell the model determines if precipitation falls as snow or rain by comparing the actual air temperature to a critical temperature. When air temperature is below or equal to the critical



temperature, precipitation will fall as snow. When air temperature is above the critical temperature, precipitation will fall as rain.

In the model a differentiation is made between the potential snow melt and the actual snow melt (Figure 26). The potential snow melt is defined as the air temperature (if above 0 °C) multiplied by a degree day factor for snow multiplied by the cell fraction covered with snow. The actual snow melt however, is limited by the thickness of the snow pack. No more snow can be melted than the amount of snow which is available at the considered time step. The snow storage is then updated, to be used for the next time step. The snow storage is updated by subtracting the melt and/or adding the freshly fallen snow or rain to the water storage in the snow pack. The updated snow storage is the 'old' snow storage with the fresh snow added and the actual snow melt subtracted.

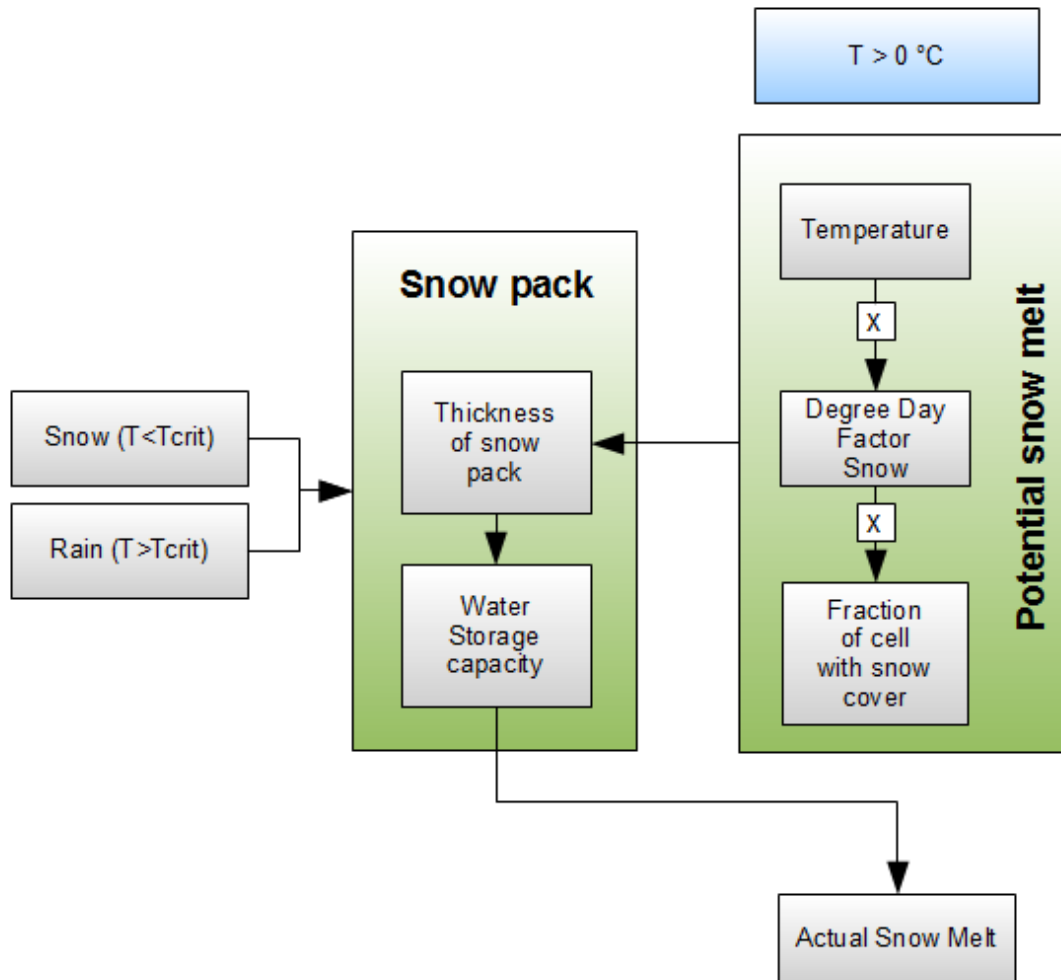


Figure 26 Schematic representation of snow related processes in the HI-SPHY model

The water resulting from snow melt will partially refreeze as it infiltrates the underlying snow pack. The maximum amount of water that can refreeze is defined by the water storage capacity of the snow pack which depends on the thickness of the snow pack present and the storage capacity of snow (e.g. the total millimeters of melt water that can refreeze per millimeter of snow). The actual amount of water that is stored in the snow pack is defined as the water stored in the snow pack during the previous time step summed by the actual snow melt. Snow melt will become actual snow melt when the amount of snow melt exceeds the water storage capacity of the snow pack. When all snow in a grid cell has melted, the snow fraction is set to zero. If snow



falls on a cell which had no snow during the previous time step the snow fraction is updated to 1.

4.1.3 Rainfall runoff

The modelling steps for rainfall in the HI-SPHY model are represented in Figure 27. Precipitation in the model will fall as rain when the air temperature is above a critical temperature.

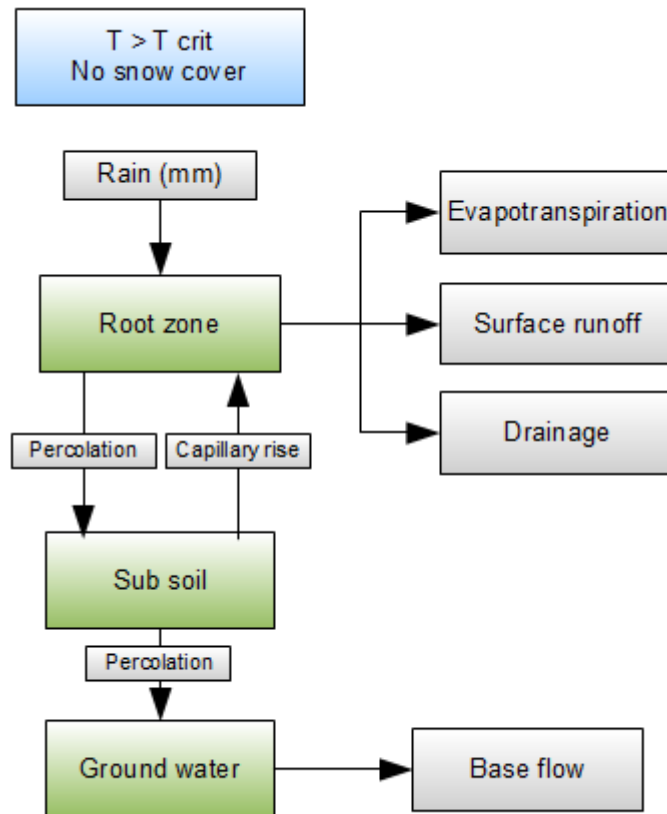


Figure 27: Schematic representation of rainfall-runoff modelling in the HI-SPHY model

A soil module based on the saturation excess overland flow (also known as Hewlettian runoff) concept is incorporated in the HI-SPHY model. The soil layer in the model is divided in a root zone and a sub soil. The thickness of the soil is slope dependent in the model. The soil properties are based on pedotransfer functions, to quantify soil properties for different soil types. The soil properties used in the HI-SPHY model are listed in Table 12. Using these properties, the model evaluates how much water in the rootzone is available for evapotranspiration, surface runoff, lateral drainage and percolation/capillary rise to/from the subsoil.

Table 12: Soil properties used in HI-SPHY model.

Rootzone	Subsoil
Rooting depth (mm)	Subsoil depth (mm)
Saturated water content (mm/mm)	Saturated water content (mm/mm)
Field capacity (mm/mm)	Field capacity (mm/mm)
Wilting point (mm/mm)	Saturated conductivity (mm/day)
Permanent wilting point (mm/mm)	
Saturated conductivity (mm/day)	



The potential evapotranspiration (ET_{pot}) in the model is calculated using the reference evapotranspiration (ET_{ref}) and a crop coefficient (K_c):

$$ET_{pot} = ET_{ref} \cdot K_c$$

The reference evapotranspiration is calculated according to the Modified Hargreaves method [Droogers and Allen, 2002]. This method requires average, maximum and minimum air temperature (T_{avg} , T_{max} , T_{min}), the summed precipitation (P) and incoming extraterrestrial radiation (Ra):

$$ET_{ref} = 0.0013 \cdot 0.408Ra \cdot (T_{avg} + 17.0) \cdot ((T_{max} - T_{min}) - 0.0123P)^{0.76}$$

Based on land use type, each grid cell is assigned a K_c factor to calculate the potential evapotranspiration. The actual evapotranspiration (ET_{act}) is the potential evapotranspiration limited by the water available in the rootzone (e.g. the saturation of the root zone).

Excess water is also leaving the rootzone as surface runoff, lateral drainage or percolation to the sub soil. The occurrence of capillary rise from the sub soil to the root zone or percolation from the root zone to the sub soil depends on differences in water saturation of both soil layers. Water percolates from the sub soil to the ground water.

At the moment a 'rain fraction' is covered with snow, it switches to 'snow fraction'. As long as snow cover is present, the snow module (described in section 4.1.2) is active. However, the soil component remains active, although no more precipitation is entering the soil and no more water is leaving the soil as surface runoff or evapotranspiration. Percolation to the subsoil and eventually to the ground water remains active.

4.1.4 Ground water

A ground water reservoir generating base flow is incorporated in the model. During periods with low runoff the streams are fed by processes such as sustained ground water flow and/or slow throughflow through the deeper soil from earlier precipitation events. This is referred to as base flow. The ground water reservoir is active for each entire grid cell. The ground water is fed by percolation from the sub soil and percolation from the glacier fraction of a cell. These two components provide recharge to the ground water reservoir. The ground water recharge is translated into baseflow released from the reservoir with a certain time lag.

4.1.5 Routing

In the model, the generated runoff is routed through the basin according to a flow direction map based on the DEM. For each cell the local drain direction is defined. The runoff generated per grid cell accumulates with runoff generated in downstream grid cells. Using a linear regression with a regression constant, the time water needs to flow through the reservoir towards the outflow point is simulated.

4.2 Calibration

The SPHY-model is calibrated using a three-step calibration approach, to calibrate three groups of related model parameters separately. Parameters related to the glacier melt component are calibrated separately, as well as parameters related to snow melt. The third group of



parameters that is calibrated separately includes the parameters related to direct rainfall-runoff, baseflow and routing. The two groups of parameters related to glacier melt and snow melt have to be calibrated before the third group of parameters is calibrated.

4.2.1 Calibration of parameters related to glacier melt

The glacier melt parameters include the degree day factors for non-debris covered glaciers (DDF_{CI}) and debris-covered glaciers (DDF_{DC}). These parameters are calibrated by comparing the simulated glacier mass balance between 1999 and 2007 to the observed geodetic mass balance that was derived using DEM-differencing by T. Bolch for the period 1999-2009 in the Shimshal valley area. The simulated mass balance does not extend after 2007 until 2009 because no forcing data is available in APHRODITE [Yatagai *et al.*, 2012b] after 2007 and APHRODITE is used as a basis for the corrected forcing dataset described in chapter 2. The glacier melt component of the SPHY-model is run at 1 km resolution for this area and the glacier mass balance for the individual glaciers that are located in this area according the Randolph Glacier Inventory version 3.2 (RGI, [Arendt *et al.*, 2012]) is calculated. For the same glacier outlines, the observed mass balance is calculated from the elevation differences in the DEMs combined with the average ice density. The ice density varies in the three dimensions of the glaciers, with fresh snow being least dense and the matured ice at the bottom of the thickest parts of the glaciers being most dense. An average ice density from scientific literature is assumed to be representative for the area [Huss, 2013]. The DDFs are optimized as to have the lowest difference in the distribution of observed and simulated mass balances for the glaciers present in the area (Figure 28).

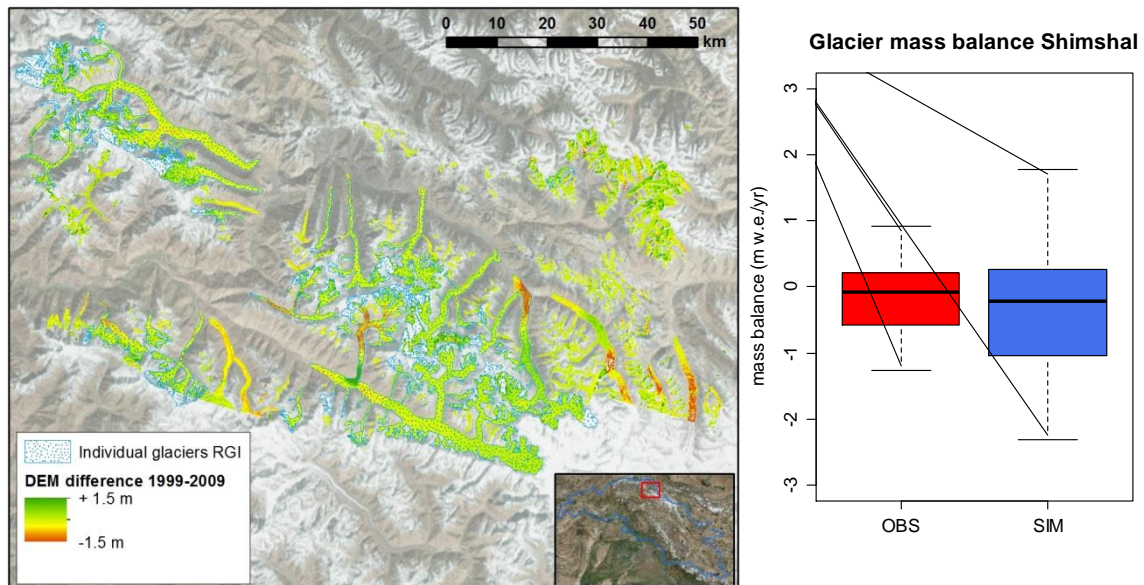


Figure 28: Left: Map showing DEM difference for glaciated areas in Shimshal valley 1999-2009 (provided by T. Bolch), and outlines of individual glaciers from the Randolph Glacier Inventory covering the analysed parts. Right: Box plots showing distributions of observed (1999-2009) and simulated (1999-2007) glacier mass balances for optimum parameter configuration.

The parameter values resulting in the smallest difference between the observed and simulated glacier mass balance are listed in Table 13.



Table 13: Calibrated values for glacier melt related parameters in the SPHY-model.

Parameter name	Symbol	Value
Degree day factor for clean ice glaciers	DDF _{CI}	7.5 mm w.e. day ⁻¹
Degree day factor for debris covered glaciers	DDF _{DC}	4.0 mm w.e. day ⁻¹

4.2.2 Calibration of parameters related to snow melt

The parameters related to snow melt are calibrated independently using MODIS snow cover imagery. The same MODIS dataset is used as in [Immerzeel *et al.*, 2009]. From the beginning of 2000 until halfway 2008 the snow cover imagery is averaged for 46 different periods of 8 days (5 days for the last period) to generate 46 different average snow cover maps. E.g. period 1 is the average snow cover for 1-8 January for 2000 until 2008, period 2 is the average snow cover for 9-16 January for 2000 until 2008, etc.

The routines related to snow melt in SPHY are extended by implementing to additional routines. The first extension is a parameterization for the downslope transport of snow through avalanches. In the steep mountains of the upper Indus basin, this process of snow transport is very important. For this study, we implemented the SnowSlide routine [Bernhardt and Schulz, 2010], which was successfully incorporated in a high-resolution modeling study in the Baltoro watershed [Immerzeel *et al.*, 2013b]. The second extension is a parameterization for the sublimation of snow. The sublimation of snow is an important component in the water balance, especially in conditions with strong wind [Bowling *et al.*, 2004; Macdonald *et al.*, 2009; Wagnon *et al.*, 2013]. At the same time this component is difficult to quantify, especially when no data on wind speed is available, like it is the case in this large scale study. We estimate the sublimation using a calibrated relation between potential sublimation and elevation. Theoretically, the sublimation increases with elevation due to increases in wind speed and exposure of snow to wind with elevation and lowering air pressure with elevation.

The SPHY model is run for 2000-2007 at a daily time step and for each 1x1 km pixel the average snow cover is calculated for the same 46 periods as in the MODIS observed snow cover dataset. Subsequently these simulated snow cover maps are resampled to 0.05° spatial resolution, which is the native resolution of the MODIS product. Table 14 lists the calibrated parameter values.

Table 14: Calibrated values for snowmelt related parameters in the SPHY-model.

Parameter name	Symbol	Value
Degree day factor for snow	DDF _S	5.0 mm w.e. day ⁻¹
Critical temperature for precipitation to fall as snow	TCrit	2.0 °C
Water storage capacity of snow pack	SnowSC	0.5 mm mm ⁻¹
Minimum slope for gravitational snow transport	Sm	0.2
Minimum snow holding depth	ShdMin	50 mm
Snow holding depth threshold function parameters	SS1	50
	SS2	-10
Potential sublimation function	SubPot	0.0021 H - 6.3298 for H > 3000 m a.s.l.

Figure 29 shows the average observed and simulated fractional snow cover for the 46 periods during 2000-2008. From the figure it is clear that the observed and simulated snow cover show a good correspondence. Figure 30 shows the same, but specified for the Himalaya, Hindu Kush and Karakoram subareas (Figure 8). For the Himalaya and Hindu Kush subareas the SPHY model is very well able to simulate the observed snow cover. For the Karakoram region, the model performance is less good, but still satisfactory.



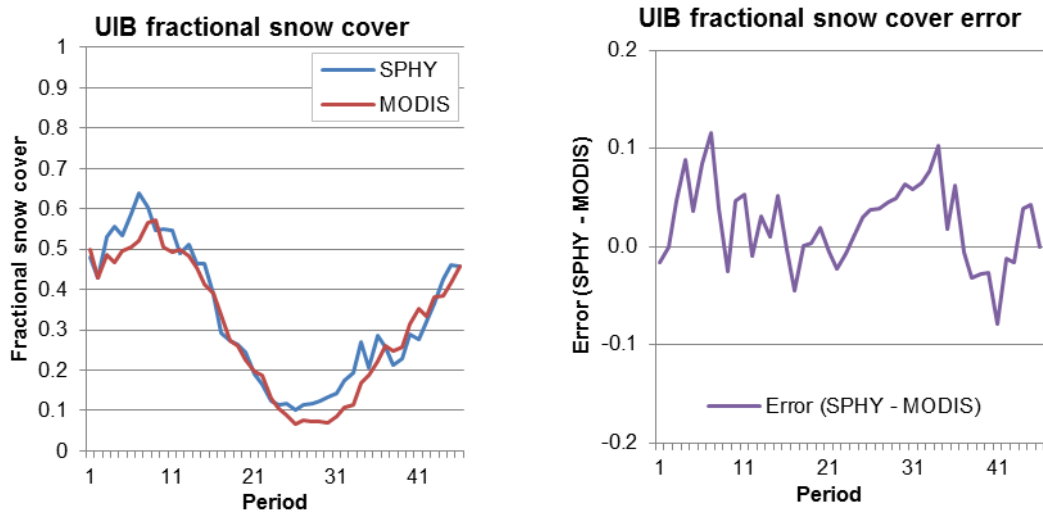


Figure 29: Left panel: Observed and simulated average fractional snow cover in the entire UIB (left panel). The values represent the average for the 46 periods during 2000-2008. Right panel: The difference in fractional snow cover between simulated and observed.

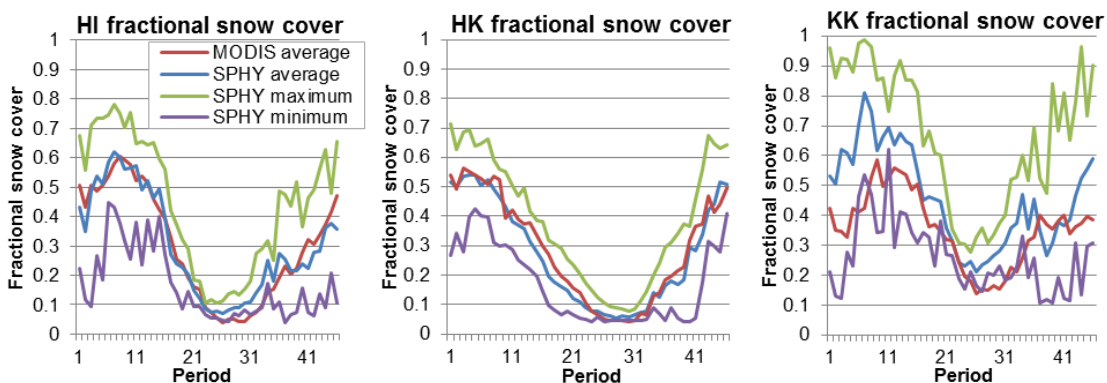


Figure 30: Observed and simulated fractional snow cover in three subareas within the UIB (HI=Himalaya, HK=Hindu Kush, KK=Karakoram, see Figure 8). Red line shows the average observed for 2000-2008, blue line shows the average simulated for 2000-2007, green line shows the maximum simulated for 2000-2007 and the purple line shows the minimum simulated for 2000-2007.

Figure 31 shows the spatial variation in the ability of SPHY to simulate the MODIS observed snow cover. These figures also show that the SPHY model has good ability to simulate the observed snow cover. The area with the largest error between simulated and observed snow cover are the highest areas in the Karakoram region. Besides the SPHY model shows some overestimation of snow cover for some valley bottoms.



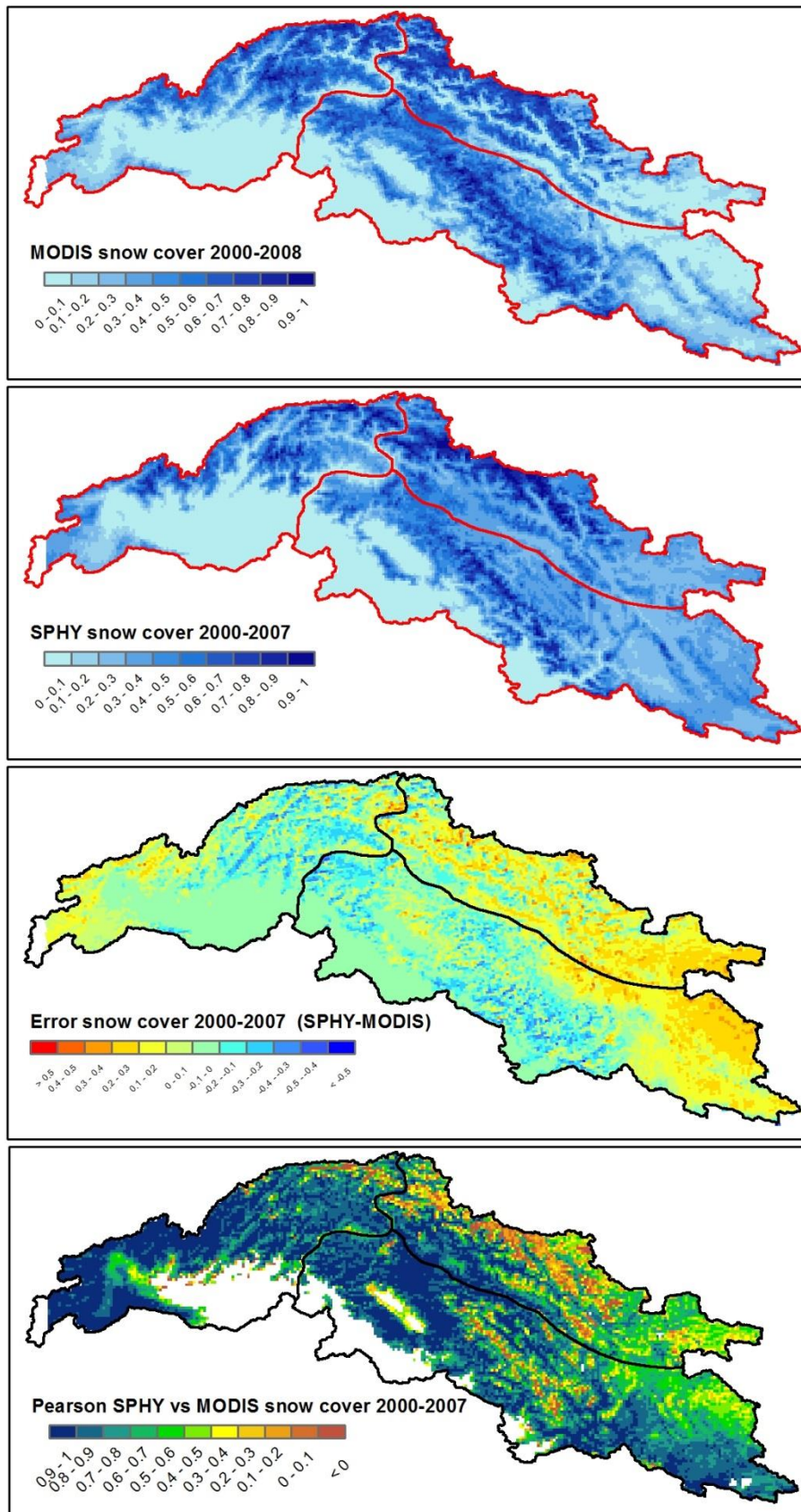


Figure 31: Average snow cover 2000-2008 according to MODIS (a), and 2000-2007 according to SPHY (b). Error SPHY-MODIS (c), and Pearson coefficient SPHY vs MODIS (d)



4.2.3 Calibration of parameters related to rainfall-runoff, baseflow and routing

Subsequent to the calibration of parameters related to glacier melt and snow melt, the parameters related to rainfall-runoff, baseflow and routing of runoff are calibrated. These parameters are calibrated to the observed stream flow at multiple locations in the UIB (Figure 32, Table 15).

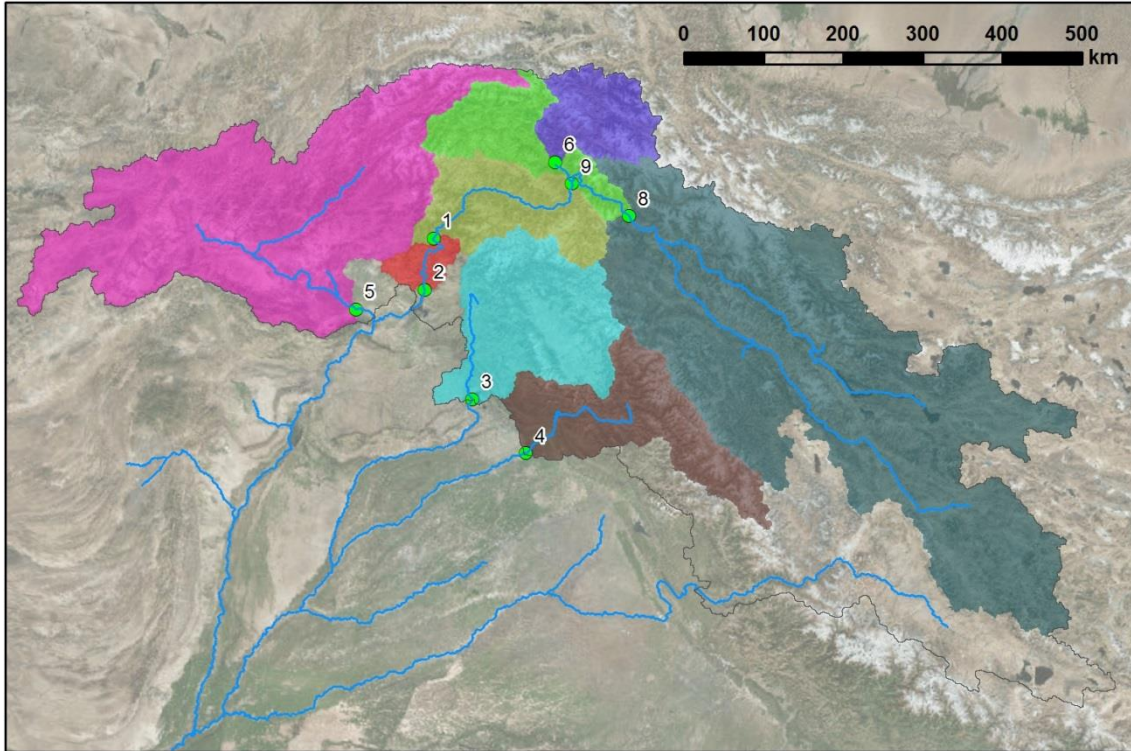


Figure 32: Locations of gauging stations which records where used for calibration and/or validation of the SPHY model.

Table 15: Gauging stations used for calibration and validation of the SPHY model.

ID	Name	River	source	LAT	LON	Interval	Period available
1	Besham Qila	Indus	SWHP/WAPDA	34.91	72.87	daily	2000-2007
2	Tarbela inflow	Indus	IMWI Pakistan	34.33	72.86	daily, 10 days	daily:4-2008 - 3-2009 10 days:4-1976 - 3-2011
3	Mangla inflow	Jhelum	IMWI Pakistan	33.20	73.66	daily, 10 days	daily:4-2008 - 3-2009 10 days:4-1976 - 3-2011
4	Marala inflow	Chenab	IMWI Pakistan	32.67	74.46	10 days	4-1976 - 3-2011
5	Nowshera inflow	Kabul	IMWI Pakistan	34.01	71.98	10 days	4-1976 - 3-2011
6	Dainyor bridge	Hunza	WAPDA	35.93	74.37	daily	1966-2010
8	Skardu - Kachura	Indus	WAPDA	35.43	75.47	daily	2005-2007
9	Partab - Partab Bridge	Indus	WAPDA	35.77	74.60	daily	2005-2007

The selection of stations is primarily dictated by data availability and access. Secondly the selection is refined to include as many parts of the basin as possible, with different hydrological regimes, and a range of catchment surface areas, ranging from large basins to smaller subcatchments. The observed and simulated discharges at gauging locations used for model calibration are shown in Figure 33. Gauging station locations 1, 3 and 6 were used for calibration of the rainfall-runoff and baseflow related model parameters. The starting date of the simulated period for the calibration of these parameters corresponds to the starting date of



longest available discharge record (1 January 1966) and the ending date corresponds to the ending date of the reference forcing dataset (31 December 2007). Averaged over the three locations, the Nash-Sutcliffe efficiency calculated for the daily values equals 0.70, whereas the average bias is -16.7% and Pearson's correlation coefficient equals 0.86.

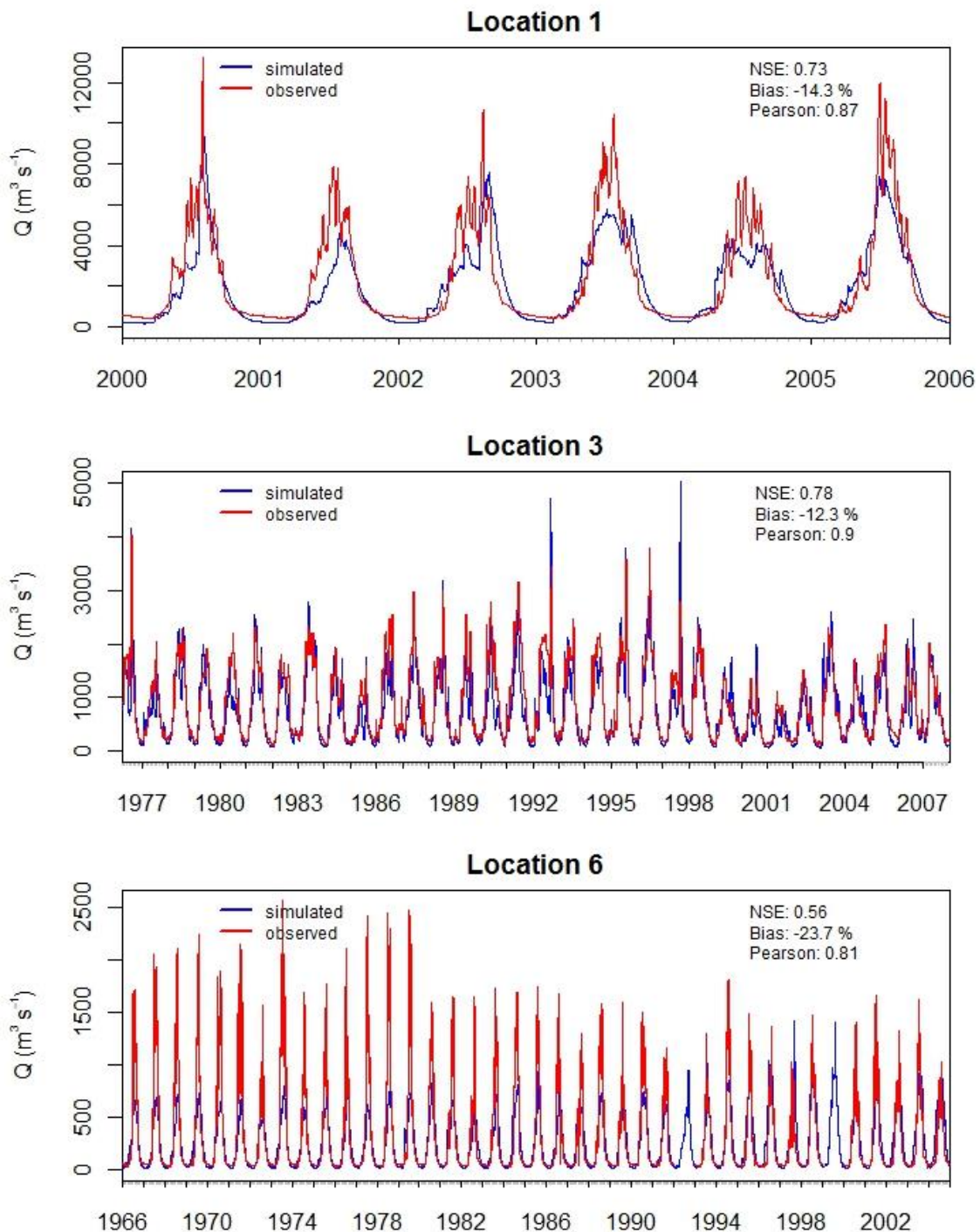


Figure 33: Observed and simulated flow for gauging station locations used for model calibration.

The largest bias at the daily scale is observed for the Hunza basin upstream of Dainyor bridge (location 6), which harbors the highest and most poorly meteorologically monitored part of the UIB and thus probably the uncertainty in the meteorological modelling forcing is largest there.



Noteworthy are also the difficulties for the model to simulate the highest peak flow as can be seen for location 1. Given the complexity of high mountain hydrology, the scale of the application with one parameter set for the entire basin and large uncertainties in the meteorological model forcing, we conclude that the model calibration is satisfactory.

4.3 Validation

Different locations than the locations used for model calibration were used for the independent model validation (locations 2,4,5). This was done for the remaining station locations for which daily or ten-daily data are available (Figure 34). In addition, the model performance was validated at numerous other locations where only long-term average discharge data is available (Table 16). In these cases, the observed long-term average is compared to the simulated long-term average.

The model validation at the three locations shows the most satisfactory results for the Indus at Tarbela (location 2), with its catchment covering the largest part of the UIB. Here, the model's Nash-Sutcliffe efficiency equals 0.67, average bias is -18.2% and Pearson's correlation coefficient equals 0.84. The simulation of the inflow at Marala (location 4), is less satisfactory, with a larger underestimate than at Tarbela. At Nowshera (location 5) on the other hand, the model overestimates the total flow, which might indicate that the positive correction of the precipitation as described in chapter 2 could be too strong in the Kabul subbasin.

The long timeframe of the reference forcing data spanning from 1961 until 2007 makes it possible to compare the simulated flows over this long period to long-term averaged discharges, which are reported in scientific literature (Table 16). Based on this validation, the overall conclusion is that the model satisfactorily simulates the observed flow at different locations with different catchment sizes and differing hydrological regimes, although the model performance shows strong spatial variation. This makes the model suitable for the major objective of this study: to assess changes in water availability in the future with respect to a historical reference.



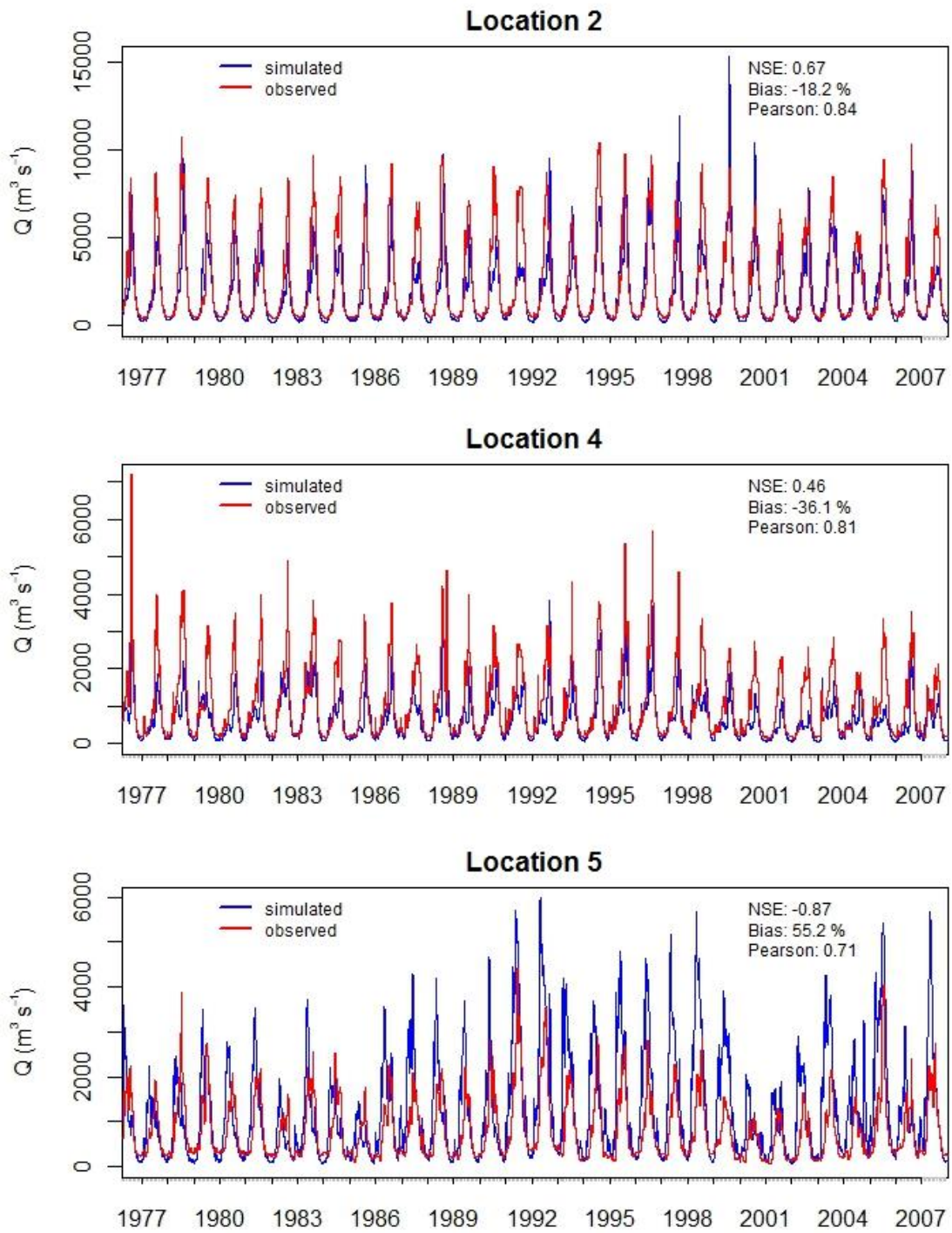


Figure 34: Observed and simulated flow for gauging station locations used for model validation.



Table 16: Validation of simulated discharge to observed long-term averaged discharge data.

Station	LAT	LON	Delineated catchment area (km ²)	Observed Q (m ³ s ⁻¹)	Period observed Q	Simulated Q (m ³ s ⁻¹)	Period simulated Q (m ³ s ⁻¹)
Yogo	35.18	76.10	64240	359.4**	1973-2010	261.5	1973-2007
Kharmong	34.93	76.22	70875	452.3**	1982-2010	435.5	1982-2007
Gilgit	35.93	74.30	13174	286.7**	1980-2010	218.4	1980-2007
Doyian	35.55	74.70	4000	135.7**	1974-2009	75.1	1974-2007
Chitral	35.87	71.78	12824	271.9***	1964-1996	193.4	1964-1996
Kalam	35.47	72.60	2151	89.6***	1961-1997	69.9	1961-1997
Naran	34.90	73.65	1181	48.1***	1960-1998	24.8	1961-1998
Alam bridge	35.77	74.60	28201	644.0**	1966-2010	472.8	1966-2007
Chakdara	34.65	72.02	5990	178.9***	1961-1997	160.8	1961-1997
Karora	34.90	72.77	586	21.2***	1975-1996	18.1	1975-1996
Garhi Habibullah	34.45	73.37	2493	101.8***	1960-1998	72.7	1961-1998
Muzafferabad	34.43	73.49	7604	357***	1963-1995	230.7	1963-1995
Chinari	34.16	73.83	14248	330***	1970-1995	319.8	1970-1995
Kohala	34.09	73.50	25820	828***	1965-1995	657.0	1965-1995
Kotli	33.53	73.89	2907	134***	1960-1995	39.3	1961-1995
Shigar	35.42	75.73	6681	202.6**	1985-1998	197.3	1985-1998
Phulra	34.32	73.08	1106	19.2****	1969-1996	34.8	1969-1996
Daggar	34.50	72.47	534	6.9****	1969-1996	9.3	1969-1996
Warsak	34.10	71.30	74092	593.0*****	1967-2005	919.2	1967-2005
Shatial Bridge	35.53	73.57	189263	2083.2**	1984-2009	1642.4	1984-2007

* Calculated using discharges made available by the Pakistan Water and Power Development (WAPDA), and delineated catchment area.

** From [Mukhopadhyay and Khan, 2014]

*** From [Sharif et al., 2013b].

**** Calculated using discharge (mm) reported in [Archer, 2003b] and delineated catchment area.

***** Calculated using discharge (mm) reported in [Khattak et al., 2011b] and delineated catchment area.

4.4 Current hydrology

The calibrated and validated model is run from 1 January 1961 until 31 December 2007 with a daily time step to gain insight in the characteristics of the historic regional hydrology. A historical period spanning 30 years from 1971 until 2000 is defined as the reference period. The model output for this period is used as a reference that can be used for comparison with two future periods (near future: 2031-2060, and far future (2071-2100)).

The top left panel in Figure 35 shows the spatial distribution of all generated runoff during the reference period. The figure clearly shows a distinct pattern in the runoff generation. Glaciers generate glacier melt water mostly in the highly glaciated Karakoram and other mountain ranges in the Hindu-Kush and Himalayas. Strong south to north and east to west gradients are



visible in the intensity of the rainfall-runoff generation, consistent with the intensity of the monsoon that comes in from the southeast during the monsoon season. Most precipitation falls in the first mountain ranges. Also the clear relationship between altitude and rainfall-runoff intensity is clearly visible in the figure. Most snow melt runoff is generated in the Hindu Kush mountains in the Kabul basin, which receive a lot of precipitation from westerly systems during the winter months. Also a lot of snow melt is generated in the southeastern part of the basin with a high precipitation intensity, The runoff that is generated on the Tibetan Plateau is partly snow melt runoff and partly rainfall-runoff.

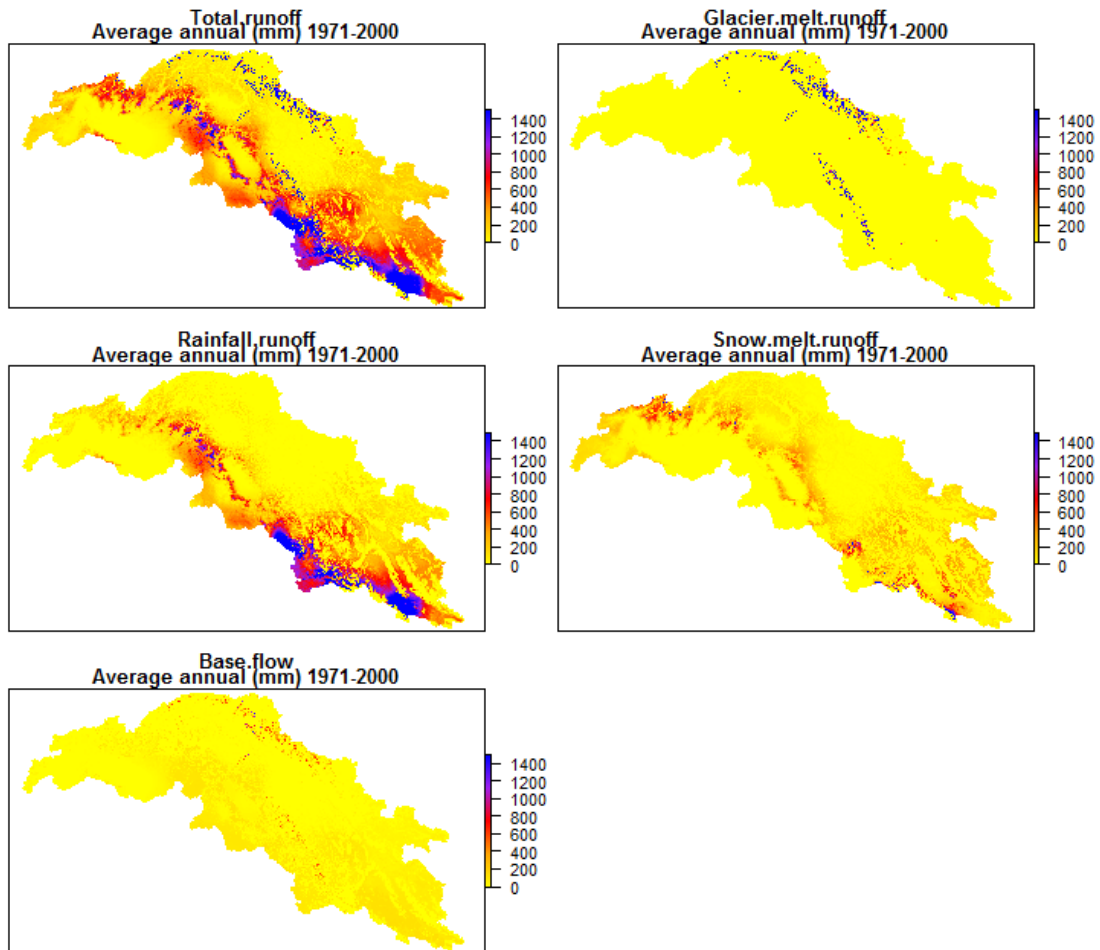


Figure 35: Average annual runoff generation in the UIB per 1x1 km model grid cell during the reference period, specified as total runoff (upper left panel) and per runoff component (other panels).

The runoff that is generated is transported downstream and runoff from different sources mixes in the river system. Figure 36 indicates the relative contribution of glacier melt, snow melt and rainfall-runoff to the total runoff for the major streams in the basin. It clearly shows the gradient of decreasing dependency of rivers from upstream to downstream. The highest glacier melt dependency is observed in the most upstream parts of the streams in the Karakoram. This also makes the Indus river the most melt-water dependent river leaving the UIB. The Yarkhun river in the Kabul basin also has a strong glacier melt water dependency. At the outlet of the UIB however, the Kabul river is mostly dependent on snow melt, because its western tributaries mainly contribute water generated from snow melt, as this region receives a lot of snowfall during the winter months. Snow melt is also a large contributor for the tributaries of the Indus

coming from the Tibetan Plateau. The water leaving the UIB in the Satluj River is mostly rainwater since this subbasin receives most rainfall during the monsoon season.

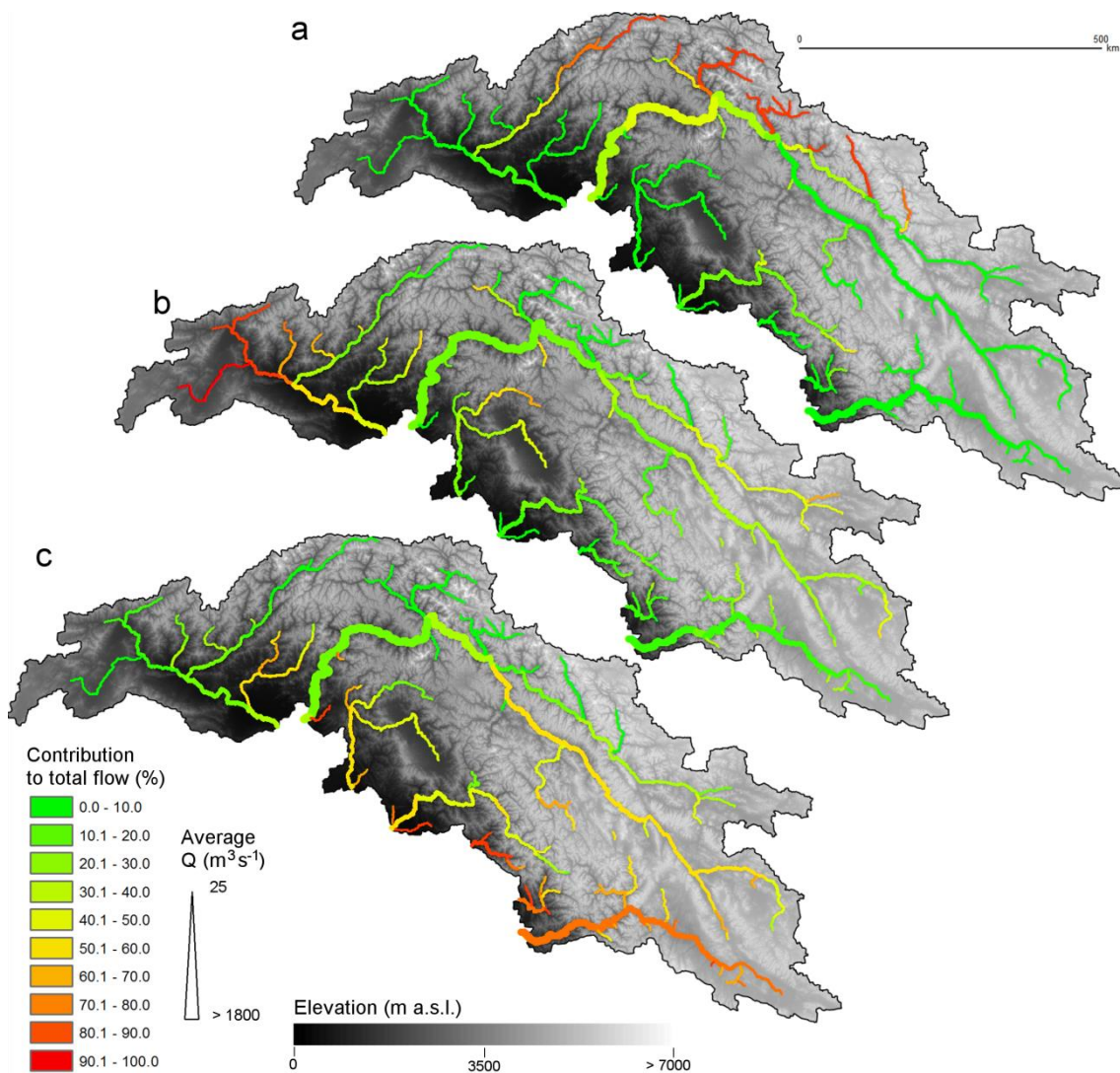


Figure 36: Contributions of glacier melt (a), snow melt (b) and rainfall-runoff (c) to the total flow (magnitude indicated by symbol size) averaged over the reference period (1971-2000).

Averaged over the entire UIB, 12.4% of the total runoff comes from glacier melt, 35.3% from snow melt, and 43.9% from rainfall (Table 17). However, as is clear from Figure 35 and Figure 36, the generation of total runoff as well as the runoff generated per contributor has a strong spatial variation within the basin. Therefore we analyse the model output separately for five subbasins within the UIB, that cover a large part of the UIB, catchment sizes, hydrological regimes and proximity to the glacier systems (Figure 37). We analyse the model results at the outlet of the UIB for the Kabul basin at Nowshera, the Indus at Tarbela and the Satluj. These subbasins cover large part of the basin and the northwest-southeast climatic gradient. In the Indus two additional subbasins are selected: The Hunza basin upstream of Dainyor bridge, which has the highest abundance of glaciers, and the Indus basin upstream of Skardu, which covers large part of the Karakoram and the northeastern part of the basin on the Tibetan Plateau.



Table 17: Hydro-meteorological characteristics of the entire UIB and five subbasins for the reference period (1971-2000).

(Sub)basin	Glacier-ized area (%)	P (mm yr ⁻¹)	Ratio rain/snow	Et _a (mm yr ⁻¹)	Other Losses* (mm yr ⁻¹)	Runoff (mm yr ⁻¹)	Contribution to total flow (%)			
							Glacier melt	Snow melt	Rainfall-runoff	Base flow
Total UIB	4.9	906	0.45 / 0.55	223	229	454	12.4	35.3	43.9	8.5
Indus - Tarbela	7.5	671	0.41 / 0.59	139	241	291	30.4	29.2	30.4	10.0
Kabul - Nowshera	1.8	805	0.57 / 0.43	272	132	400	6.4	59.6	28.7	5.3
Satluj outlet	2.4	1339	0.58 / 0.42	199	473	666	2.1	24.9	63.5	9.4
Hunza - Dainyor bridge	19.8	692	0.23 / 0.77	84	51	557	70.6	14.1	7.3	8.0
Indus - Skardu	7.2	601	0.37 / 0.63	124	269	207	33.1	23.6	30.1	13.3

*Other losses consist of losses through sublimation of snow, infiltration to deep groundwater and differences in storage).

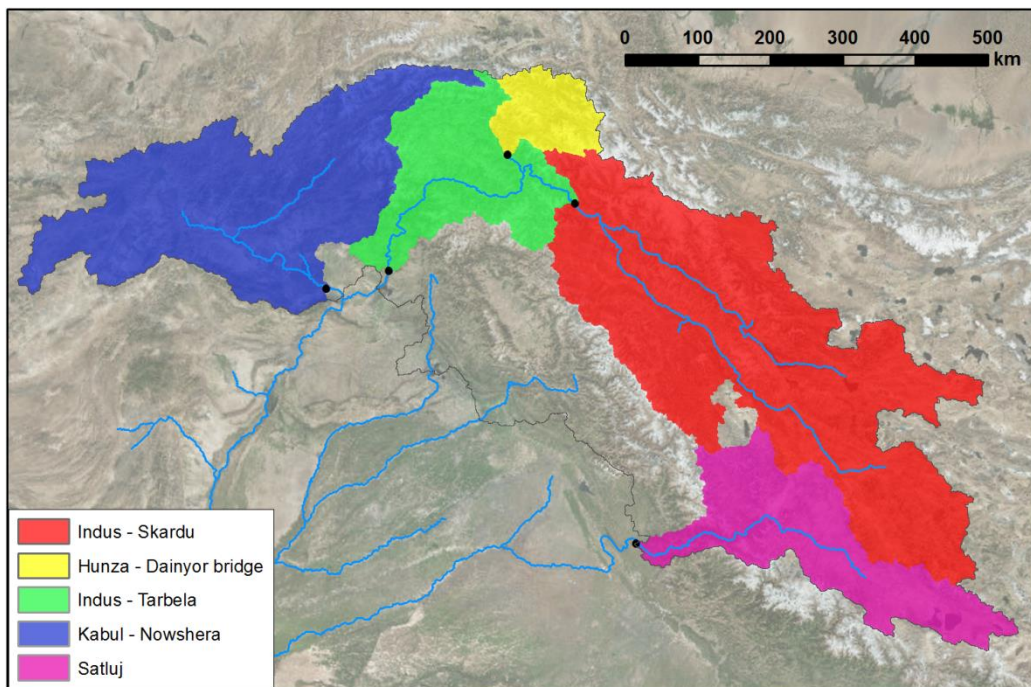


Figure 37: Five subbasins in the UIB. Note that the Hunza basin upstream of Dainyor bridge and the Indus basin upstream of Skardu are part of the Indus basin upstream of Tarbela.

Table 17 shows how contrasting these five basins are in terms of precipitation (amount and phase), presence of glaciers and runoff (amount and composition). The Satluj basin receives most precipitation with the majority of precipitation falling as rain, thus making it the basin with highest rainfall contribution to the runoff. The Indus has 30.4% glacier melt contribution at Tarbela, whereas its upstream tributary Hunza has 70.6% glacier melt contribution at Dainyor bridge. The Indus tributaries from the east have 33% glacier melt contribution at Skardu.

The amount and composition of flow also has strong seasonal variations.

Figure 38 shows the distribution and composition of the flow over the year. It clearly shows the peak flow of the Hunza river at Dainyor bridge when the glacier melt peaks. For the Indus at Skardu and Tarbela this glacier melt water peak is strongly enhanced by the monsoonal rains.



The Satluj peaks at the same time during the monsoon as it is rain-dominated, but also shows a clear peak in the snow melt during May and June. In the Kabul river at Nowshera the peak flow is dominated by the peak in snow melt, which is at its maximum in May.

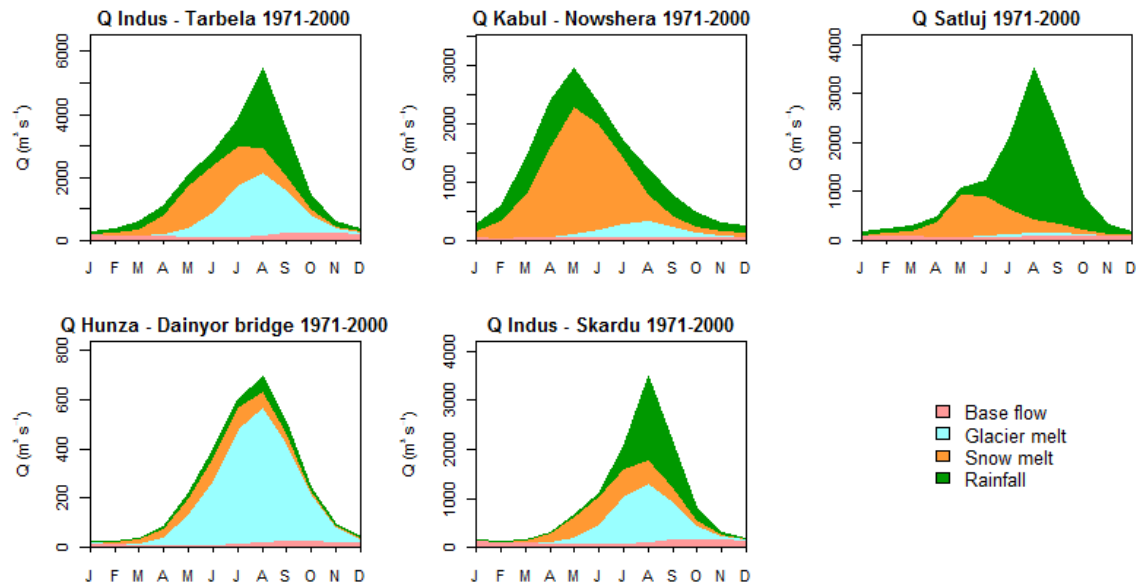


Figure 38: Simulated monthly averaged discharge and separation of runoff components for 1971-2000 at five locations in the UIB.

4.5 Future hydrological changes

To assess changes in the future hydrology, the calibrated and validated model is forced with the downscaled GCM-forcing in transient runs at a daily timestep from 1 January 2001 until 31 December 2100. In total eight model runs are done (2 RCPs x 4 GCMs), covering the entire envelope of possible future climates according to the CMIP5 multi-model ensemble for these two RCPs (see chapter 3).

4.5.1 Changes in glacier extent

Given the strong dependence of many rivers in the Indus basin, the future of the glacier extent in the UIB is a crucial factor for the future hydrology in the basin. At the same time, projecting the future of the glacier cover at the large river basin scale is difficult because the downslope transport of ice cannot be resolved in models running at spatial resolutions in the order of square kilometers, which is currently the highest possible resolution for river basin scale models. The available methods to estimate glacier changes at the large river basin scale are limited. In SPHY we use a parameterization of glacier changes at the large river basin scale [Lutz *et al.*, 2013], where we force a regionalized glacier mass balance model for three subzones (Figure 8), and estimate changes in the basins' glacier extent as a function of the glacier size distribution in the basins and projected temperature and precipitation. The model is calibrated for 2003-2007 against the average the observed mass balance in the basins according to IceSat data [Kääb *et al.*, 2012b]. Subsequently, projections for 2008 until 2100 are generated.



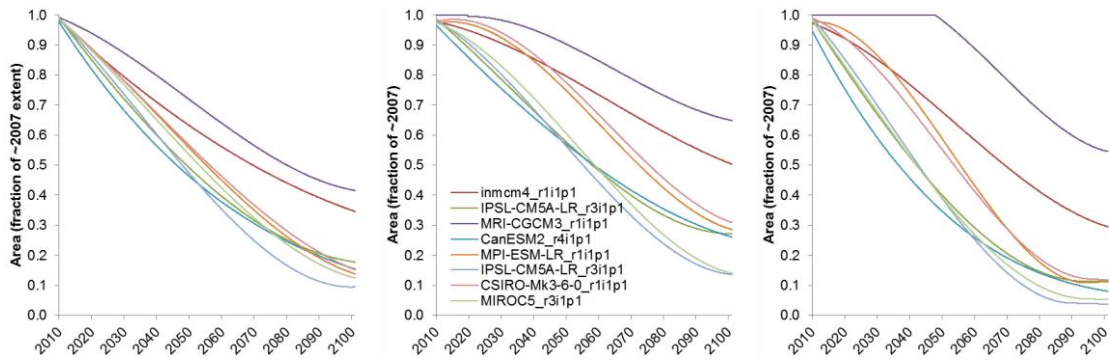


Figure 39: Projected changes in glacier extent for three subzones in the UIB. Left panel: Himalayas, middle panel: Karakoram, right panel: Hindu Kush. Projected changes for each multi-model ensemble member are shown.

The projected changes in glacier extent are the result of a close interplay of projected changes in temperature and precipitation, which are calculated at a monthly timestep in the parameterization approach. For the projections of glacier extent, the seasonal timing of the projected temperature and precipitation projections is very important as changes can apply to the ablation season in summer or to the accumulation season, which is during the winter months in the northwestern parts of the basins. Figure 39 shows the projection for each of the ensemble members in each of the three subzones. The projections have a strong uncertainty between ensemble members. For the Hindu Kush subzone projections range from almost no remaining glaciers at the end of the century to almost 60% remaining. One scenario in the Hindu Kush projects an expansion of the glacier area during the first decades of the 21st century. For the Karakoram the projections indicate 20 to 70% remaining ice at the end of the century. Strongest decreases are projected for the Himalayan subzone, with 10 to 50% remaining ice at the end of the century. The main factor leading to the large spread of glacier extent projections between the models is the large uncertainty in future precipitation, which feeds the glaciers.

4.5.2 Changes in water availability

This section discusses the changes in water availability and composition of runoff for the entire multi-model ensemble for two future time slices (2031-2060 and 2071-2100) with respect to the 1971-2000 reference period. Similar as in section 4.4, the changes are summarized for the entire UIB and five representative subbasins.



Table 18 lists the projected changes according for each GCM for the near future and the far future, for the entire UIB and the five subbasin, demonstrating the extremely large variability between the models and subbasins. These variations can be illustrated with the figures in the remainder of this section.



Table 18: Projected changes in the total UIB and five subbasins for the entire multi-model ensemble for two future periods (2031-2060 and 2071-2100) with respect to the reference period (1971-2000).

Basin	Period	RCP	Model	ΔP (%)	Ratio rain / snow	ΔET (%)	Δ total runoff (%)	Δ glacier melt runoff (%)	Δ snow melt runoff (%)	Δ rainfall-runoff (%)
Total UIB	2031-2060	RCP4.5	inmcm4_r1i1p1	-6	0.6 / 0.4	1	-7	-1	-21	2
			IPSL-CM5A-LR_r3i1p1	-9	0.66 / 0.34	5	-5	7	-38	17
			MRI-CGCM3_r1i1p1	8	0.6 / 0.4	8	11	15	-2	20
		RCP8.5	CanESM2_r4i1p1	5	0.68 / 0.32	20	10	1	-27	41
			MPI-ESM-LR_r1i1p1	-7	0.63 / 0.37	6	-5	15	-31	8
			IPSL-CM5A-LR_r3i1p1	-7	0.69 / 0.31	6	3	18	-40	32
			CSIRO-Mk3-6-0_r1i1p1	22	0.67 / 0.33	17	37	15	-10	83
	2071-2100	RCP4.5	MIROC5_r3i1p1	18	0.7 / 0.3	20	33	12	-18	80
			inmcm4_r1i1p1	-5	0.63 / 0.37	2	-6	-25	-24	14
			IPSL-CM5A-LR_r3i1p1	-10	0.69 / 0.31	7	-10	-44	-42	23
		RCP8.5	MRI-CGCM3_r1i1p1	6	0.6 / 0.4	11	6	-10	-1	18
			CanESM2_r4i1p1	0	0.7 / 0.3	24	-3	-41	-38	34
			MPI-ESM-LR_r1i1p1	-14	0.7 / 0.3	10	-15	-24	-51	15
			IPSL-CM5A-LR_r3i1p1	-16	0.74 / 0.26	13	-15	-44	-53	22
2031-2060	RCP4.5	CSIRO-Mk3-6-0_r1i1p1	40	0.73 / 0.27	36	61	-21	-6	143	
		MIROC5_r3i1p1	29	0.78 / 0.22	33	51	-38	-34	147	
		inmcm4_r1i1p1	-3	0.27 / 0.73	1	-2	-6	8	15	
	RCP8.5	IPSL-CM5A-LR_r3i1p1	-3	0.33 / 0.67	24	0	-10	15	68	
		MRI-CGCM3_r1i1p1	18	0.27 / 0.73	11	19	13	35	52	
		CanESM2_r4i1p1	8	0.36 / 0.64	40	2	-14	31	119	
		MPI-ESM-LR_r1i1p1	8	0.31 / 0.69	14	13	4	28	84	
2071-2100	RCP4.5	IPSL-CM5A-LR_r3i1p1	-2	0.35 / 0.65	27	9	-1	22	87	
		CSIRO-Mk3-6-0_r1i1p1	22	0.34 / 0.66	31	20	4	41	146	
		MIROC5_r3i1p1	22	0.38 / 0.62	50	16	-5	41	184	
	RCP8.5	inmcm4_r1i1p1	-9	0.29 / 0.71	5	-24	-33	2	29	
		IPSL-CM5A-LR_r3i1p1	-5	0.35 / 0.65	32	-35	-56	15	85	
		MRI-CGCM3_r1i1p1	13	0.28 / 0.72	17	-1	-13	30	61	
		CanESM2_r4i1p1	-3	0.39 / 0.61	54	-32	-53	4	111	
2031-2060	RCP4.5	MPI-ESM-LR_r1i1p1	4	0.39 / 0.61	40	-15	-40	32	157	
		IPSL-CM5A-LR_r3i1p1	-16	0.41 / 0.59	44	-39	-59	7	84	
		CSIRO-Mk3-6-0_r1i1p1	33	0.4 / 0.6	77	-2	-37	62	242	
	RCP8.5	MIROC5_r3i1p1	20	0.48 / 0.52	93	-16	-56	29	306	
		inmcm4_r1i1p1	-3	0.45 / 0.55	7	5	9	-25	23	
		IPSL-CM5A-LR_r3i1p1	1	0.52 / 0.48	27	22	31	-34	51	
		MRI-CGCM3_r1i1p1	9	0.39 / 0.61	12	12	21	7	10	
2071-2100	RCP4.5	CanESM2_r4i1p1	10	0.53 / 0.47	38	32	24	-21	78	
		MPI-ESM-LR_r1i1p1	3	0.45 / 0.55	20	17	33	-16	23	
		IPSL-CM5A-LR_r3i1p1	2	0.54 / 0.46	31	35	45	-30	71	
	RCP8.5	CSIRO-Mk3-6-0_r1i1p1	20	0.48 / 0.52	33	41	34	6	77	
		MIROC5_r3i1p1	25	0.58 / 0.42	44	71	38	-18	170	
		inmcm4_r1i1p1	0	0.47 / 0.53	13	5	-8	-20	32	
		IPSL-CM5A-LR_r3i1p1	2	0.53 / 0.47	33	6	-23	-25	56	
2031-2060	RCP4.5	MRI-CGCM3_r1i1p1	8	0.39 / 0.61	14	4	1	23	-3	
		CanESM2_r4i1p1	8	0.53 / 0.47	46	8	-18	-22	54	
		MPI-ESM-LR_r1i1p1	1	0.5 / 0.5	42	6	7	-15	18	
	RCP8.5	IPSL-CM5A-LR_r3i1p1	-3	0.58 / 0.42	49	5	-17	-22	46	
		CSIRO-Mk3-6-0_r1i1p1	34	0.53 / 0.47	65	54	11	30	122	
		MIROC5_r3i1p1	42	0.69 / 0.31	80	98	-10	-16	302	
		inmcm4_r1i1p1	-5	0.47 / 0.53	4	-1	2	-19	10	
2071-2100	RCP4.5	IPSL-CM5A-LR_r3i1p1	-4	0.53 / 0.47	21	6	12	-30	28	
		MRI-CGCM3_r1i1p1	9	0.44 / 0.56	10	14	17	7	21	
		CanESM2_r4i1p1	6	0.55 / 0.45	31	16	7	-20	57	
	RCP8.5	MPI-ESM-LR_r1i1p1	0	0.49 / 0.51	15	9	20	-16	20	
		IPSL-CM5A-LR_r3i1p1	-3	0.56 / 0.44	23	16	24	-28	45	
		CSIRO-Mk3-6-0_r1i1p1	20	0.52 / 0.48	26	36	20	1	87	
		MIROC5_r3i1p1	20	0.59 / 0.41	36	45	18	-13	121	
2031-2060	RCP4.5	inmcm4_r1i1p1	-6	0.49 / 0.51	9	-8	-20	-25	14	
		IPSL-CM5A-LR_r3i1p1	-5	0.55 / 0.45	26	-10	-39	-30	33	
		MRI-CGCM3_r1i1p1	7	0.44 / 0.56	12	4	-6	8	14	
	RCP8.5	CanESM2_r4i1p1	0	0.56 / 0.44	39	-8	-34	-34	39	
		MPI-ESM-LR_r1i1p1	-5	0.55 / 0.45	32	-5	-15	-29	25	
		IPSL-CM5A-LR_r3i1p1	-11	0.6 / 0.4	36	-14	-37	-36	25	
		CSIRO-Mk3-6-0_r1i1p1	33	0.57 / 0.43	54	46	-12	17	133	
2071-2100	RCP4.5	MIROC5_r3i1p1	31	0.69 / 0.31	64	54	-31	-24	205	
		inmcm4_r1i1p1	-7	0.59 / 0.41	-3	-5	-7	-10	8	
		IPSL-CM5A-LR_r3i1p1	-18	0.67 / 0.33	-5	-19	-19	-38	20	
	RCP8.5	MRI-CGCM3_r1i1p1	8	0.64 / 0.36	11	17	21	-5	59	
		CanESM2_r4i1p1	4	0.69 / 0.31	18	6	-27	-21	67	
		MPI-ESM-LR_r1i1p1	-13	0.68 / 0.32	1	-11	3	-38	40	



Satluj outlet	2071-2100	RCP4.5	IPSL-CM5A-LR_r3i1p1	-14	0.7 / 0.3	-7	-8	-9	-38	53
			CSIRO-Mk3-6-0_r1i1p1	15	0.69 / 0.31	19	25	-1	-13	109
			MIROC5_r3i1p1	9	0.71 / 0.29	16	16	-15	-22	100
			inmcm4_r1i1p1	-15	0.63 / 0.37	-2	-19	-44	-28	4
			IPSL-CM5A-LR_r3i1p1	-22	0.7 / 0.3	-7	-25	-72	-47	29
	2031-2060	RCP4.5	MRI-CGCM3_r1i1p1	5	0.67 / 0.33	14	9	-14	-15	62
			CanESM2_r4i1p1	-8	0.75 / 0.25	19	-18	-72	-47	53
			MPI-ESM-LR_r1i1p1	-27	0.79 / 0.21	-11	-25	-61	-68	71
			IPSL-CM5A-LR_r3i1p1	-31	0.8 / 0.2	-10	-35	-79	-69	44
			CSIRO-Mk3-6-0_r1i1p1	29	0.75 / 0.25	37	42	-60	-18	189
	2071-2100	RCP8.5	MIROC5_r3i1p1	5	0.8 / 0.2	20	10	-75	-49	150
			inmcm4_r1i1p1	-10	0.66 / 0.34	6	-2	-8	-32	9
			IPSL-CM5A-LR_r3i1p1	-2	0.71 / 0.29	19	15	-5	-32	34
			MRI-CGCM3_r1i1p1	-1	0.61 / 0.39	13	4	4	4	5
			CanESM2_r4i1p1	4	0.71 / 0.29	21	23	-4	-29	46
2031-2060	RCP8.5	MPI-ESM-LR_r1i1p1	-8	0.68 / 0.32	20	0	8	-30	12	
		IPSL-CM5A-LR_r3i1p1	-3	0.74 / 0.26	25	17	8	-34	37	
		CSIRO-Mk3-6-0_r1i1p1	14	0.72 / 0.28	17	40	7	-25	70	
		MIROC5_r3i1p1	17	0.71 / 0.29	19	45	3	-7	70	
		inmcm4_r1i1p1	2	0.68 / 0.32	5	22	-37	-13	38	
2071-2100	RCP4.5	IPSL-CM5A-LR_r3i1p1	-3	0.75 / 0.25	27	17	-53	-36	41	
		MRI-CGCM3_r1i1p1	0	0.61 / 0.39	19	6	-27	22	2	
		CanESM2_r4i1p1	9	0.72 / 0.28	28	32	-51	-14	55	
		MPI-ESM-LR_r1i1p1	-9	0.76 / 0.24	40	6	-36	-39	24	
		IPSL-CM5A-LR_r3i1p1	-4	0.82 / 0.18	49	20	-51	-44	49	
2031-2060	RCP8.5	CSIRO-Mk3-6-0_r1i1p1	36	0.8 / 0.2	35	87	-35	-21	142	
		MIROC5_r3i1p1	41	0.81 / 0.19	35	101	-46	-6	156	

Figure 40 and Figure 41 show the simulated monthly averaged discharge for the near future (2031-2060) at the five locations in the UIB, to reveal intra-annual changes in flow. The mean projection for RCP4.5 shows increased flow for the Indus at Tarbela and Skardu and the Satluj. For the Hunza at Dainyor bridge, the flow is almost unchanged in the mean projection, implying that the retreating glaciers melt at higher rates. A slight shift towards earlier in the year can be observed for the snow melt peak at Skardu. The Kabul river at Nowshera shows a decrease in flow for the months where its flow currently peaks whereas an increase can be observed for the winter months, which is most probably related to a shift towards more winter precipitation falling as rain to higher elevations, in response to warming, thus increasing the direct rainfall-runoff in winter and decreasing the snow melt peak in April-June. The uncertainty is largest for the Kabul and Satluj.

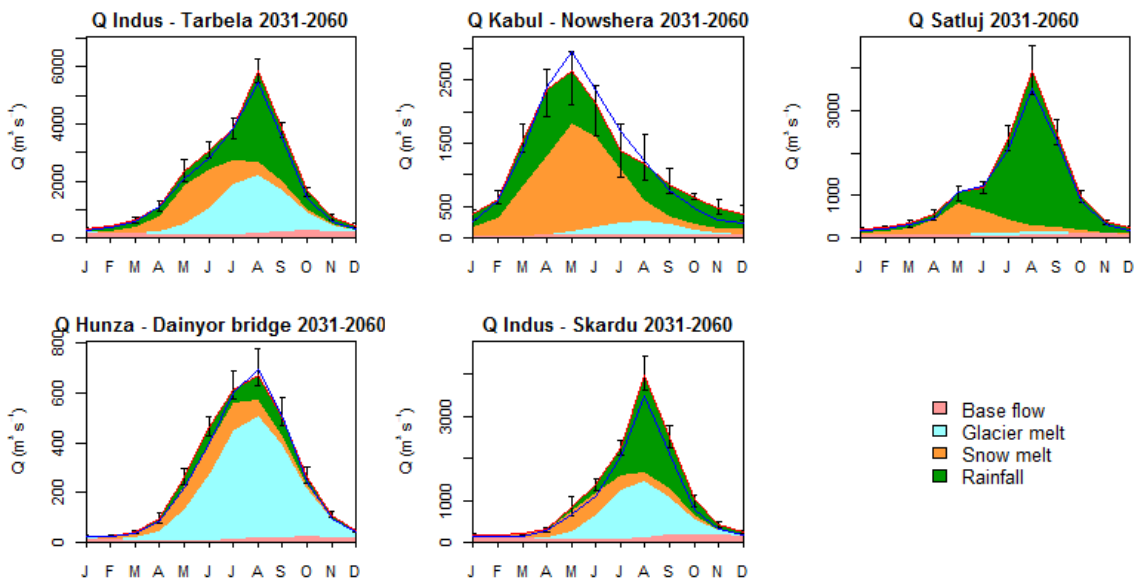


Figure 40: Simulated monthly averaged discharge and separation of runoff components at five locations in the UIB for 2031-2060 for the RCP4.5 ensemble. The red line indicates the mean projection and error bars indicate spread in the ensemble output. The blue line indicates the reference situation.



For RCP8.5 the picture differs a lot from RCP4.5 (Figure 41). The mean projection indicates clear increases in flow for the Indus at Tarbela, Hunza and Skardu and also for the Satluj. This is caused by a combination of increasing glacier melt and precipitation. Note that although the uncertainty of the flow projections is large, even the minimum projection shows increasing flows for each of these locations. The same trend of decreasing spring flows and increasing autumn/winter flows as for RCP4.5 can be seen for the Kabul at Nowshera, but with larger uncertainties.

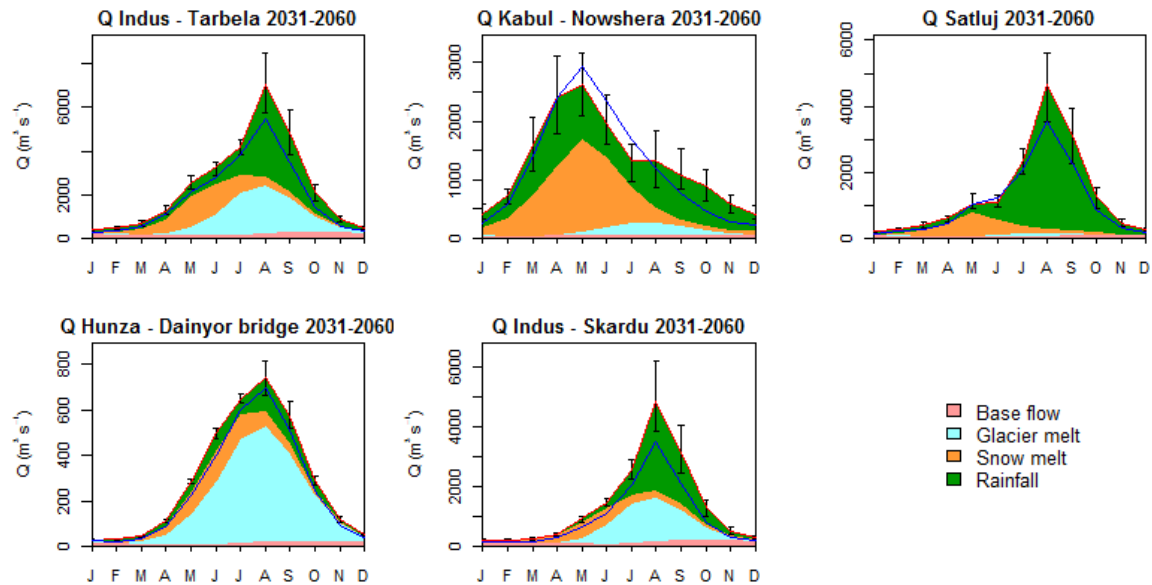


Figure 41: Simulated monthly averaged discharge and separation of runoff components at five locations in the UIB for 2031-2060 for the RCP8.5 ensemble. The red line indicates the mean projection and error bars indicate spread in the ensemble output. The blue line indicates the reference situation.

For August to December the uncertainty in the projections for Tarbela is very small, which is also the case for Skardu. This is probably related to the small spread in precipitation projections in the eastern part of the UIB for this ensemble in this time slice (Figure 22). On the other hand, the uncertainty is large for the Hunza basin, because of the large spread in projections of changes in glacier extent. The mean projection for the Satluj shows increasing flows due to increased precipitation, although with a large uncertainty, especially for August and September. The Kabul basin on the other hand shows decreasing flows. These contrasting projections are in line with the contrast between the mean precipitation projections for the eastern and western parts of the UIB for RCP4.5 for this time slice (Figure 22).

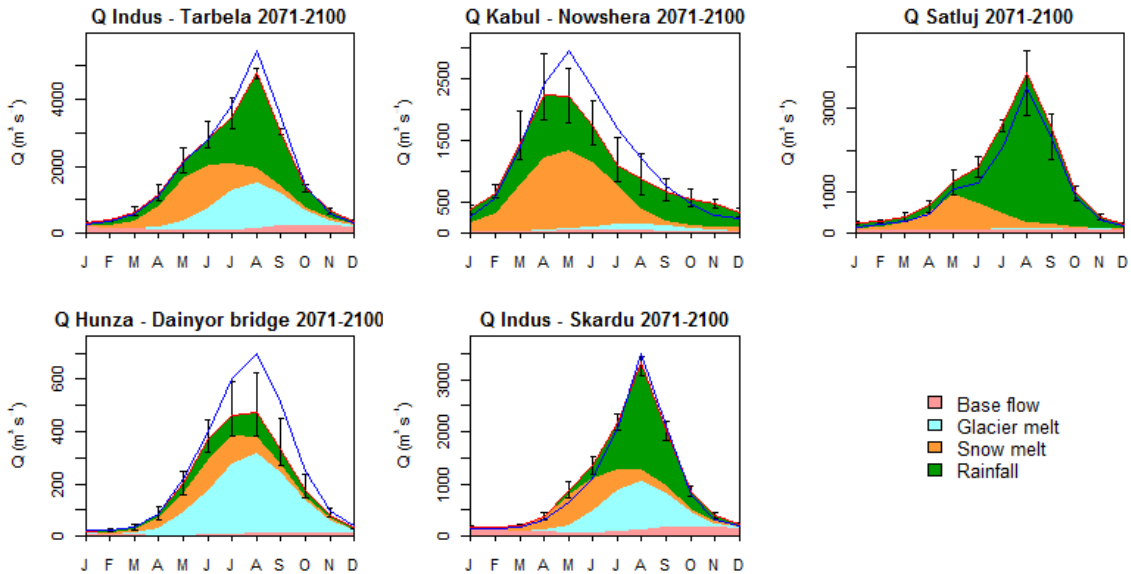


Figure 42: Simulated monthly averaged discharge and separation of runoff components at five locations in the UIB for 2071-2100 for the RCP4.5 ensemble. The red line indicates the mean projection and error bars indicate spread in the ensemble output. The blue line indicates the reference situation.

For the far future according to the RCP8.5 ensemble (Figure 43), the most striking are the very large uncertainties in the projections, which are a direct result of the large spread in precipitation projections in the ensemble members. Especially for the Kabul basin, the projections are very uncertain for each month in the year. The largest uncertainty for a single month is for August at Skardu. Note that the uncertainty for many months at four of these basins is even larger than the projected flow. All basins show a very clear shift of the snow melt peak towards earlier in the year.

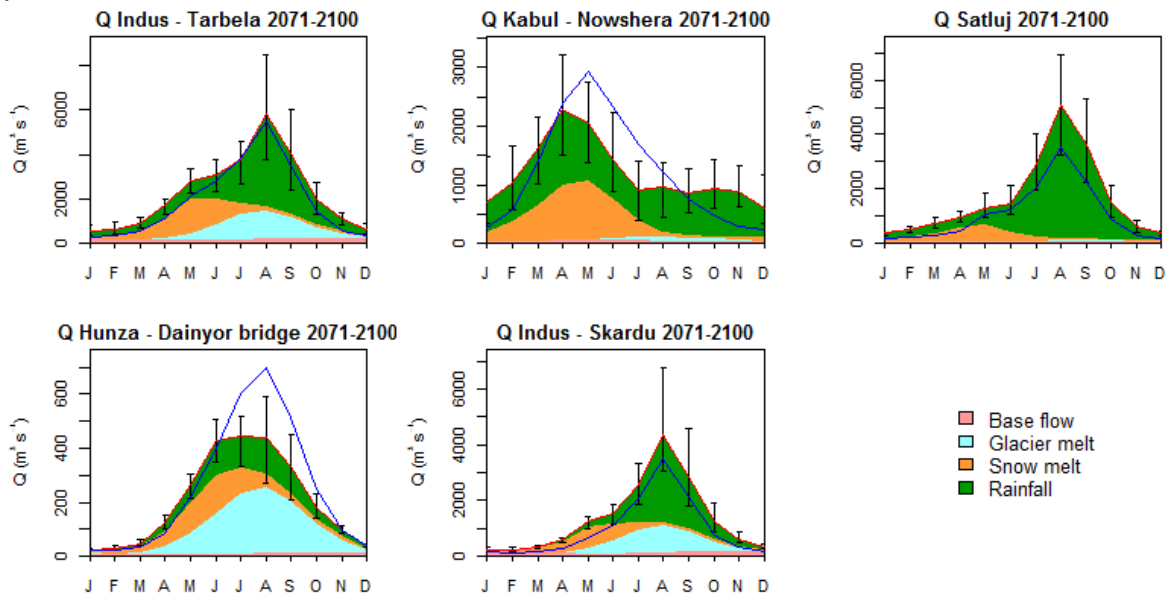


Figure 43: Simulated monthly averaged discharge and separation of runoff components at five locations in the UIB for 2071-2100 for the RCP8.5 ensemble. The red line indicates the mean projection and error bars indicate spread in the ensemble output. The blue line indicates the reference situation.



For the Satluj all ensemble members indicate an increase in total flow, whereas most also do for Skardu. The change in total water availability for the Kabul and Indus basins is very uncertain.

Figure 44 and Figure 45 show the annual average discharge for the entire simulated period spanning 140 years (1961-2100) for RCP4.5 and RCP8.5. These figures show how the glacier melt contribution to the total flow increase slightly from the 1960's until around 2030-2050, and then begins to decrease. The figures also show that the interannual variability in flow will increase for all subbasins. The RCP8.5 ensemble mean projects stronger increases in flow than the RCP4.5 ensemble mean, but also has a much larger uncertainty. In fact, these figures show that for most rivers in the UIB increasing water availability as well as decreasing water availability is very possible.

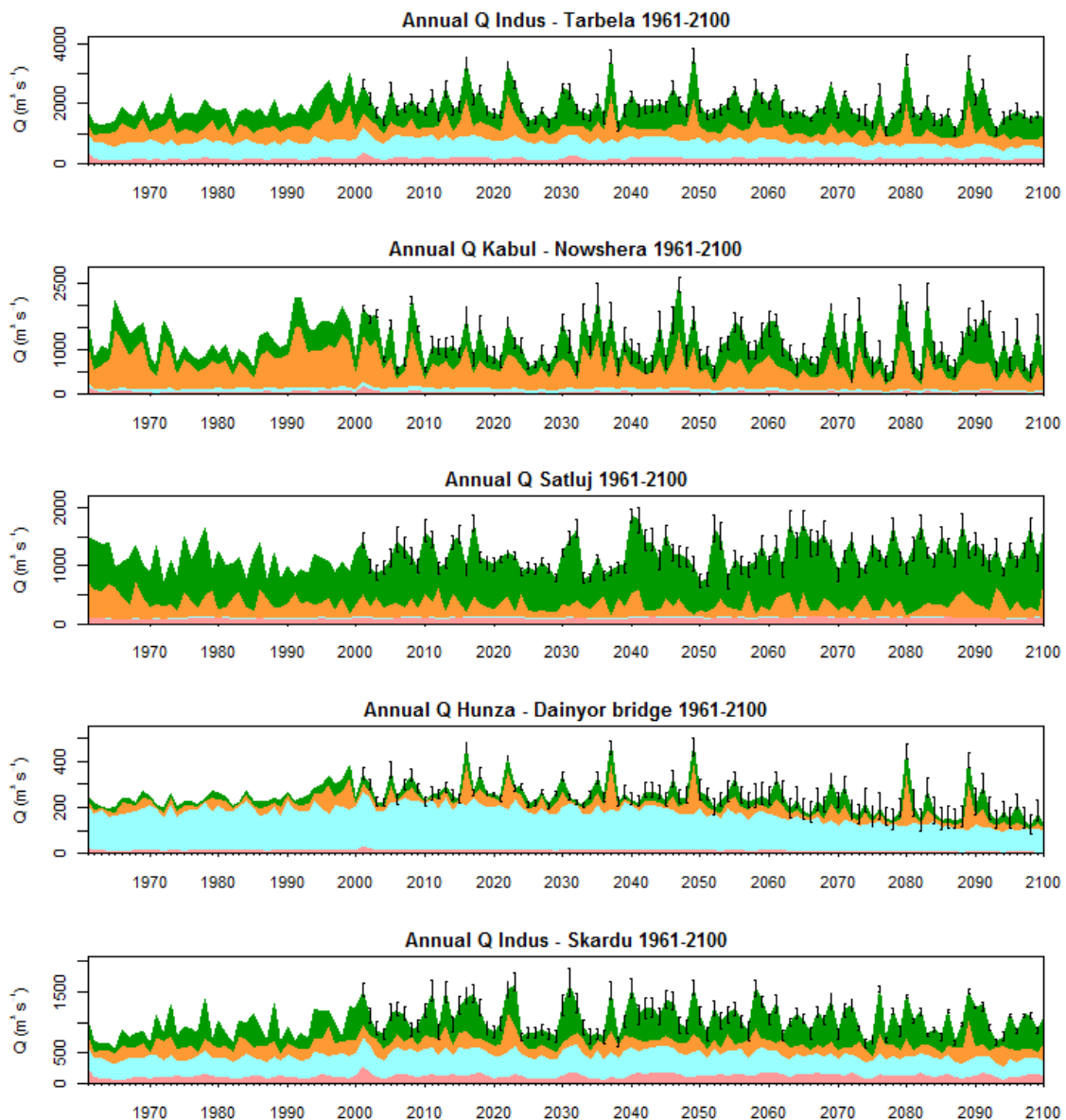


Figure 44: Time series annual averaged discharge at five locations in the UIB for the entire simulated period (1961-2100). Until 2000, the results for the baseline climate run are shown. After 2000 the mean of the model forced with the RCP4.5 ensemble is shown with error bars marking the spread in output from the entire ensemble.

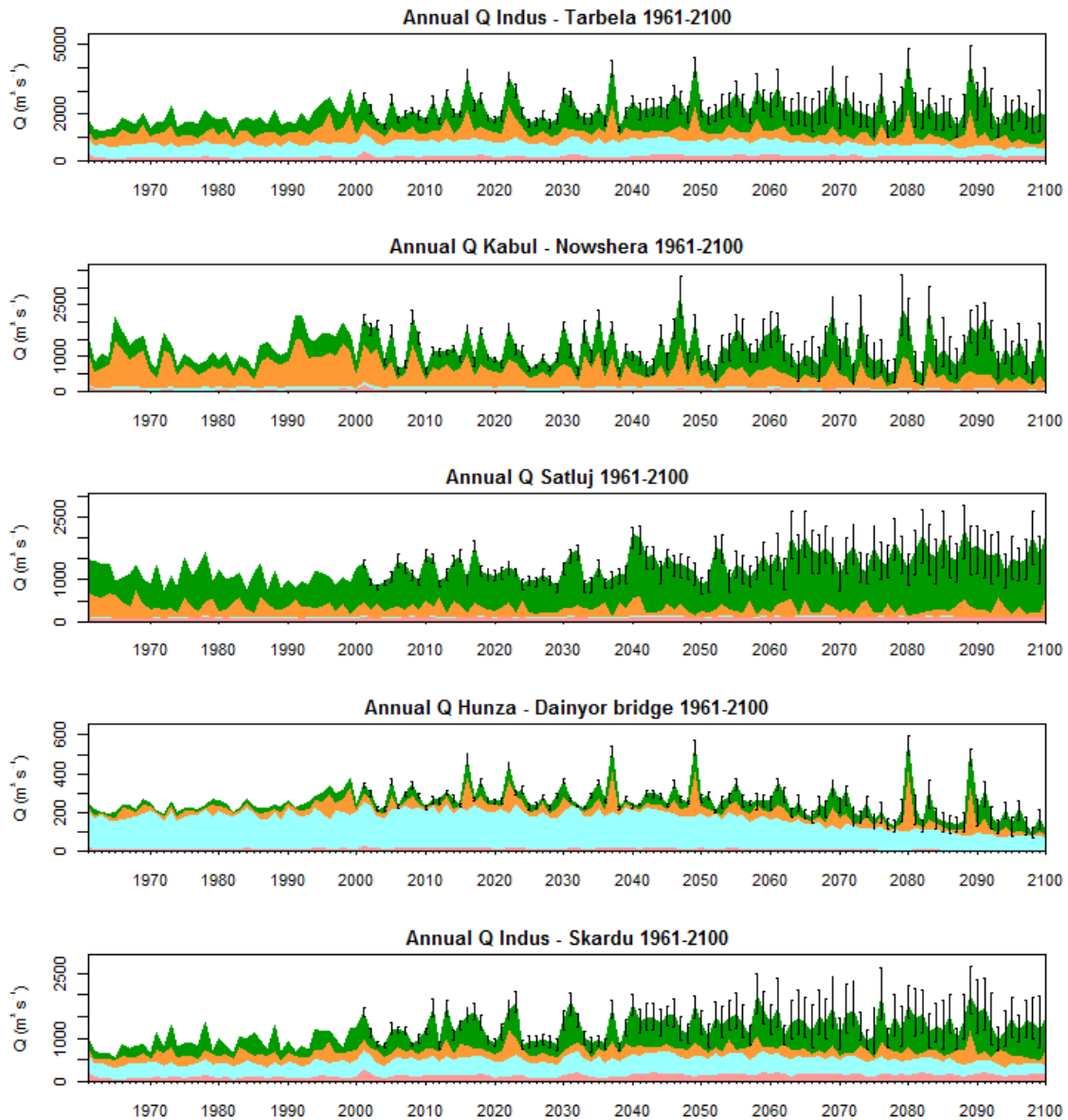


Figure 45: Time series annual averaged discharge at five locations in the UIB for the entire simulated period (1961-2100). Until 2000, the results for the baseline climate run are shown. After 2000 the mean of the model forced with the RCP8.5 ensemble is shown with error bars marking the spread in output from the entire ensemble.

4.5.3 Changes in hydrological extremes

The application of the Advanced Delta Change method, which projects changes in the distribution of precipitation intensity, makes it possible to project changes in the distribution of discharge intensity using the hydrological model. We do this for the same five locations in the UIB. Table 19 lists the projected changes in the distribution of daily discharge intensity for these five locations. The changes are further illustrated by flow duration curves for each of the locations and all ensemble members at the end of this section.



Table 19: Quantiles of daily discharge values at five locations in the UIB for the reference period, near future and far future for the model forced with each ensemble member in RCP4.5 and RCP8.5

Basin	Period	RCP	Model	Q50 (m ³ s ⁻¹)	Q75 (m ³ s ⁻¹)	Q90 (m ³ s ⁻¹)	Q95 (m ³ s ⁻¹)	Q99 (m ³ s ⁻¹)
Hunza - Dainyor bridge	1971-2000	-	Reference	142	423	648	733	934
	2031-2060	RCP4.5	CanESM2_rcp45	156	418	587	787	1097
			IPSL_CM5A_LR_rcp45	147	410	596	724	1114
			inmcm4_rcp45	143	423	602	698	968
			MRI_CGCM3_rcp45	192	507	722	825	1162
		RCP8.5	CSIRO_Mk3_6_0_rcp85	185	492	733	870	1207
			IPSL_CM5A_LR_rcp85	172	447	632	771	1232
			MIROC5_rcp85	175	477	687	844	1301
			MPI_ESM_LR_rcp85	175	477	671	811	1125
	2071-2100	RCP4.5	CanESM2_rcp45	107	237	366	572	1021
			IPSL_CM5A_LR_rcp45	95	224	349	566	1066
			inmcm4_rcp45	107	309	443	627	944
			MRI_CGCM3_rcp45	156	396	577	754	1095
		RCP8.5	CSIRO_Mk3_6_0_rcp85	162	353	543	811	1241
			IPSL_CM5A_LR_rcp85	102	189	300	481	1190
			MIROC5_rcp85	125	272	473	715	1467
			MPI_ESM_LR_rcp85	139	291	451	716	1288
	Indus - Skardu	1971-200	-	Reference	438	1303	2551	3511
2031-2060		RCP4.5	CanESM2_rcp45	617	1704	3210	4654	7236
			IPSL_CM5A_LR_rcp45	544	1561	3076	4347	6677
			inmcm4_rcp45	434	1360	2591	3776	6261
			MRI_CGCM3_rcp45	552	1533	2715	3674	5980
		RCP8.5	CSIRO_Mk3_6_0_rcp85	662	1783	3694	4979	7558
			IPSL_CM5A_LR_rcp85	618	1715	3352	4766	7495
			MIROC5_rcp85	750	1965	4615	6452	9610
			MPI_ESM_LR_rcp85	573	1527	2820	3932	6173
2071-2100		RCP4.5	CanESM2_rcp45	545	1337	2522	3714	6024
			IPSL_CM5A_LR_rcp45	501	1260	2553	3908	6219
			inmcm4_rcp45	432	1340	2552	3772	5963
			MRI_CGCM3_rcp45	493	1455	2371	3463	5521
		RCP8.5	CSIRO_Mk3_6_0_rcp85	822	1992	3641	5122	7585
			IPSL_CM5A_LR_rcp85	612	1255	2284	3521	5575
			MIROC5_rcp85	912	2231	5389	7284	11009
			MPI_ESM_LR_rcp85	599	1414	2334	3342	5320
Indus - Tarbela		1971-2000	-	Reference	1134	2807	4462	5779
	2031-2060	RCP4.5	CanESM2_rcp45	1359	3137	5210	6562	10106
			IPSL_CM5A_LR_rcp45	1182	2825	4730	6121	9638
			inmcm4_rcp45	1065	2618	4372	5703	9167
			MRI_CGCM3_rcp45	1376	3219	4959	6101	9346
		RCP8.5	CSIRO_Mk3_6_0_rcp85	1562	3582	6174	7648	12577
			IPSL_CM5A_LR_rcp85	1324	3117	5104	6552	10649
			MIROC5_rcp85	1690	3745	6614	8611	13187
			MPI_ESM_LR_rcp85	1303	2985	4783	6103	9378
	2071-2100	RCP4.5	CanESM2_rcp45	1107	2282	4118	5484	8823
			IPSL_CM5A_LR_rcp45	1021	2181	4008	5502	9243
			inmcm4_rcp45	966	2331	4163	5627	8691
			MRI_CGCM3_rcp45	1310	2804	4532	5849	8678
		RCP8.5	CSIRO_Mk3_6_0_rcp85	1960	3717	5915	7475	11471
			IPSL_CM5A_LR_rcp85	1085	2048	3667	5058	7849
			MIROC5_rcp85	1757	3789	7093	9227	14594
			MPI_ESM_LR_rcp85	1212	2375	4038	5422	8577



	1971-2000	-	Reference	790	1804	2921	3601	4817
Kabul - Nowshera	2031-2060	RCP4.5	CanESM2_rcp45	839	1879	3015	3632	5420
			IPSL_CM5A_LR_rcp45	599	1430	2366	2942	4300
			inmcm4_rcp45	744	1688	2795	3413	4721
			MRI_CGCM3_rcp45	1034	2091	3188	3738	5143
		RCP8.5	CSIRO_Mk3_6_0_rcp85	1151	2102	3340	3982	5842
			IPSL_CM5A_LR_rcp85	659	1540	2752	3513	5216
			MIROC5_rcp85	926	2082	3265	4016	5944
			MPI_ESM_LR_rcp85	761	1449	2435	3139	4442
	2071-2100	RCP4.5	CanESM2_rcp45	577	1245	2488	3309	5344
			IPSL_CM5A_LR_rcp45	495	1165	2384	3174	4679
			inmcm4_rcp45	577	1334	2490	3155	4457
			MRI_CGCM3_rcp45	856	1791	3234	4050	5651
		RCP8.5	CSIRO_Mk3_6_0_rcp85	1305	2343	3611	4464	6421
			IPSL_CM5A_LR_rcp85	368	916	2145	3055	4950
			MIROC5_rcp85	794	1710	3406	4579	6750
			MPI_ESM_LR_rcp85	472	1154	2290	3197	5001
Satluj	2031-2060	RCP4.5	CanESM2_rcp45	591	1577	3770	5142	7616
			IPSL_CM5A_LR_rcp45	564	1544	3441	4627	6771
			inmcm4_rcp45	411	1272	3024	4198	6299
			MRI_CGCM3_rcp45	562	1404	2962	3993	5877
		RCP8.5	CSIRO_Mk3_6_0_rcp85	619	1781	4471	6055	8778
			IPSL_CM5A_LR_rcp85	549	1500	3509	4818	7112
			MIROC5_rcp85	762	1973	4403	5773	7951
			MPI_ESM_LR_rcp85	487	1309	2989	4068	6062
	2071-2100	RCP4.5	CanESM2_rcp45	692	1909	3998	5005	6806
			IPSL_CM5A_LR_rcp45	613	1576	3577	4621	6534
			inmcm4_rcp45	573	1771	3840	4826	6488
			MRI_CGCM3_rcp45	649	1558	2795	3675	5405
		RCP8.5	CSIRO_Mk3_6_0_rcp85	926	2449	5794	7775	10414
			IPSL_CM5A_LR_rcp85	686	1738	3305	4444	6410
			MIROC5_rcp85	1171	2918	6042	7361	9220
			MPI_ESM_LR_rcp85	619	1486	3052	3897	5326

For the Hunza river at Dainyor bridge, all models project increases in the high end of the discharge distribution. In general, the highest discharges are similar for the near future and the far future, although in general decreases in mean discharge are projected for the far future. The MIROC5 model in RCP8.5 for 2071-2100 projects the strongest increase in extreme discharges, while the projected increase in mean discharge is highest for the same period is projected by the CSIRO model. For the Indus at Skardu, mostly strong increases in the highest discharges are projected For the MIROC5 model in RCP8.5 the Q_{99} is even doubled with respect to the reference period. Also for the Indus at Tarbela, all models project increases in the highest discharges, despite part of the models projecting decreases in the total flow. Similar observations can be made for the Kabul and Satluj basins with mostly stronger increases in the highest discharges compared to the changes in the mean discharge, and in some cases increases in the highest discharges while the mean discharge is decreasing, as for example for the inmcm4 and MPI-ESM-LR models for the near future in the Satluj basin. The general conclusion can be drawn that increases in extreme discharges can be expected for most climate change scenarios in most parts of the UIB.



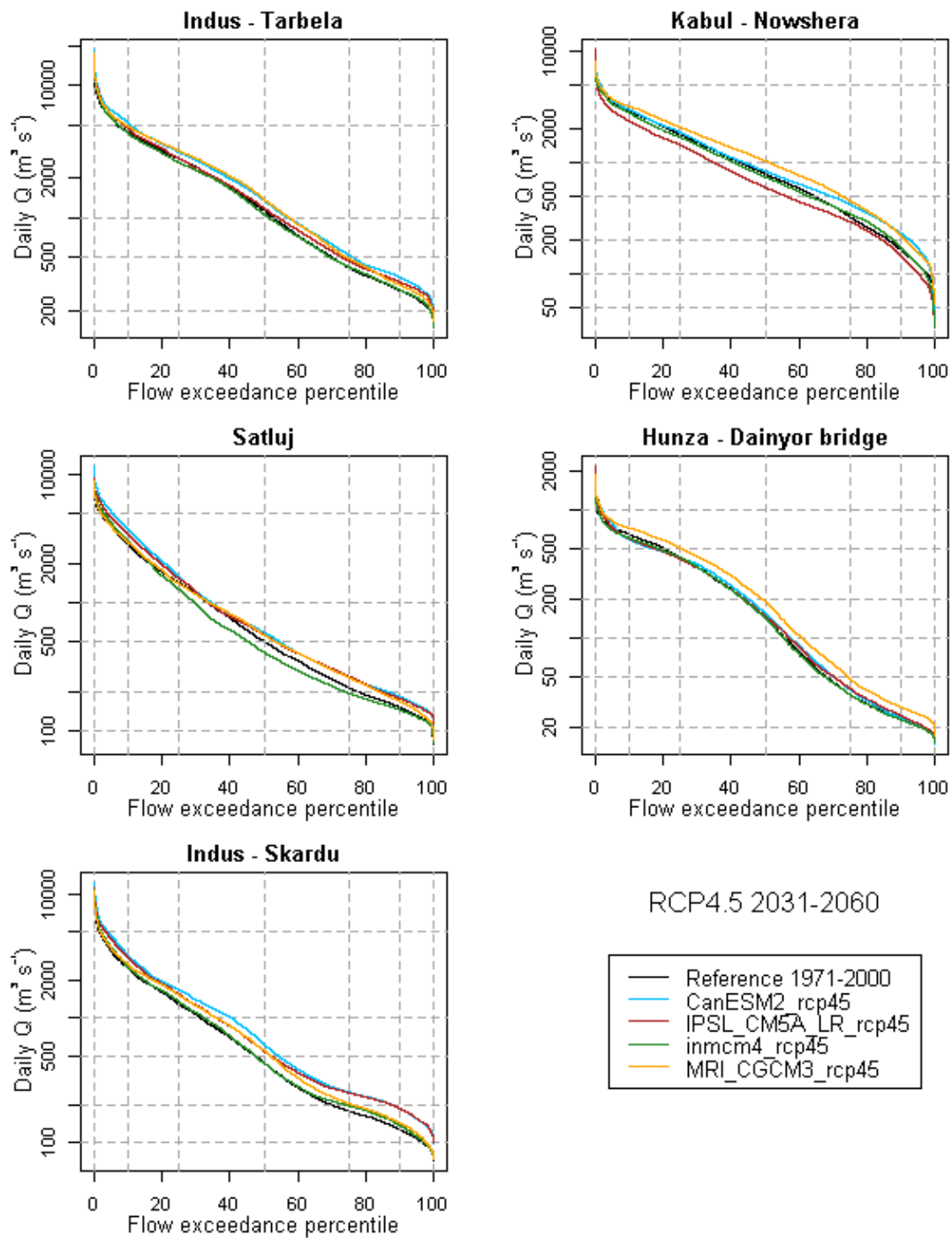


Figure 46: Flow duration curves for five locations in the UIB for SPHY forced with all RCP4.5 ensemble members for 2031-2060.



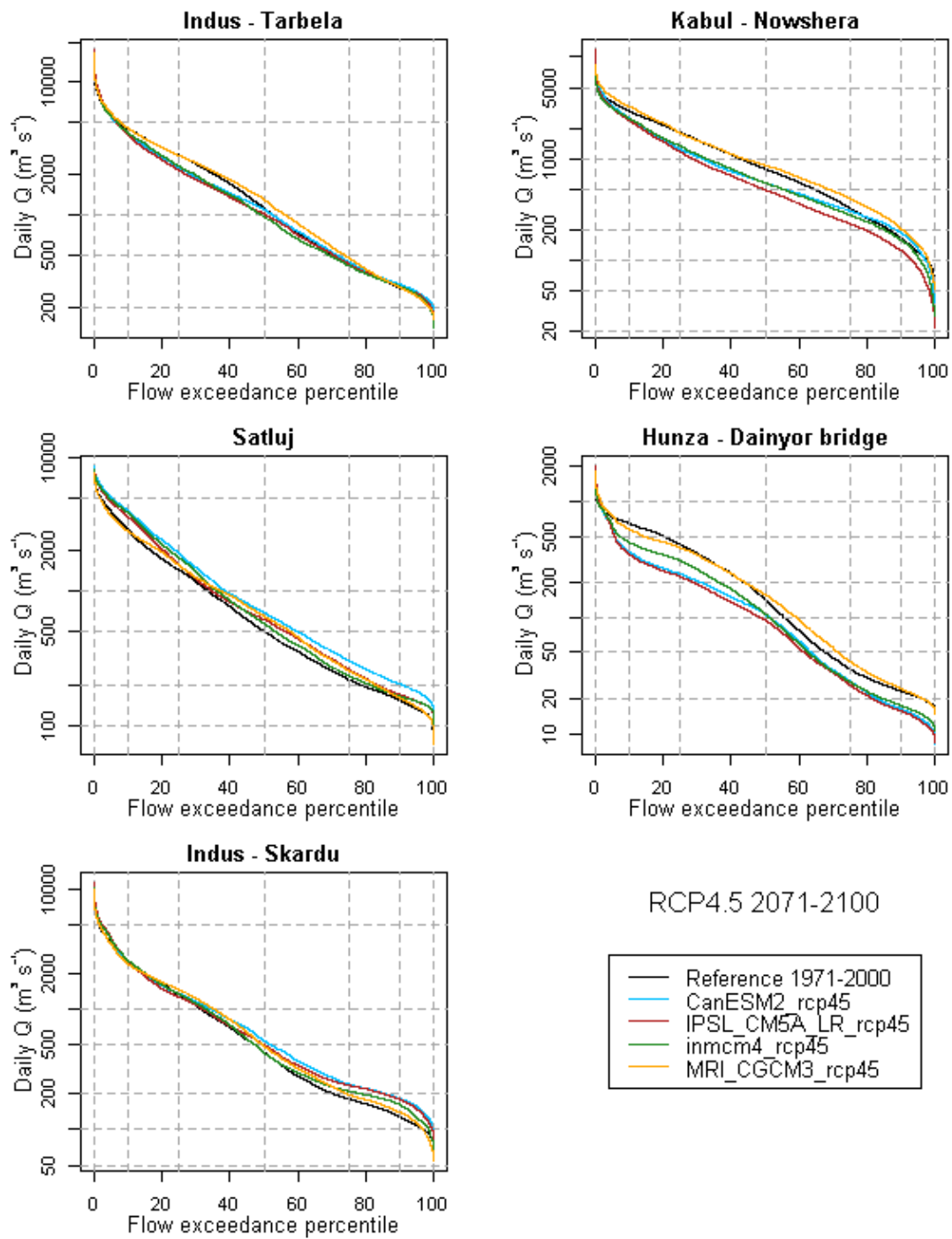


Figure 47: Flow duration curves for five locations in the UIB for SPHY forced with all RCP4.5 ensemble members for 2071-2100.



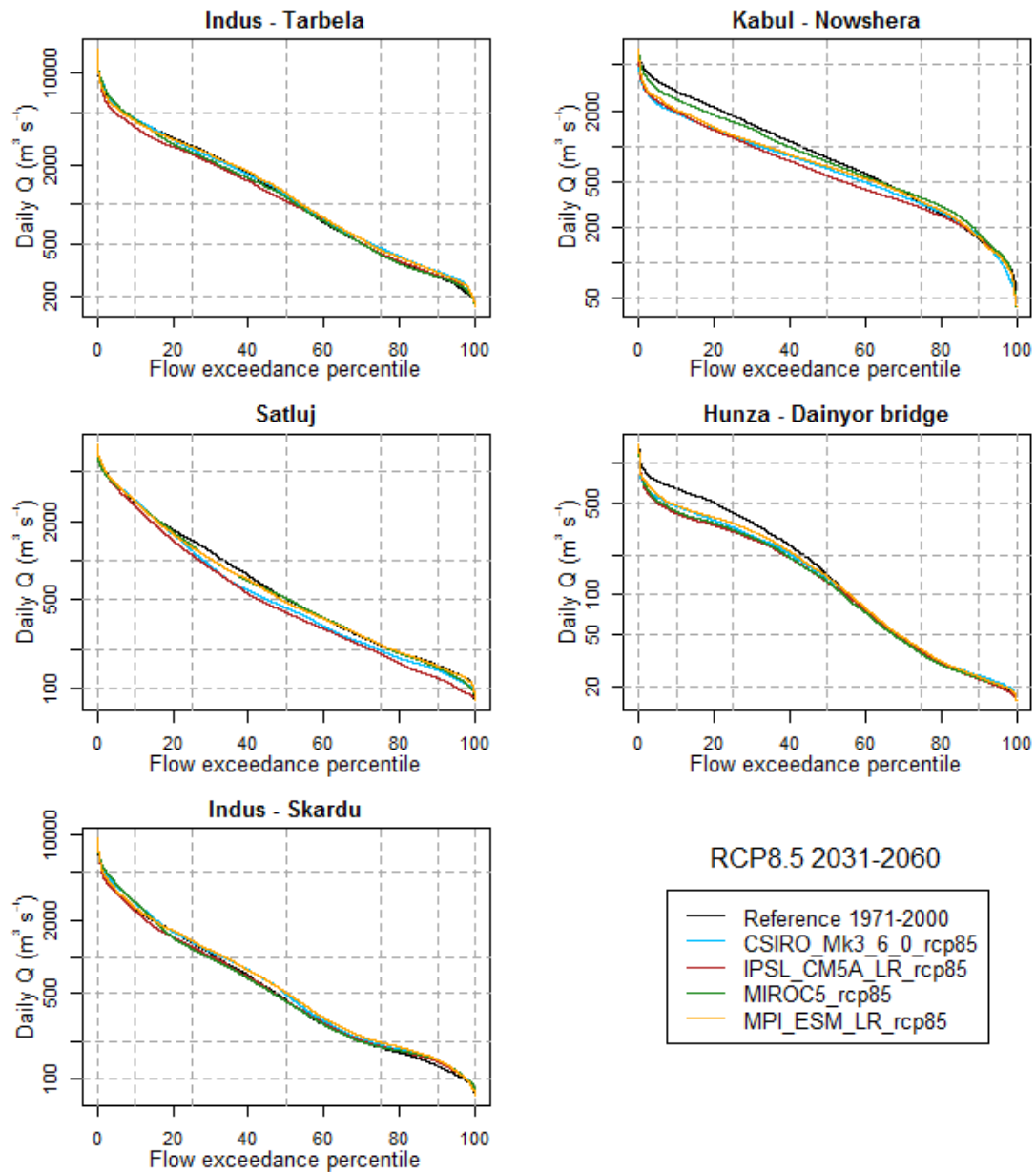


Figure 48: Flow duration curves for five locations in the UIB for SPHY forced with all RCP8.5 ensemble members for 2031-2060.



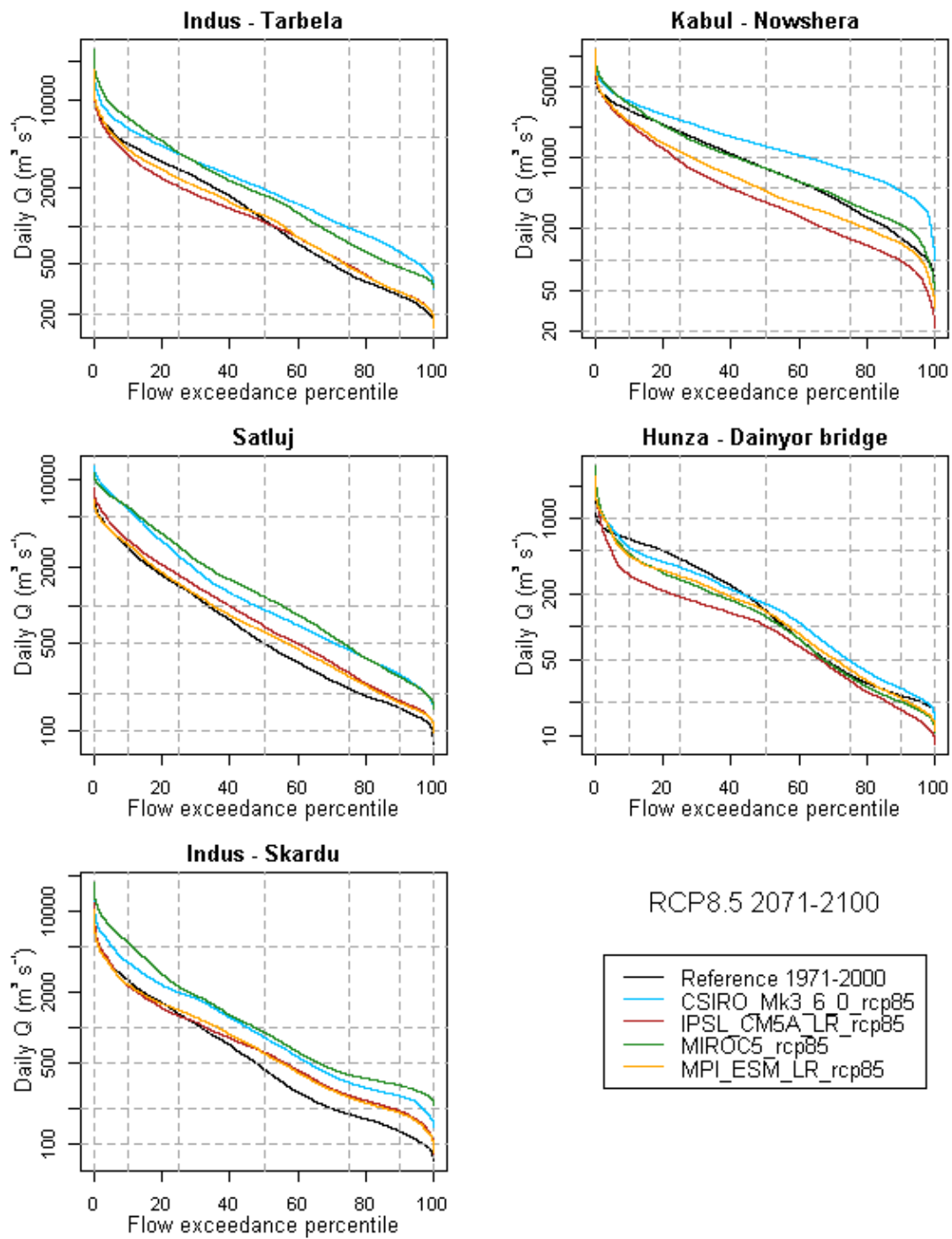


Figure 49: Flow duration curves for five locations in the UIB for SPHY forced with all RCP8.5 ensemble members for 2071-2100.



5 Conclusions and Recommendations

The Spatial Processes in Hydrology (SPHY) model has been systematically improved and set up for a 1961-2007 historical period with improved gridded meteorological data. Improvement of the existing APHRODITE precipitation product by using observed glacier mass balances as a proxy to estimate local precipitation gradients shows that:

- Averaged over the Upper Indus Basin, corrected precipitation is more than double of uncorrected precipitation.
- In the most extreme cases the corrected precipitation is a factor 5 to 10 than the uncorrected product

A downscaled ensemble of climate models in the CMIP5 multi-model ensemble for Representative Concentration Pathways 4.5 and 8.5 until 2100 shows that there is large uncertainty in the future climate of the Upper Indus basin:

- Projections of temperature change project increasing temperatures by ~ 2.0 to ~ 7.3 °C between 1971-2000 and 2071-2100. The uncertainty in the temperature projections is largest in the highest areas of the Upper Indus Basin.
- Projections of precipitation change project changes ranging from -15% to +35% averaged over the entire Upper Indus basin. Spatial and seasonal variations in these projections are extremely large with short distances between areas with projected precipitation increase and areas with projected precipitation decrease and large uncertainty between the models. It is likely that the frequency of extreme precipitation events will increase in most parts of the Upper Indus basin

Directly related to the high uncertainty in the precipitation projections, also large uncertainties are applicable to the water availability scenarios in the Upper Indus basin. Averaged over the entire Upper Indus basin:

- For 2031-2060 projections range from -7% to + 37%
- For 2071-2100 projections range from -15% to +60%

A large spatial variability and uncertainty in between models is observed in the water availability scenarios. Besides the uncertainty varies with the time of the year, with differing patterns in differing subbasins.

Analysis of changes in extreme discharges indicate that increases in discharge extremes can be expected for most of the Upper Indus Basin.

Recommendations for future work include further improvement of the hydrological model:

- The parameterization of sublimation, which is included in the SPHY model can be further improved. Sublimation is an important component of the water balance in areas which experience a lot of snow cover, like the Upper Indus basin. However, this process is not included in most models operating at the river basin scale. The strong relationship between wind speed and sublimation makes this a challenging task to incorporate at the large river basin scale.



- Improved routing routines can enhance the projections of changes in discharge extremes

Although it is recommendable to further improve the model to reduce the uncertainties in the hydrological model, the uncertainty introduced by uncertainties in the hydrological model are small compared to the uncertainty in the climate change scenarios, which is particularly large for the Upper Indus Basin.



References

- Andermann, C., S. Bonnet, and R. Gloaguen (2011), Evaluation of precipitation data sets along the Himalayan front, *Geochemistry, Geophys. Geosystems*, 12(7), 1–16, doi:10.1029/2011GC003513. [online] Available from: <http://doi.wiley.com/10.1029/2011GC003513> (Accessed 20 August 2013)
- Archer, D. (2003a), Contrasting hydrological regimes in the upper Indus Basin, *J. Hydrol.*, 274(1-4), 198–210, doi:10.1016/S0022-1694(02)00414-6. [online] Available from: <http://linkinghub.elsevier.com/retrieve/pii/S0022169402004146> (Accessed 11 October 2013)
- Archer, D. (2003b), Contrasting hydrological regimes in the upper Indus Basin, *J. Hydrol.*, 274(1-4), 198–210, doi:10.1016/S0022-1694(02)00414-6.
- Arendt, A. et al. (2012), Randolph Glacier Inventory – A Dataset of Global Glacier Outlines: Version 3.2.,
- Bajracharya, S. R., and A. B. Shrestha (2011), *The Status of Glaciers in the Hindu Kush-Himalayan Region*.
- “Batura Investigations Group” (1979), The Batura Glacier in the Karakoram Mountains and its variations., *Sci. Sin.*, 22(8), 958–974.
- Bernhardt, M., and K. Schulz (2010), SnowSlide: A simple routine for calculating gravitational snow transport, *Geophys. Res. Lett.*, 37(11), n/a–n/a, doi:10.1029/2010GL043086. [online] Available from: <http://doi.wiley.com/10.1029/2010GL043086> (Accessed 28 January 2014)
- Bowling, L. C., J. W. Pomeroy, and D. P. Lettenmaier (2004), Parameterization of Blowing-Snow Sublimation in a Macroscale Hydrology Model, *J. Hydrometeorol.*, 745–762.
- Droogers, P., and R. G. Allen (2002), Estimating reference evapotranspiration under inaccurate data conditions, *Irrig. Drain. Syst.*, 16, 33–45.
- Duncan, J. M. A., and E. M. Biggs (2012), Assessing the accuracy and applied use of satellite-derived precipitation estimates over Nepal, *Appl. Geogr.*, 34, 626–638, doi:10.1016/j.apgeog.2012.04.001. [online] Available from: <http://linkinghub.elsevier.com/retrieve/pii/S0143622812000276> (Accessed 23 August 2012)
- Farr, T. G. et al. (2007), The Shuttle Radar Topography Mission, *Rev. Geophys.*, 45(RG2004).
- Hewitt, K. (2005a), The Karakoram Anomaly? Glacier Expansion and the “Elevation Effect,” Karakoram Himalaya, *Mt. Res. Dev.*, 25(4), 332 – 340.
- Hewitt, K. (2005b), The Karakoram Anomaly? Glacier Expansion and the “Elevation Effect,” Karakoram Himalaya, *Mt. Res. Dev.*, 25(4), 332 – 340.
- Hewitt, K. (2007a), Tributary glacier surges: an exceptional concentration at Panmah Glacier, Karakoram Himalaya, *J. Glaciol.*, 53(181), 181–188, doi:10.3189/172756507782202829. [online] Available from: <http://openurl.ingenta.com/content/xref?genre=article&issn=0022-1430&volume=53&issue=181&spage=181>
- Hewitt, K. (2007b), Tributary glacier surges: an exceptional concentration at Panmah Glacier, Karakoram Himalaya, *J. Glaciol.*, 53(181), 181–188, doi:10.3189/172756507782202829.



- Hewitt, K. (2011a), Glacier Change, Concentration, and Elevation Effects in the Karakoram Himalaya, Upper Indus Basin, *Mt. Res. Dev.*, 31(3), 188–200, doi:10.1659/MRD-JOURNAL-D-11-00020.1.
- Hewitt, K. (2011b), Glacier Change, Concentration, and Elevation Effects in the Karakoram Himalaya, Upper Indus Basin, *Mt. Res. Dev.*, 31(3), 188–200, doi:10.1659/MRD-JOURNAL-D-11-00020.1.
- Hock, R. (2005), Glacier melt: a review of processes and their modelling, *Prog. Phys. Geogr.*, 29(3), 362–391, doi:10.1191/0309133305pp453ra. [online] Available from: <http://ppg.sagepub.com/cgi/doi/10.1191/0309133305pp453ra> (Accessed 30 July 2011)
- Huss, M. (2013), Density assumptions for converting geodetic glacier volume change to mass change, *Cryosph.*, 7(3), 877–887, doi:10.5194/tc-7-877-2013. [online] Available from: <http://www.the-cryosphere.net/7/877/2013/> (Accessed 24 March 2014)
- Immerzeel, W. W., and A. F. Lutz (2012), *Regional knowledge sharing on climate change scenario downscaling. FutureWater technical report 116.*, Wageningen, The Netherlands.
- Immerzeel, W. W., P. Droogers, S. M. de Jong, and M. F. P. Bierkens (2009), Large-scale monitoring of snow cover and runoff simulation in Himalayan river basins using remote sensing, *Remote Sens. Environ.*, 113(1), 40–49, doi:10.1016/j.rse.2008.08.010. [online] Available from: <http://linkinghub.elsevier.com/retrieve/pii/S0034425708002575> (Accessed 26 July 2011)
- Immerzeel, W. W., L. P. . Van Beek, and M. F. P. Bierkens (2010a), Climate change will affect the Asian water towers, *Science (80-.)*, 328(5984), 1382–5, doi:10.1126/science.1183188. [online] Available from: <http://www.ncbi.nlm.nih.gov/pubmed/20538947> (Accessed 20 July 2011)
- Immerzeel, W. W., L. P. . Van Beek, and M. F. P. Bierkens (2010b), Climate change will affect the Asian water towers, *Science (80-.)*, 328(5984), 1382–5, doi:10.1126/science.1183188.
- Immerzeel, W. W., F. Pellicciotti, and A. B. Shrestha (2012), Glaciers as a Proxy to Quantify the Spatial Distribution of Precipitation in the Hunza Basin, *Mt. Res. Dev.*, 32(1), 30–38, doi:10.1659/MRD-JOURNAL-D-11-00097.1.
- Immerzeel, W. W., F. Pellicciotti, and M. F. P. Bierkens (2013a), Rising river flows throughout the twenty-first century in two Himalayan glacierized watersheds, *Nat. Geosci.*, 6(8), 1–4, doi:10.1038/ngeo1896. [online] Available from: <http://www.nature.com/doi/10.1038/ngeo1896> (Accessed 5 August 2013)
- Immerzeel, W. W., F. Pellicciotti, and M. F. P. Bierkens (2013b), Rising river flows throughout the twenty-first century in two Himalayan glacierized watersheds, *Nat. Geosci.*, 6(8), 1–4, doi:10.1038/ngeo1896.
- IPCC (2013), *Climate Change 2013: The Physical Science Basis. Contribution of Working Group I to the Fifth Assessment Report of the Intergovernmental Panel on Climate Change*, Cambridge, UK.
- Kääb, A., E. Berthier, C. Nuth, J. Gardelle, and Y. Arnaud (2012a), Contrasting patterns of early twenty-first-century glacier mass change in the Himalayas., *Nature*, 488(7412), 495–8, doi:10.1038/nature11324. [online] Available from: <http://www.ncbi.nlm.nih.gov/pubmed/22914167> (Accessed 29 October 2012)



- Kääb, A., E. Berthier, C. Nuth, J. Gardelle, and Y. Arnaud (2012b), Contrasting patterns of early twenty-first-century glacier mass change in the Himalayas., *Nature*, 488(7412), 495–8, doi:10.1038/nature11324.
- Karssenbergh, D., P. Burrough, R. Sluiter, and K. de Jong (2001), The PCRASTER software and course materials for teaching numerical modelling in the environmental sciences, *Trans. GIS*, 5, 99–110, doi:10.1111/1467-9671.00070. [online] Available from: <http://doi.wiley.com/10.1111/1467-9671.00070>
- Khattak, M. S., M. S. Babel, and M. Sharif (2011a), Hydro-meteorological trends in the upper Indus River basin in Pakistan, *Clim. Res.*, 46(2), 103–119, doi:10.3354/cr00957. [online] Available from: <http://www.int-res.com/abstracts/cr/v46/n2/p103-119/> (Accessed 29 November 2012)
- Khattak, M. S., M. S. Babel, and M. Sharif (2011b), Hydro-meteorological trends in the upper Indus River basin in Pakistan, *Clim. Res.*, 46(2), 103–119, doi:10.3354/cr00957.
- Kraaijenbrink, P. (2013a), *Advanced Delta Change method*, De Bilt, The Netherlands.
- Kraaijenbrink, P. (2013b), *Advanced Delta Change method*, De Bilt, The Netherlands.
- Lehner, B. et al. (2011), Global Reservoir and Dam Database, Version 1 (GRanDv1): Reservoirs, Revision 01, [online] Available from: <http://sedac.ciesin.columbia.edu/data/set/grand-v1-reservoirs-rev01>
- Lutz, A. F., and W. W. Immerzeel (2013), *Water Availability Analysis for the Upper Indus, Ganges, Brahmaputra, Salween and Mekong River Basins*, Technical Report 127 FutureWater, Wageningen, The Netherlands.
- Lutz, A. F., W. W. Immerzeel, A. Gobiet, F. Pellicciotti, and M. F. P. Bierkens (2013), Comparison of climate change signals in CMIP3 and CMIP5 multi-model ensembles and implications for Central Asian glaciers, *Hydrol. Earth Syst. Sci.*, 17(9), 3661–3677, doi:10.5194/hess-17-3661-2013. [online] Available from: <http://www.hydrol-earth-syst-sci.net/17/3661/2013/> (Accessed 30 September 2013)
- Lutz, A. F., W. W. Immerzeel, A. B. Shrestha, and M. F. P. Bierkens (2014a), Consistent increase in High Asia's runoff due to increasing glacier melt and precipitation, *Nat. Clim. Chang.*, 4, 587–592, doi:10.1038/NCLIMATE2237.
- Lutz, A. F., W. W. Immerzeel, A. B. Shrestha, and M. F. P. Bierkens (2014b), Consistent increase in High Asia's runoff due to increasing glacier melt and precipitation, *Nat. Clim. Chang.*, 4, 587–592, doi:10.1038/NCLIMATE2237.
- Macdonald, M. K., J. W. Pomeroy, and A. Pietroniro (2009), Parameterizing redistribution and sublimation of blowing snow for hydrological models : tests in a mountainous subarctic catchment, *Hydrol. Process.*, 2583(July), 2570–2583, doi:10.1002/hyp.
- Mukhopadhyay, B., and A. Khan (2014), A quantitative assessment of the genetic sources of the hydrologic flow regimes in Upper Indus Basin and its significance in a changing climate, *J. Hydrol.*, 509, 549–572, doi:10.1016/j.jhydrol.2013.11.059. [online] Available from: <http://linkinghub.elsevier.com/retrieve/pii/S0022169413008834> (Accessed 6 February 2014)
- Palazzi, E., J. Von Hardenberg, and A. Provenzale (2013a), Precipitation in the Hindu-Kush Karakoram Himalaya : Observations and future scenarios, *J. Geophys. Res. Atmos.*, 118, 85–100, doi:10.1029/2012JD018697.



- Palazzi, E., J. Von Hardenberg, and A. Provenzale (2013b), Precipitation in the Hindu-Kush Karakoram Himalaya : Observations and future scenarios, *J. Geophys. Res. Atmos.*, 118, 85–100, doi:10.1029/2012JD018697.
- Pellicciotti, F., C. Buergi, W. W. Immerzeel, M. Konz, and A. B. Shrestha (2012), Challenges and Uncertainties in Hydrological Modeling of Remote Hindu Kush–Karakoram–Himalayan (HKH) Basins: Suggestions for Calibration Strategies, *Mt. Res. Dev.*, 32(1), 39–50, doi:10.1659/MRD-JOURNAL-D-11-00092.1. [online] Available from: <http://www.bioone.org/doi/abs/10.1659/MRD-JOURNAL-D-11-00092.1>
- Van Pelt, S. C., J. J. Beersma, T. a. Buishand, B. J. J. M. van den Hurk, and P. Kabat (2012a), Future changes in extreme precipitation in the Rhine basin based on global and regional climate model simulations, *Hydrol. Earth Syst. Sci.*, 16(12), 4517–4530, doi:10.5194/hess-16-4517-2012.
- Van Pelt, S. C., J. J. Beersma, T. a. Buishand, B. J. J. M. van den Hurk, and P. Kabat (2012b), Future changes in extreme precipitation in the Rhine basin based on global and regional climate model simulations, *Hydrol. Earth Syst. Sci.*, 16(12), 4517–4530, doi:10.5194/hess-16-4517-2012.
- Schaefli, B., B. Hingray, M. Niggli, and A. Musy (2005), A conceptual glacio-hydrological model for high mountainous catchments, *Hydrol. Earth Syst. Sci.*, 2(1), 73–117, doi:10.5194/hessd-2-73-2005. [online] Available from: <http://www.hydrol-earth-syst-sci-discuss.net/2/73/2005/>
- Sharif, M., D. R. Archer, H. J. Fowler, and N. Forsythe (2013a), Trends in timing and magnitude of flow in the Upper Indus Basin, *Hydrol. Earth Syst. Sci.*, 17(4), 1503–1516, doi:10.5194/hess-17-1503-2013. [online] Available from: <http://www.hydrol-earth-syst-sci.net/17/1503/2013/> (Accessed 22 January 2014)
- Sharif, M., D. R. Archer, H. J. Fowler, and N. Forsythe (2013b), Trends in timing and magnitude of flow in the Upper Indus Basin, *Hydrol. Earth Syst. Sci.*, 17(4), 1503–1516, doi:10.5194/hess-17-1503-2013.
- Shrestha, A. B., and R. Aryal (2010), Climate change in Nepal and its impact on Himalayan glaciers, *Reg. Environ. Chang.*, 11(S1), 65–77, doi:10.1007/s10113-010-0174-9. [online] Available from: <http://link.springer.com/10.1007/s10113-010-0174-9> (Accessed 5 February 2014)
- Tahir, A. A., P. Chevallier, Y. Arnaud, L. Neppel, and B. Ahmad (2011a), Modeling snowmelt-runoff under climate scenarios in the Hunza River basin, Karakoram Range, Northern Pakistan, *J. Hydrol.*, 409(1-2), 104–117, doi:10.1016/j.jhydrol.2011.08.035. [online] Available from: <http://linkinghub.elsevier.com/retrieve/pii/S0022169411005816> (Accessed 30 September 2013)
- Tahir, A. A., P. Chevallier, Y. Arnaud, L. Neppel, and B. Ahmad (2011b), Modeling snowmelt-runoff under climate scenarios in the Hunza River basin, Karakoram Range, Northern Pakistan, *J. Hydrol.*, 409(1-2), 104–117, doi:10.1016/j.jhydrol.2011.08.035.
- Taylor, K. E., R. J. Stouffer, and G. A. Meehl (2012), An Overview of CMIP5 and the Experiment Design, *Bull. Am. Meteorol. Soc.*, 93(4), 485–498, doi:10.1175/BAMS-D-11-00094.1.
- Wagnon, P. et al. (2013), Seasonal and annual mass balances of Mera and Pokalde glaciers (Nepal Himalaya) since 2007, *Cryosph.*, 7(6), 1769–1786, doi:10.5194/tc-7-1769-2013.
- Winiger, M., M. Gumpert, and H. Yamout (2005a), Karakorum-Hindukush-western Himalaya: assessing high-altitude water resources, *Hydrol. Process.*, 19(12), 2329–2338, doi:10.1002/hyp.5887.



Winiger, M., M. Gumpert, and H. Yamout (2005b), Karakorum-Hindukush-western Himalaya: assessing high-altitude water resources, *Hydrol. Process.*, 19(12), 2329–2338, doi:10.1002/hyp.5887.

Yatagai, A., K. Kamiguchi, O. Arakawa, A. Hamada, N. Yasutomi, and A. Kitoh (2012a), APHRODITE: Constructing a Long-Term Daily Gridded Precipitation Dataset for Asia Based on a Dense Network of Rain Gauges, *Bull. Am. Meteorol. Soc.*, 93(9), 1401–1415, doi:10.1175/BAMS-D-11-00122.1. [online] Available from: <http://journals.ametsoc.org/doi/abs/10.1175/BAMS-D-11-00122.1> (Accessed 1 March 2013)

Yatagai, A., K. Kamiguchi, O. Arakawa, A. Hamada, N. Yasutomi, and A. Kitoh (2012b), APHRODITE: Constructing a Long-Term Daily Gridded Precipitation Dataset for Asia Based on a Dense Network of Rain Gauges, *Bull. Am. Meteorol. Soc.*, 93(9), 1401–1415, doi:10.1175/BAMS-D-11-00122.1.

